

Numerical studies on the matrix model and
the expanding universe

Yuta Ito

Doctor of Philosophy

Department of Particle and Nuclear Physics
School of High Energy Accelerator Science
SOKENDAI (The Graduate University for
Advanced Studies)

Numerical studies on the matrix model and the expanding universe

Yuta Ito

*Department of Particle and Nuclear Physics,
Graduate University for the Advanced Studies (SOKENDAI),
Tsukuba, Ibaraki, 305-0821, Japan*

yito@post.kek.jp

Abstract

In this thesis I study the dynamics of the space-time in the matrix models using numerical simulations. Recent studies on the Lorentzian type IIB matrix model show that (3+1)d space-time emerges dynamically from (9+1)d space-time predicted by superstring theory, which indicates the birth of the (3+1)d universe in the string theory. In order to investigate what happens at late times, I study the two simplified Lorentzian type IIB matrix models. We find that the emergent space expands exponentially at early times, which changes into a power-law behavior $t^{1/2}$ with respect to time t at late times. This is reminiscent of the expanding behavior in the inflation and the Friedmann-Robertson-Walker universe in the radiation dominated era, respectively. Moreover, I investigate the infrared cutoff dependence of the expanding behavior in these models. For the simplified model, it turns out that the infrared cutoff effects disappear for a certain region of the cutoff parameter in the infinite volume limit.

On the other hand, I investigate the dimensionality of emergent space by the toy model of the Euclidean type IIB matrix model which has a spontaneous breaking of rotational SO(4) symmetry. From the complex Langevin approach, I show that introducing extra mass parameters in the Dirac operator extends the range of applicability of the method, which enable us to observe the spontaneous breaking of SO(4) symmetry. Moreover, I show that the result obtained by extrapolating the parameters to zero is consistent with the one obtained by another method.

Contents

1	Introduction	3
2	Review of the type IIB matrix model	6
3	Lorentzian version of the type IIB matrix model	12
3.1	Brief review of the Lorentzian type IIB matrix model	13
4	Expanding behavior of the Universe	18
4.1	The simplified model for early times	19
4.2	The simplified model for late times	21
4.2.1	Properties of the bosonic model for $N < N_c$	22
4.2.2	Properties of the bosonic model for $N \geq N_c$	23
5	The IR cutoff dependence of the expanding behavior	28
5.1	Generalization of the form of the IR cutoffs	29
5.2	The p dependence of $R(t)$	30
5.3	The Schwinger-Dyson equations in the simplified model	31
6	The matrix model with $SO(4)$ rotational symmetry	43
6.1	The definition of the toy model of the Euclidean type IIB matrix model	44
6.2	Brief review of the complex Langevin approach	48
6.3	The application to the complex action case	49
6.4	Application of the complex Langevin method to the matrix model	53
7	Summary and discussion	62
A	Details of Monte Carlo simulation	65
B	Results for the (5+1)D version of the bosonic model	67
C	The differences between two simplified models	70
D	Review of stochastic quantization and the Langevin equation	72
E	The result for the another fermion mass term	78

1 Introduction

The Standard Model is extremely successful in understanding quantum field theory of fundamental interactions and it can explain the experimental observations except for a few important remaining problems. In particular, lattice gauge theory has been established as the non-perturbative approach for studying physics of the strong interaction. The numerical study by the lattice gauge theory is actually the powerful approach to understanding the physics in the strong coupling region where perturbative approach is not applicable. On the other hand, describing the quantum gravity has not been achieved yet. However, the description of quantum gravity is necessary to understanding dynamics of the early universe in which macroscopic description of gravity as general relativity breaks down due to the cosmic singularity. As a most promising candidate of quantum gravity theory, the string theory has been studied for a long time. However, superstring theory requires the space-time to be ten dimensional whereas our universe is four dimensional.

In fact, one can obtain four-dimensional space-time by compactifying the extra dimensions with various ways, which allows too many vacua giving four-dimensional low energy effective field theories with various gauge symmetries. Nevertheless, there is no guiding principle to pick up one vacuum from those vacua as far as one deals with superstring theory perturbatively. It is therefore necessary to consider superstring theory non-perturbatively.

As a non-perturbative formulation of superstring/M theory, matrix models were proposed. They can be obtained by dimensionally reducing the ten-dimensional $\mathcal{N} = 1$ super Yang-Mills theory to $d = 0$ [1], $d = 1$ [2] and $d = 2$ [3]. The matrix models can naturally describe the many-body system of strings.

The type IIB matrix model [1] is one of these proposals corresponding to the $d = 0$ case mentioned above, whose action can be derived from the Schild type world-sheet action of type IIB superstring by the matrix regularization. The important feature of this model is that the space-time does not exist a priori and is described dynamically as the eigenvalue distribution of the ten bosonic matrices. In this context, the idea of emergent gravity has been pursued [4–11] in the gauge theories on the non-commutative space which appear from the type IIB matrix model for a particular class of backgrounds [12–15]. Until recently, this model was studied after making a Wick rotation [16–29] because the partition function of the Euclidean model obtained in this way was shown to be finite [30,31]. However, the Euclidean model is not suitable for studying the real time dynamics because the time coordinate is treated as purely imaginary. Moreover, it is known that the Wick rotation is more subtle in quantum gravity theory than in quantum field theory at the non-perturbative level [32,33]. Indeed a recent study using the Gaussian expansion method suggests that the emergent space-

time in the Euclidean matrix model does not seem to be four-dimensional space-time [34].

On the other hand, the Lorentzian version of the type IIB matrix model has been studied using Monte Carlo simulation for the first time in ref. [35]. Unlike the Euclidean case, one has to introduce the infrared cutoffs in both the temporal and spatial directions in order to make the partition function finite. Although such a subtlety remains (it will be discussed in detail later), the Lorentzian matrix model is suitable for studying real-time dynamics. The eigenvalue distribution of the matrix representing the time coordinate can extend to infinity owing to the existence of supersymmetry, and dominant configurations of spatial matrices obtained by Monte Carlo simulation have a very nontrivial structure. This structure enables us to naturally extract the time evolution from the matrices. It turned out that the large- N scaling behavior is observed, and surprisingly, the $SO(9)$ rotational symmetry of the 9d space is spontaneously broken down to $SO(3)$ at some critical time, after which only three out of nine spatial directions start to expand. This emergence of 3d space indicates the birth of the three-dimensional universe in the string theory. It should be emphasized that the dimensionality of the space-time is determined uniquely by the non-perturbative dynamics of superstring theory in contrast to the perturbative superstring theory in which consistent vacua can have various space-time dimensionality.

As another important property of the Lorentzian IIB matrix model, it is expected that the classical approximation becomes valid at late times since each term in the action becomes large as the expansion of the “universe” proceeds, which enables us to investigate possible behaviors at late times [36–40]. A general prescription to construct solutions to the classical equations of motion was given in ref. [37]. One can actually construct classical solutions corresponding to an expanding (3+1)d universe, which naturally solve the cosmological constant problem [37]. As a closely related progress, it was found that matrix configurations with intersecting fuzzy spheres in the extra dimensions can accommodate the standard model fermions [41–47]. In fact, it is known that the classical equations of motion of the matrix model have infinitely many solutions [37]. Therefore, in order to determine which classical solution is actually realized at late times, we need to study the time-evolution of the “universe” at least for a sufficiently long time by performing Monte Carlo simulation.

One can also study the qualitative behavior of the expanding 3d space in a long time evolution using the simplified models of the Lorentzian type IIB matrix model [48–50]. These models are obtained by using an approximation, which captures important properties of the original model at early times and at late times. This simplification and the usage of a large-scale parallel computer enable us to perform Monte Carlo simulation with much larger matrix size.

The first simplified model describes the early time behaviors of the original model [49].

With the matrix size $N \leq 256$, we observed a clear exponentially expanding behavior, which is reminiscent of the inflation. Monte Carlo studies of the original model with $N = 24$ [48] yielded results consistent with this observation. The second simplified model describes the late time behaviors of the original model, which is merely a bosonic model defined by omitting the fermionic matrices [50]. Unlike in the case of the original model, it turns out that the eigenvalue distribution of the temporal matrix has a finite extent without introducing an IR cutoff in the temporal direction due to the absence of supersymmetry. In spite of this, we find that the properties of the model changes drastically at the critical $N = N_c$, and one can extract the meaningful time-evolution for $N \geq N_c$. Moreover, the model suggests that the exponential expansion terminates at some point in time and changes into the power-law $t^{1/2}$ expansion which is consistent with the expanding behavior for the Friedmann-Robertson-Walker universe in the radiation dominated era. These results indicate that the exponential expansion of the space suggested in the original model actually ends at some point in time and turns into a power law similarly to the bosonic model. This would imply that the number of e-foldings is determined dynamically in the Lorentzian type IIB matrix model.

Let us recall that these interesting observations are obtained from the Lorentzian type IIB matrix model, which is regularized by infrared cutoffs. However, unlike in quantum field theories, it is not obvious that the effects of IR cutoffs disappear in the infinite volume limit because the extent of space-time is given by the dynamics of the model. Therefore we consider the IR cutoffs deformed with a parameter and study how it affects the expanding behavior in the simplified model. We found that the expanding behavior becomes universal for a certain range of the cutoff parameter. This suggests that the IR cutoff effects disappear for such a parameter region. We also found that this suggestion are supported by the analysis using the Schwinger-Dyson equation, in which the terms arising from the IR cutoffs decrease as N is increased for the same range of the cutoff parameter.

In this thesis, we also discuss the Euclidean version of the type IIB matrix model. In the Euclidean model the complex fermion determinant causes the sign problem which makes numerical studies difficult. As we mentioned earlier, there are several proposals to overcome this problem. Especially, the recent studies on the complex Langevin approach [51] and the Lefschetz thimble approach solve the sign problem for several simple cases [53–59]. One of the issues in the complex Langevin method we consider in this thesis is that the condition for which the method works is not understood very well. However, recent studies revealed certain criteria to justify the method, and in order to satisfy the criteria, one can consider an improvement called by the “gauge cooling”. It is known that the complex Langevin method (CLM) in fact becomes successful at some parameter region of QCD at finite density and the related Random Matrix theory.

In this thesis we consider a matrix model which is expected to undergo a spontaneous breaking of the rotational $\text{SO}(4)$ symmetry. This model is considered as a simplified model of the Euclidean type IIB matrix model. In application of the complex Langevin approach to this simplified matrix model, it turned out that the gauge cooling for justifying the method does not work well enough. Therefore, in addition to the gauge cooling, we introduced the mass parameter m_f to the fermion action to improve the method further. After taking the $m_f \rightarrow 0$ limit, we have shown that the $\text{SO}(4)$ symmetry actually breaks spontaneously down to $\text{SO}(2)$.

The rest of this paper is organized as follows. In section 2 we review the definition of the type IIB matrix model. In section 3 we briefly review the definition and some important properties of the Lorentzian type IIB matrix model. In section 4 we define the simplified models, and present results obtained by direct Monte Carlo studies. In section 5 we discuss the dependence of the expanding behavior of space-time on the IR cutoffs in the simplified model. In section 6 we study the Euclidean matrix model, in which we investigate the spontaneous breaking of rotational symmetry in the simplified model using the complex Langevin approach. Section 7 is devoted to a summary and discussions.

2 Review of the type IIB matrix model

I briefly introduce the type IIB matrix model we consider in this paper. The model was proposed as a non-perturbative formulation of superstring theory, which is defined by dimensional reducing the 10d $\mathcal{N} = 1$ SYM theory to zero-dimension. On the other hand, one can show that the model can be derived from the world-sheet action of the type IIB superstring by applying the matrix regularization. Moreover, the model naturally seems to describe the many-body system of strings by embedding them to matrix degrees of freedom. In what follows, I show that the action of the type IIB matrix model can be derived from the Shild type world-sheet action of the type IIB superstring.

The action of the type IIB matrix model is given by

$$S = \frac{1}{g^2} \text{Tr} \left([A_\mu, A_\nu] [A^\mu, A^\nu] + \frac{1}{2} \bar{\Psi} \Gamma^\mu [A_\mu, \Psi] \right), \quad (2.1)$$

where A_μ ($\mu = 0, \dots, 9$) are the $N \times N$ Hermitian matrices. Γ^μ are the 10d gamma matrices and Ψ_α ($\alpha = 1, \dots, 16$) are the 10d Majorana-Weyl spinors which are also $N \times N$ Hermitian matrices. Therefore the action has the $\text{SO}(9,1)$ symmetry.

Then, we show that the action (2.1) can be derived from the Green-Schwartz action for

the type IIB superstring

$$S_{\text{GS}} = -T \int d^2\sigma \left(\sqrt{-\frac{1}{2}\Sigma^2} + i\epsilon^{ab}\partial_a X^\mu (\bar{\theta}^1 \Gamma_\mu \partial_b \theta^1 + \bar{\theta}^2 \Gamma_\mu \partial_b \theta^2) + \epsilon^{ab}\bar{\theta}^1 \Gamma^\mu \partial_a \theta^1 \bar{\theta}^2 \Gamma_\mu \partial_b \theta^2 \right), \quad (2.2)$$

where T is the tension of a string and σ^a ($a = 1, 2$) is the world-sheet coordinate. θ^1 and θ^2 are the 10d Majorana-Weyl spinors which have the same chirality in 10d space-time since we are considering the type IIB superstring. $\Sigma^{\mu\nu}$ is defined by

$$\begin{aligned} \Sigma^{\mu\nu} &= \epsilon^{ab}\Pi_a^\mu \Pi_b^\nu, \\ \Pi_a^\mu &= \partial_a X^\mu - i\bar{\theta}^1 \Gamma^\mu \partial_a \theta^1 + i\bar{\theta}^2 \Gamma^\mu \partial_a \theta^2. \end{aligned} \quad (2.3)$$

Note that the action (2.1) is defined after taking the analytic continuation $\theta^2 \rightarrow i\theta^2$.

One can show that the action (2.1) has the 10 dimensional $\mathcal{N} = 2$ supersymmetry

$$\begin{aligned} \delta_{SUSY}\theta^1 &= \epsilon^1, \\ \delta_{SUSY}\theta^2 &= \epsilon^2, \\ \delta_{SUSY}X^\mu &= i\bar{\epsilon}^1 \Gamma^\mu \theta^1 - i\bar{\epsilon}^2 \Gamma^\mu \theta^2 \end{aligned} \quad (2.4)$$

and the κ -symmetry

$$\begin{aligned} \delta_\kappa \theta^1 &= \alpha^1, \\ \delta_\kappa \theta^2 &= \alpha^2, \\ \delta_\kappa X^\mu &= i\bar{\theta}^1 \Gamma^\mu \alpha^1 - i\bar{\theta}^2 \Gamma^\mu \alpha^2, \end{aligned} \quad (2.5)$$

where α^1 and α^2 are defined by

$$\begin{aligned} \alpha^1 &= (1 + \tilde{\Gamma}) \kappa^1, \\ \alpha^2 &= (1 - \tilde{\Gamma}) \kappa^2, \\ \tilde{\Gamma} &= \frac{1}{2\sqrt{-\frac{1}{2}\Sigma^2}} \Sigma_{\mu\nu} \Gamma^{\mu\nu}. \end{aligned} \quad (2.6)$$

κ^1 and κ^2 are local parameter of the Majorana-Weyl spinors depending on the world-sheet coordinate σ^a . One can show that $\tilde{\Gamma}^2 = 1$, from which it turns out that α^1 and α^2 have only a half degree of freedom of θ^1 and θ^2 . Therefore by fixing the gauge of the κ -symmetry, one can reduce the d. o. f. of θ^1 and θ^2 by half. Since the chirality of θ^1 and θ^2 are same, the

Lorentz symmetry is preserved even after the gauge fixing.

Now, let us choose the gauge of the κ symmetry so that

$$\theta^1 = \theta^2 = \psi . \quad (2.7)$$

Then the action (2.1) becomes

$$\tilde{S}_{\text{GS}} = -T \int d^2\sigma \left(\sqrt{-\frac{1}{2}\sigma^{\mu\nu}\sigma_{\mu\nu}} + 2i\epsilon^{ab}\partial_a X^\mu \bar{\psi} \Gamma_\mu \partial_b \psi \right) , \quad (2.8)$$

where

$$\sigma^{\mu\nu} = \epsilon^{ab}\partial_a X^\mu \partial_b X^\nu . \quad (2.9)$$

One can see that the action (2.8) still has the $\mathcal{N} = 2$ supersymmetry by defining a new supersymmetric transformation so that the gauge fixing condition (2.7) is preserved as

$$\begin{aligned} \delta\theta^1 &= (\delta_{SUSY} + \delta_\kappa) \theta^1 , \\ \delta\theta^2 &= (\delta_{SUSY} + \delta_\kappa) \theta^2 , \\ \delta X^\mu &= (\delta_{SUSY} + \delta_\kappa) X^\mu , \end{aligned} \quad (2.10)$$

and in order to satisfy $\delta\theta^1 = \delta\theta^2$ we set κ^1 and κ^2 as

$$\begin{aligned} \kappa^1 &= \frac{-\epsilon^1 + \epsilon^2}{2} , \\ \kappa^2 &= \frac{\epsilon^1 - \epsilon^2}{2} . \end{aligned} \quad (2.11)$$

Then, by introducing new parameters ξ and ϵ as

$$\begin{aligned} \xi &= \frac{\epsilon^1 + \epsilon^2}{2} , \\ \epsilon &= \frac{\epsilon^1 - \epsilon^2}{2} , \end{aligned} \quad (2.12)$$

we can rewrite the $\mathcal{N}=2$ supersymmetry using ξ and ϵ as

$$\begin{aligned} \delta^{(1)}\psi &= -\frac{1}{2\sqrt{-\frac{1}{2}\sigma^2}}\sigma_{\mu\nu}\alpha\Gamma^{\mu\nu}\epsilon , \\ \delta^{(1)}X^\mu &= 4i\bar{\epsilon}\Gamma^\mu\psi , \end{aligned} \quad (2.13)$$

and

$$\begin{aligned}\delta^{(2)}\psi &= \xi, \\ \delta^{(2)}X^\mu &= 0.\end{aligned}\tag{2.14}$$

Furthermore, we rewrite the Nambu-Goto type action (2.8) to the Schild type action. In order to do this, we introduce the Poisson bracket

$$\{X, Y\} \equiv \frac{1}{\sqrt{g}}\epsilon^{ab}\partial_a X\partial_b Y,\tag{2.15}$$

where \sqrt{g} is the world-sheet density defined by the metric g_{ab} on the world-sheet. Using the Poisson bracket, the action (2.8) can be written as

$$S_{\text{Schild}} = \int d^2\sigma \left[\sqrt{g}\alpha \left(\frac{1}{4} \{X^\mu, X^\nu\}^2 - \frac{i}{2}\bar{\psi}\Gamma^\mu \{X^\mu, \psi\} \right) + \beta\sqrt{g} \right].\tag{2.16}$$

One can show that the above action is equivalent to the Nambu-Goto type action (2.8). In fact, the equation of motion for \sqrt{g} is given by

$$-\frac{1}{4}\alpha\frac{1}{g}\left(\epsilon^{ab}\partial_a X^\mu\partial_b X^\nu\right)^2 + \beta = 0.\tag{2.17}$$

Then one obtains

$$\sqrt{g} = \frac{1}{2}\sqrt{\frac{\alpha}{\beta}}\sqrt{(\epsilon^{ab}\partial_a X^\mu\partial_b X^\nu)^2}.\tag{2.18}$$

By substituting (2.18) to the Schild type action (2.16), one obtains the action as

$$\int d^2\sigma \left(\sqrt{\alpha\beta}\sqrt{(\epsilon^{ab}\partial_a X^\mu\partial_b X^\nu)^2} - \frac{i}{2}\alpha\epsilon^{ab}\partial_a X^\mu\bar{\psi}\Gamma^\mu\partial_b\psi \right),\tag{2.19}$$

which is equivalent to (2.8) up to the normalization.

Note that the $\mathcal{N} = 2$ supersymmetry is realized for the Schild type action (2.16) as

$$\begin{aligned}\delta^{(1)}\psi &= -\frac{1}{2}\{X_\mu, X_\nu\}\Gamma^{\mu\nu}\epsilon, \\ \delta^{(1)}X^\mu &= i\bar{\epsilon}\Gamma^\mu\psi,\end{aligned}\tag{2.20}$$

and

$$\begin{aligned}\delta^{(2)}\psi &= \xi, \\ \delta^{(2)}X^\mu &= 0.\end{aligned}\tag{2.21}$$

Here, one can formally consider the quantization of the action (2.16) with the path integral formalism as

$$Z = \int \mathcal{D}\sqrt{g} \mathcal{D}X \mathcal{D}\psi e^{S_{\text{Schild}}} . \quad (2.22)$$

In addition to the $\mathcal{N} = 2$ SUSY, the action (2.16) has the diffeomorphism invariance for the world-sheet such as

$$\begin{aligned} \delta_d \psi &= \epsilon^a \partial_a \psi , \\ \delta_d X^\mu &= \epsilon^a \partial_a X^\mu , \\ \delta_d \sqrt{g} &= \epsilon^a \partial_a \sqrt{g} . \end{aligned} \quad (2.23)$$

Note that we assume here that the measure of the path integral (2.22) is invariant under the transformation (2.23). For instance, one considers to fix the gauge for which \sqrt{g} is constant all over the world-sheet. Therefore the infinitesimal transformation of \sqrt{g} in (2.23) becomes

$$\delta_d \sqrt{g} = \epsilon^a \partial_a \sqrt{g} = 0 . \quad (2.24)$$

The solution of the above differential equation is given by

$$\epsilon^a = \frac{1}{\sqrt{g}} \epsilon^{ab} \partial_b \rho \quad (2.25)$$

using the arbitrary function $\rho(\sigma^a)$. Then substituting (2.25) to (2.23) gives the ‘‘area preserving diffeomorphism’’ as

$$\begin{aligned} \delta_d \psi &= \{ \psi, \rho \} , \\ \delta_d X^\mu &= \{ \psi, X^\mu \} , \\ \delta_d \sqrt{g} &= 0 . \end{aligned} \quad (2.26)$$

In particular, it satisfies the w_∞ -algebra which is described by the Poisson bracket. One considers to regularize the path integral (2.22), in which one regularizes the w_∞ -algebra with the $SU(n)$ algebra. When n is sufficiently large, one can approximate the Poisson bracket and the integral with respect to the world-sheet coordinate by the commutator and the trace of matrices

$$\begin{aligned} \{ , \} &\rightarrow -i [,] , \\ \frac{1}{2\pi} \int d^2\sigma &\rightarrow \text{Tr} . \end{aligned} \quad (2.27)$$

In this context, the bosonic fields X_μ and fermionic fields ψ become $n \times n$ Hermitian matrices and the properties for the Poisson bracket

$$\begin{aligned} \int d^2\sigma \sqrt{g} \{X, Y\} &= \int d^2\sigma \partial_a (\epsilon^{ab} X \partial_b Y) = 0, \\ \int d^2\sigma \sqrt{g} X \{Y, Z\} &= \int d^2\sigma \sqrt{g} Z \{X, Y\} \end{aligned} \quad (2.28)$$

are replaced by the relations

$$\begin{aligned} \text{Tr}([X, Y]) &= 0, \\ \text{Tr}(X [Y, Z]) &= \text{Tr}(Z [X, Y]). \end{aligned} \quad (2.29)$$

Therefore, by replacing the Poisson bracket and the integral in (2.16) and (2.22) by the commutator and the trace, one obtains the action and partition function of the type IIB matrix model as

$$S_{\text{IKKT}} = \alpha \left(-\frac{1}{4} \text{Tr} [A_\mu A_\nu]^2 - \frac{1}{2} \text{Tr} (\bar{\psi} \Gamma^\mu [A_\mu, \psi]) \right) + 2\pi\beta \text{Tr} 1, \quad (2.30)$$

$$Z = \sum_{n=0}^{\infty} \int dA d\psi e^{-S_{\text{IKKT}}}, \quad (2.31)$$

where we denote the $n \times n$ Hermitian matrices by A_μ . The integral with respect to \sqrt{g} is replaced by the summation over n which represents the area of the world-sheet. The measure in the path integral (2.31) is the Haar measure which is defined as

$$\begin{aligned} dA &= \prod_{\mu} \left(\prod_i d(A_\mu)_{ii} \right) \left(\prod_{i>j} d\text{Re}(A_\mu)_{ij} d\text{Im}(A_\mu)_{ij} \right), \\ d\psi &= \prod_{\alpha} \left(\prod_i d(\psi_\alpha)_{ii} \right) \left(\prod_{i>j} d\text{Re}(\psi_\alpha)_{ij} d\text{Im}(\psi_\alpha)_{ij} \right). \end{aligned} \quad (2.32)$$

One can easily see that the action (2.30) also has the $\mathcal{N} = 2$ supersymmetry. According to the rule (2.27), the supersymmetry transformation for the type IIB matrix model is given as

$$\begin{aligned} \delta^{(1)}\psi &= \frac{i}{2} [A_\mu, A_\nu] \Gamma^{\mu\nu} \epsilon, \\ \delta^{(1)}A_\mu &= i\bar{\epsilon} \Gamma_\mu \psi, \end{aligned} \quad (2.33)$$

and

$$\begin{aligned}\delta^{(2)}\psi &= \xi, \\ \delta^{(2)}A_\mu &= 0.\end{aligned}\tag{2.34}$$

The type IIB matrix model can describe states including more than one string while the Schild action represents the action for one string. In fact, by considering block diagonal configurations, the action (2.30) can be decomposed with the direct sum of block matrices, in which each block represents one string state described by the Schild type action. In that case, off-diagonal blocks can be interpreted to represent interactions between corresponding two strings. Thus, the matrix model is expected to describe the second quantization of string theory.

Note that the term proportional to $\text{Tr}1$ in (2.30) and the summation over n in the path integral (2.31) do not exist in the original action of the type IIB matrix model. This can be interpreted that (2.30) is the effective action obtained by integrating out some sub-matrices. Therefore when one regards $\beta\text{Tr}1$ as a chemical potential for matrix size n , one can interpret the partition function (2.31) as the micro canonical ensemble version of the type IIB matrix model.

3 Lorentzian version of the type IIB matrix model

As was explained in section 2, the type IIB matrix model describes states of more than one string or D-brane as the d.o.f. of matrices. The eigenvalues of matrices describe the positions of D-branes and their distribution can be regarded as the extent of emergent space-time from 10d space-time. Thus, the type IIB matrix model would explain how 4d space-time emerges from the 10d space-time required by superstring theory.

There are many studies on the type IIB matrix model, in which the model have been studied after making the Wick rotation. In the Euclidean model, the partition function turns out to be well-defined and one can deal with it numerically. In that case, the model has $\text{SO}(10)$ symmetry. However, it has not been shown how the dimensionality is chosen. In particular, the study using the Gaussian expansion method suggests that the emergent space is three-dimensional rather than four-dimensional.

On the other hand, the Lorentzian version of the type IIB matrix model has been studied in ref. [35]. In the Lorentzian case, the time coordinate is treated as real and the model is suitable for investigating real time dynamics. Although the action becomes imaginary, it turned out that the imaginary action can be approximated by a delta function, which enables

us to deal with the Lorentzian model numerically. One has to introduce IR cutoffs in practice since the action is unbounded. As a result of numerical analysis, it turned out that the only three out of nine spatial directions start to expand at some point in time-evolution. In what follows, I will briefly review the definition of the Lorentzian type IIB matrix model and the result mentioned above.

3.1 Brief review of the Lorentzian type IIB matrix model

The action of the Lorentzian type IIB matrix model is given by [1]

$$S = S_b + S_f , \quad (3.1)$$

$$S_b = \frac{1}{4g^2} \text{Tr} ([A_\mu, A_\nu] [A^\mu, A^\nu]) , \quad (3.2)$$

$$S_f = -\frac{1}{2g^2} \text{Tr} \left(\Psi_\alpha (\mathcal{C}\Gamma^\mu)_{\alpha\beta} [A_\mu, \Psi_\beta] \right) , \quad (3.3)$$

where the bosonic $N \times N$ matrices A_μ ($\mu = 0, \dots, 9$) and the fermionic matrices Ψ_α ($\alpha = 1, \dots, 16$) are both traceless and Hermitian. Γ^μ are 10D gamma-matrices after the Weyl projection and \mathcal{C} is the charge conjugation matrix. The ‘‘coupling constant’’ g is merely a scale parameter in this model since it can be absorbed by rescaling A_μ and Ψ appropriately. The indices μ and ν are contracted using the Lorentzian metric $\eta_{\mu\nu} = \text{diag}(-1, 1, \dots, 1)$. The Euclidean version can be obtained by making the ‘‘Wick rotation’’ $A_0 = iA_{10}$, where A_{10} is supposed to be Hermitian.

The partition function for the Lorentzian version is proposed in ref. [35] as

$$Z = \int dA d\Psi e^{iS} \quad (3.4)$$

with the action (3.1). The ‘‘ i ’’ in front of the action is motivated from the fact that the string world-sheet metric should also have a Lorentzian signature. By integrating out the fermionic matrices, we obtain the Pfaffian

$$\int d\Psi e^{iS_f} = \text{Pf} \mathcal{M}(A) , \quad (3.5)$$

which is real unlike in the Euclidean case [29]. Note also that the bosonic action (3.2) can be written as

$$S_b = \frac{1}{4g^2} \text{Tr} (F_{\mu\nu} F^{\mu\nu}) = \frac{1}{4g^2} \left\{ -2\text{Tr} (F_{0i})^2 + \text{Tr} (F_{ij})^2 \right\} , \quad (3.6)$$

where we have introduced the Hermitian matrices $F_{\mu\nu} = i[A_\mu, A_\nu]$. Since the two terms in the last expression of eq. (3.6) are non-positive definite and have opposite signs, S_b is not

positive semi-definite. Therefore it is not bounded from below.

In order to make the partition function (3.4) finite, one needs to introduce infrared cutoffs in both the temporal and spatial directions, for instance, as

$$\frac{1}{N} \text{Tr} (A_0)^2 \leq \kappa \frac{1}{N} \text{Tr} (A_i)^2 , \quad (3.7)$$

$$\frac{1}{N} \text{Tr} (A_i)^2 \leq \Lambda^2 . \quad (3.8)$$

It is important to confirm that the IR cutoffs can be removed in the infinite volume limit, which is discussed in Section (5).

In the present work, it is important to understand the reason why we need to introduce the cutoff (3.7) in the temporal direction. Note first that one can use the $SU(N)$ symmetry of the model to bring the temporal matrix A_0 into the diagonal form

$$A_0 = \text{diag} (\alpha_1, \dots, \alpha_N) , \quad \text{where } \alpha_1 < \dots < \alpha_N . \quad (3.9)$$

By ‘‘fixing the gauge’’ in this way, we can rewrite the partition function (3.4) as

$$Z = \int \prod_{i=1}^9 dA_i \prod_{k=1}^N d\alpha_k \Delta(\alpha)^2 \text{Pf} \mathcal{M} (A) e^{iS_b} , \Delta(\alpha) \equiv \prod_{a>b}^N (\alpha_a - \alpha_b) , \quad (3.10)$$

where $\Delta(\alpha)$ is the van der Monde determinant. The factor $\Delta(\alpha)^2$ in (3.10) appears from the Fadeev-Popov procedure for the gauge fixing, and it acts as a repulsive potential between the eigenvalues α_k of A_0 . Here we consider a situation in which the eigenvalues of A_0 are well separated from each other. Then the action $S = S_b + S_f$ can be expanded as

$$S_b = -\frac{1}{2g^2} (\alpha_a - \alpha_b)^2 |(A_i)_{ab}|^2 + \dots , \quad (3.11)$$

$$S_f = -\frac{1}{2g^2} (\Psi_\alpha)_{ba} (\alpha_a - \alpha_b) (\mathcal{C}\Gamma^\mu)_{\alpha\beta} (\Psi_\beta)_{ab} + \dots , \quad (3.12)$$

omitting the sub-leading terms for large $|\alpha_a - \alpha_b|$. Integrating out A_i at one loop neglecting the zero modes corresponding to diagonal elements, we obtain $\Delta(\alpha)^{-18}$ for the one-loop potential of α_k which acts as a attractive force between α_k . On the other hand, integrating out Ψ_α at one loop similarly, we obtain $\Delta(\alpha)^{16}$. Thus we find that the potential between α_i is canceled exactly at the one-loop level. This is actually a consequence of supersymmetry [1] of the model (3.4). Owing to this property, the eigenvalue distribution of A_0 extends to infinity even for finite N if the cutoff (3.7) were absent.

In fact, after some manipulation and rescaling of A_μ , we can rewrite the partition function

(3.4) as

$$\begin{aligned}
Z &= \int dA \text{Pf}\mathcal{M}(A) \delta\left(\frac{1}{N}\text{Tr}(F_{\mu\nu}F^{\mu\nu})\right) \delta\left(\frac{1}{N}\text{Tr}(A_i)^2 - 1\right) \theta\left(\kappa - \frac{1}{N}\text{Tr}(A_0)^2\right) \\
&= \int \prod_{a=1}^N d\alpha_a \prod_{i=1}^d dA_i \Delta^2(\alpha) \text{Pf}\mathcal{M}(A) \delta\left(\frac{1}{N}\text{Tr}(F_{\mu\nu}F^{\mu\nu})\right) \\
&\quad \times \delta\left(\frac{1}{N}\text{Tr}(A_i)^2 - 1\right) \theta\left(\kappa - \frac{1}{N}\text{Tr}(A_0)^2\right), \tag{3.13}
\end{aligned}$$

where $\theta(x)$ is the Heaviside step function. This form allows us to performing Monte Carlo simulation of the Lorentzian model without the sign problem unlike the Euclidean model.¹

Let us note first that the integrand of the partition function (3.4) involves a phase factor e^{iS_b} . As is commonly done in integrating oscillating functions, we introduce a convergence factor $e^{-\epsilon|S_b|}$ and take the $\epsilon \rightarrow 0$ limit after the integration.

Then the partition function can be rewritten as

$$Z = \int dA \int_0^{\Lambda^2} dr \delta\left(\frac{1}{N}\text{Tr}(A_i)^2 - r\right) \theta\left(\kappa r - \frac{1}{N}\text{Tr}(A_0)^2\right) e^{iS_b - \epsilon|S_b|} \text{Pf}\mathcal{M}, \tag{3.14}$$

where κ and Λ are the cutoff parameters introduced in (3.7) and (3.8), respectively. Rescaling the variables $A_\mu \rightarrow r^{1/2}A_\mu$ in the integrand, we get

$$Z = \int dA \text{Pf}\mathcal{M}(A) f(S_b) \delta\left(\frac{1}{N}\text{Tr}(A_i)^2 - 1\right) \theta\left(\kappa - \frac{1}{N}\text{Tr}(A_0)^2\right), \tag{3.15}$$

where the function $f(S_b)$ is defined by

$$f(S_b) \equiv \int_0^{\Lambda^2} dr r^{9(N^2-1)-1} e^{r^2(iS_b - \epsilon|S_b|)}. \tag{3.16}$$

Note that $f(S_b)$ is a complex-valued function with the property $f(-S_b) = f(S_b)^*$. For $|S_b| \ll \frac{1}{\Lambda^4}$, the function can be well approximated by

$$\begin{aligned}
f(S_b) &\approx \int_0^{\Lambda^2} dr r^{9(N^2-1)-1} \\
&= \frac{1}{9(N^2-1)} (\Lambda^2)^{9(N^2-1)}. \tag{3.17}
\end{aligned}$$

For $|S_b| \gtrsim \frac{1}{\Lambda^4}$, the phase of the integrand in (3.16) starts to oscillate violently in the region

¹Strictly speaking, the Pfaffian $\text{Pf}\mathcal{M}$ in (3.13) can change its sign, but it turned out that configurations with positive Pfaffian dominate at large N .

$r \gtrsim 1/\sqrt{|S_b|}$, and hence the integral decreases rapidly in magnitude for increasing $|S_b|$. In particular, the asymptotic behavior of $f(S_b)$ for $|S_b| \gg \frac{1}{\Lambda^4}$ can be estimated as

$$\begin{aligned} \frac{f(S_b)}{f(0)} &\sim \frac{1}{2} \Gamma\left(\frac{9}{2}(N^2 - 1)\right) |S_b|^{-\frac{9}{2}(N^2 - 1)} \cdot 9(N^2 - 1)(\Lambda^2)^{-9(N^2 - 1)} \\ &= \Gamma\left(\frac{9}{2}(N^2 - 1) + 1\right) \left(\frac{1}{\Lambda^4 |S_b|}\right)^{\frac{9}{2}(N^2 - 1)} \end{aligned} \quad (3.18)$$

by deforming the integration contour in (3.16). Recalling eq. (3.2), the condition $|S_b| \ll \frac{1}{\Lambda^4}$ for (3.17) can be rewritten as

$$\left| \frac{1}{N} \text{Tr}(F_{\mu\nu} F^{\mu\nu}) \right| \ll \frac{4g^2}{N\Lambda^4}. \quad (3.19)$$

Therefore, assuming that the right-hand side $\frac{4g^2}{N\Lambda^4}$ of (3.19) becomes small at large N , we may make a replacement

$$f(S_b) \implies \delta\left(\frac{1}{N} \text{Tr}(F_{\mu\nu} F^{\mu\nu})\right) \quad (3.20)$$

up to a normalization constant. Rescaling the variables $A_\mu \rightarrow A_\mu/L$, we arrive at eq. (3.13). Within the above approximation, the parameter L simply sets the scale of the model, and we may use $L = 1$ without loss of generality.

It turns out that one can extract a time-evolution from configurations generated by simulating (3.13). A crucial observation is that the spatial matrices A_i have a band-diagonal structure in the $SU(N)$ basis in which A_0 has the diagonal form (3.9). More precisely, there exists some integer n such that the elements of spatial matrices $(A_i)_{ab}$ for $|a - b| > n$ are much smaller than those for $|a - b| \leq n$. Based on this observation, we may naturally consider $n \times n$ matrices

$$(\bar{A}_i)_{IJ}(t) \equiv (A_i)_{\nu+I, \nu+J}, \quad (3.21)$$

as representing the state of the universe at time t , where $I, J = 1, \dots, n$ and $\nu = 0, 1, \dots, N - n$. The time t in (3.21) is defined by

$$t = \frac{1}{n} \sum_{I=1}^n \alpha_{\nu+I} \quad (3.22)$$

corresponding to the $n \times n$ matrices \bar{A}_i . For example, we can define the extent of space at time t as

$$R^2(t) = \left\langle \frac{1}{n} \text{tr} \sum_i (\bar{A}_i(t))^2 \right\rangle, \quad (3.23)$$

where the symbol tr represents a trace over the $n \times n$ block. We also define the ‘‘moment of inertia tensor’’

$$T_{ij}(t) = \frac{1}{n} \text{tr} (\bar{A}_i(t) \bar{A}_j(t)) , \quad (3.24)$$

which is a 9×9 real symmetric matrix. The eigenvalues of $T_{ij}(t)$, which we denote by $\lambda_i(t)$ with the order

$$\lambda_1(t) > \lambda_2(t) > \dots > \lambda_9(t) , \quad (3.25)$$

represent the spatial extent in each of the nine directions at time t . Note first that the appearance of the gap between $\langle \lambda_3(t) \rangle$ and $\langle \lambda_4(t) \rangle$ signals the spontaneous symmetry breaking of $\text{SO}(9)$ to $\text{SO}(3)$. Let us therefore define the separations $d_j(t) = \langle \lambda_j(t) \rangle - \langle \lambda_{j+1}(t) \rangle$. Then we find that the symmetric phase can be characterized by $d_1(t) > d_2(t) > \dots > d_8(t)$, while in the broken phase we find $d_2(t) < d_3(t)$. Therefore we may define the critical time t_c by the largest value of t' such that $d_1(t) > d_2(t) > \dots > d_8(t)$ holds for $t \leq t'$. Therefore the expectation values $\langle \lambda_i(t) \rangle$ tend to be equal in the large- N limit if the $\text{SO}(9)$ symmetry is not spontaneously broken. This is the case at early times of the time-evolution. After a critical time t_c , however, we find that three largest eigenvalues $\langle \lambda_i(t) \rangle$ ($i = 1, 2, 3$) become significantly larger than the others, which implies that the $\text{SO}(9)$ symmetry is spontaneously broken down to $\text{SO}(3)$.

It would be interesting to study a long time-evolution of the model and see how the expansion of space proceeds. This requires very large matrices, which makes the simulation unfeasible. In the previous work [49], we studied a simplified model, in which the Pfaffian is replaced by the one-loop contribution $\Delta(\alpha)^{16}$ mentioned above. This replacement is expected to be valid at early times, where the expansion of space has not proceeded much and the leading term in (3.12) is indeed dominant. According to the argument below (3.12), the potential between the eigenvalues of A_0 is canceled at one loop and hence the cutoff (3.7) in the temporal direction is needed in this simplified model as well as in the original model. On the other hand, this simplified model can be simulated with much less effort than the original model.² In ref. [49] the (5+1)d version of the simplified model was studied with the matrix size $N \leq 64$, and the $\text{SO}(5)$ symmetry was found to be broken spontaneously down to $\text{SO}(3)$ at some point in time similarly to the original model. Moreover, the expanding behavior of the 3D space turned out to be exponential,³ and no tendencies of slowing down were observed within the scaling region.

²In order to make one trajectory in the Hybrid Monte Carlo algorithm, the original model requires $\mathcal{O}(N^5)$ arithmetic operations, whereas the simplified model requires only $\mathcal{O}(N^3)$ arithmetic operations. The reason for this is that the number of iterations required for the convergence of the conjugate gradient method used to implement the effects of fermions grows as $\mathcal{O}(N^2)$.

³This behavior is also confirmed with smaller matrix size $N \leq 32$ with the aid of a renormalization group method developed in the same paper [49].

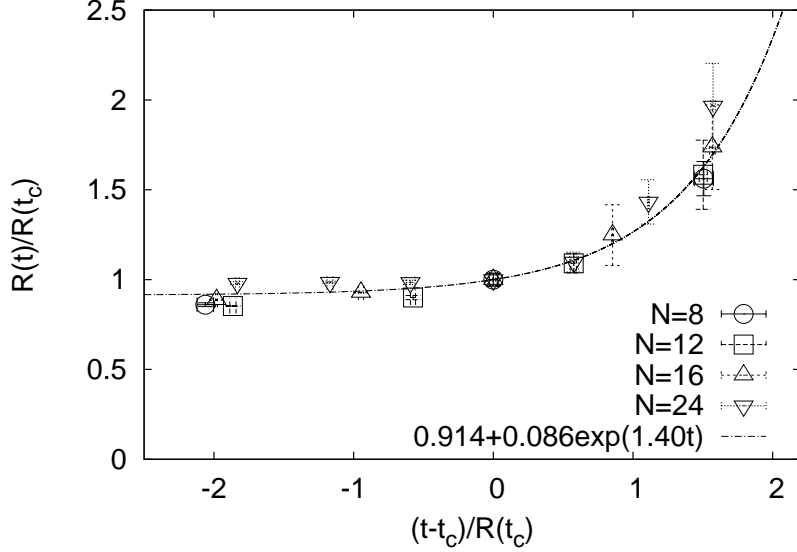


Figure 4.1: The extent of 9d space $R(t)$ normalized by $R(t_c)$ is plotted against time $(t - t_c)/R(t_c)$. The broken line is a fit to $R(t)/R(t_c) = a + (1 - a)\exp(bx)$ with $x = (t - t_c)/R(t_c)$.

As I will show in the next section, analogous behaviors are also confirmed for the (9+1)d version of the simplified model. In the original model, on the other hand, the sub-leading term in the fermionic action (3.12) becomes important at late times as the expansion proceeds, and hence it can affect the expanding behavior.

4 Expanding behavior of the Universe

As I have explained in the previous section, the Lorentzian type IIB matrix model has the interesting property such that the spontaneous symmetry breaking from $SO(9)$ to $SO(3)$. Moreover, as shown in Fig. 4.1, it turned out that the emergent 3d space seems to expand exponentially. However, that expanding behavior is unclear since the time-evolution we have observed is too short to identify it while it is interesting to discuss relations to the inflation if the exponential expansion can be confirmed. Therefore, we consider simplified models of the original Lorentzian model in order to see qualitative expanding behavior in further time-evolution. In this section, we define two simplified models which are expected to describe the expanding behavior at early times and late times, and we discuss how the behaviors depend on such the region in the time-evolution.

4.1 The simplified model for early times

In the Lorentzian case, we have investigated the original type IIB matrix model only for $N \leq 24$ since it takes enormous time to evaluate the Pfaffian.

As an approach to enlarge the matrix size, we consider to deal with the simplified model. We first consider a simplified model obtained by approximating the original model at early period in the time evolution as I will explain below [49]. We focus on approximating the fermion action to simplify the calculation of the Pfaffian. The fermion action (3.3) can be decomposed into two terms as

$$S_f \propto \text{Tr} \left(\bar{\Psi}_\alpha (\Gamma^0)_{\alpha\beta} [A_0, \Psi_\beta] \right) + \text{Tr} \left(\bar{\Psi}_\alpha (\Gamma^i)_{\alpha\beta} [A_i, \Psi_\beta] \right). \quad (4.1)$$

Since the emergent space is not so large at early times, it is expected that the components of A_0 are much larger than that of A_i . In such a situation, the contribution from the first term in (4.1) becomes dominant compared to one from the second term. Then we may merely omit the second term to obtain the simplified model for early times. After that, we can perform explicitly the integration with respect to the fermion matrices, which gives the Pfaffian as

$$\text{Pf} \mathcal{M}(A) \simeq \Delta^{16}(\alpha), \quad (4.2)$$

where $\Delta(\alpha) \equiv \prod_{i>j} (\alpha_i - \alpha_j)$ is the van der Monde determinant. Thus the partition function of the simplified model for early times is given from (3.13) and (4.2) as

$$Z = \int \prod_{i=1}^9 dA_i \prod_{k=1}^N d\alpha_k \Delta^{18}(\alpha) \delta(S_b) \delta\left(\frac{1}{N} \text{Tr}(A_i^2) - 1\right) \theta\left(\kappa - \frac{1}{N} \text{Tr}(A_0^2)\right), \quad (4.3)$$

where the extra factor $\Delta^2(\alpha)$ comes from the Fadeev-Popov procedure for the gauge fixing (3.9).

In the original Lorentzian type IIB matrix model, we have investigated the time-evolution of space-time with up to $N = 24$ [48], in which the exponential expansion of $R(t)$ is not clear because we can observed only so short time-evolution. Moreover we have studied the 6d version of the simplified model with up to $N = 64$ [49], in which we have found that $R(t)$ actually grows exponentially.

In order to explain how to determine values of the block size n introduced in (3.21), we plot the magnitude of the off-diagonal elements of A_i for $N = 64, 128, 256$ in Fig. 4.2. We find that the magnitude decreases rapidly as one goes away from diagonal elements. Moreover, the magnitude scales only for sufficiently large $|\alpha_a - \alpha_b|$. From these observations, we identify the block size n as the number of points in the region where the off-diagonal elements do not

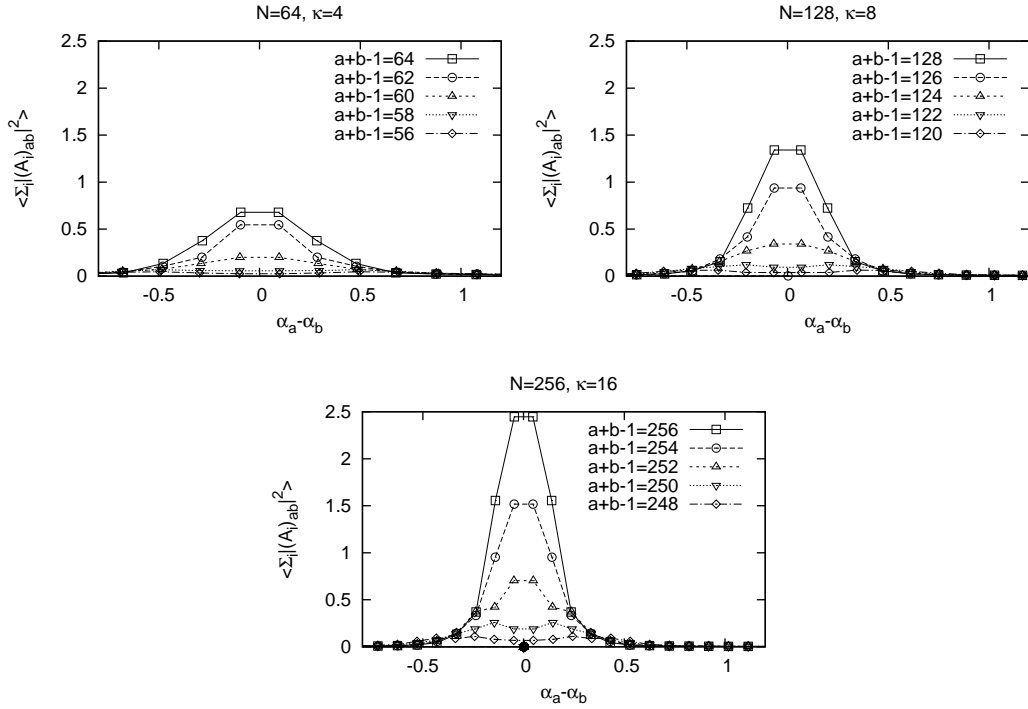


Figure 4.2: The magnitude $\sum_i |(A_i)_{ab}|^2$ of the off-diagonal elements of A_i is plotted against the time separation $\alpha_a - \alpha_b$ for $N = 64, 128$ and 256 with $\kappa = 4, 8$ and 16 , respectively. The scaling is observed only for sufficiently large $|\alpha_a - \alpha_b|$. For $N = 64$, we find 6 points in the region in which the scaling behavior is violated. Analogous plots for $N = 128, N = 256$ are shown in the other panels, where we find 10 points in the non-scaling region.

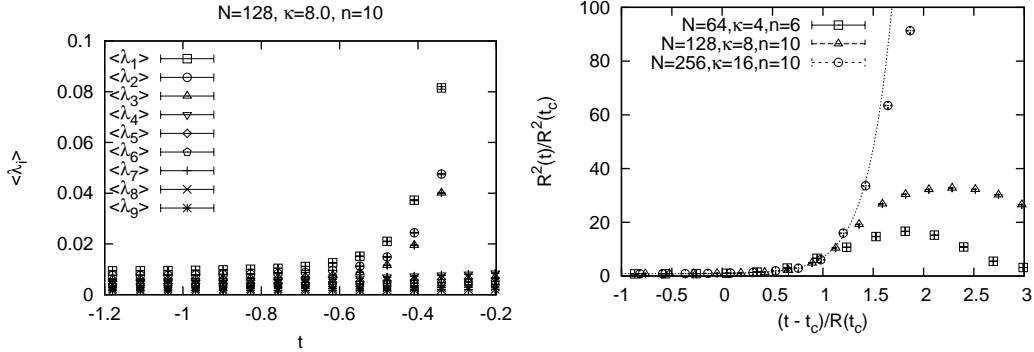


Figure 4.3: (Left) The nine eigenvalues of $T_{ij}(t)$ are plotted against time t for the simplified model with $N = 128$, $\kappa = 8.0$, $n = 10$ using the IR cutoffs (3.7) and (3.8). (Right) The extent of the space $R^2(t)$ normalized by $R^2(t_c)$ is plotted against $x = (t - t_c)/R(t_c)$ for the simplified model with $N = 64$, 128 and 256 using the IR cutoffs (3.7) and (3.8). The dashed line is a fit to $R^2(t)/R^2(t_c) = a + (1 - a) \exp(bx)$ with $N = 256$ for $0 \leq x \leq 1.3$, which gives $a = 0.89(3)$ and $b = 4.0(3)$.

scale.

Once the block size n is determined in this way, we can obtain the time-evolution. We show here results for the 10d version of the simplified model with up to $N = 256$. In Fig. 4.3 (Left), we plot the expectation values $\langle \lambda_i(t) \rangle$ of the nine eigenvalues of $T_{ij}(t)$ with $N = 128$, from which we obtained the value of critical time as $t_c = -0.63108(7)$ for $N = 128$. Applying the same procedure to another N , we find that the large- N scaling becomes less clear due to the finite N effects. However, these finite N effects can be absorbed by adjusting the values of t_c slightly from the one determined by the above argument.

Using t_c determined in this way, we plot the extent of space $R(t)$ normalized by $R(t_c)$ against t in Fig. 4.3 (Right), in which we find that the behavior of $R^2(t)$ at $t > t_c$ can be fitted well to an exponential function.

4.2 The simplified model for late times

In this subsection, we consider the second simplified model of the Lorentzian type IIB matrix model, which can be expected to describe the expanding behavior at late times. The model is defined as just a bosonic model in which the fermionic matrices are simply omitted. The partition function is given by

$$Z = \int dA e^{iS_b}. \quad (4.4)$$

In section 3.1 I reviewed an argument for the necessity of the temporal cutoff in the original model and the simplified model for early times. In the present case of the bosonic

model (4.4), the same argument implies that one does not have to introduce the temporal cutoff (3.7), and that we only need the spatial cutoff (3.8). Corresponding to (3.13), we can study the bosonic Lorentzian type IIB matrix model by simulating

$$Z = \int dA \delta \left(\frac{1}{N} \text{Tr} (F_{\mu\nu} F^{\mu\nu}) \right) \delta \left(\frac{1}{N} \text{Tr} (A_i)^2 - 1 \right) \quad (4.5)$$

$$= \int \prod_{i=1}^d dA_i \prod_{k=1}^N d\alpha_k \Delta^2(\alpha) \delta \left(\frac{1}{N} \text{Tr} (F_{\mu\nu} F^{\mu\nu}) \right) \delta \left(\frac{1}{N} \text{Tr} (A_i)^2 - 1 \right), \quad (4.6)$$

which requires computational efforts comparable to the simplified model for early times reviewed in the previous section. We have used a large-scale parallel computer to simulate the model (4.6) with the matrix size up to $N = 512$, which enables us to investigate a long time-evolution. See Appendix A for the details of the simulation.

In order to show that there is no need to introduce temporal cutoffs in the bosonic model, we measure the quantity $\langle \frac{1}{N} \text{Tr} (A_0)^2 \rangle$, which represents the extent of the eigenvalue distribution of A_0 . As we mentioned above, it turns out that this quantity keeps to be finite in the model (4.6) although we do not introduce a cutoff in the temporal direction such as (3.7). In Fig. 4.4 (Left) we plot the results against N . At small N , it is almost independent of N . However, for $N \geq N_c = 112$, it begins to increase linearly with N . At this time, the behavior for the spatial direction also drastically changes. In order to see its N dependence, we plot the expectation values $\langle \lambda_i(t) \rangle$ of the nine eigenvalues of $T_{ij}(t)$ evaluated at $t = t_{\text{peak}}$ where $R^2(t)$ becomes maximum in Figure 4.4 (Right)⁴. For small N , there is no significant gap between the nine eigenvalues, whereas for $N \geq N_c$, we observe a big gap between $\langle \lambda_3(t_{\text{peak}}) \rangle$ and $\langle \lambda_4(t_{\text{peak}}) \rangle$. As was explained in previous section, this significant implies the spontaneous breaking of the rotational symmetry of the 9d space. We will see that the SO(9) symmetry is broken down to SO(3) after a critical time similarly to the original Lorentzian type IIB matrix model.

4.2.1 Properties of the bosonic model for $N < N_c$

In this sub-subsection we discuss the properties of the bosonic model for $N < N_c$. In order to extract the time-evolution, we need to determine the block size n to be used in eq. (3.21). In Fig. 4.5 (Left) we plot the magnitude of the off-diagonal elements of A_i against the time separation $\alpha_a - \alpha_b$ for $N = 110$. The origin in the horizontal axis corresponds to the diagonal elements. We observe a nice scaling behavior for all the matrix elements. However, the magnitude falls off rather smoothly as one goes in the off-diagonal direction, which means

⁴In order to define $R^2(t)$ and $T_{ij}(t)$, we have to specify the block size n to be used in eq. (3.21). See sections 4.2.1 and 4.2.2 for the actual values of n used to obtain the results in Fig. 4.4 (Right).

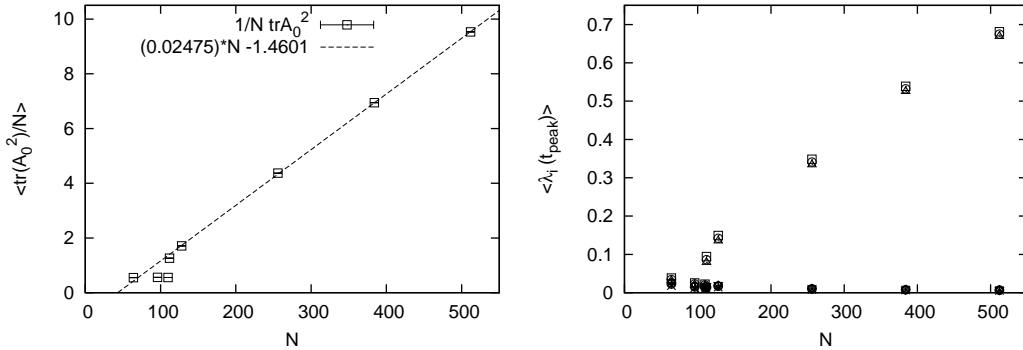


Figure 4.4: (Left) The extent $\langle \frac{1}{N} \text{Tr}(A_0)^2 \rangle$ of the eigenvalue distribution of A_0 is plotted against N . (Right) The expectation values $\lambda_i(t)$ of the nine eigenvalues of $T_{ij}(t)$ at $t = t_{\text{peak}}$ are plotted against N . For $N < N_c = 112$, the nine eigenvalues are close to each other, whereas for $N \geq N_c$, three out of the nine eigenvalues become much larger than the others.

that the dominant matrix configurations do not have a band-diagonal structure.

In this situation, we cannot naturally define the block matrices (3.21) representing the state at each time and hence the notion of time-evolution becomes obscure. Indeed, we have shown that the temporal direction does not extend with N increased. Let us nevertheless try to extract the time-evolution using $n = 14$ as the block size, which is the value obtained for $N = N_c = 112$ in the way described in the next section. In Fig. 4.5 (Right) we plot the expectation values $\langle \lambda_i(t) \rangle$ for $N = 110$. It turns out that there is only little t -dependence, and there is no clear gap between the eigenvalues for all t .

The situation for smaller N is similar to the $N = 110$ case. In Fig. 4.6 we plot the extent of space $R^2(t)$ as a function of t for $N = 64, 96$ and 110 obtained with the same block size $n = 14$. The dependence on N turns out to be modest.

4.2.2 Properties of the bosonic model for $N \geq N_c$

In this sub-subsection we study the properties of the bosonic model for $N \geq N_c$. In Fig. 4.7 (Left) we plot the magnitude of the off-diagonal elements of A_i for $N = 128$. We find that the magnitude decreases rapidly as one goes away from diagonal elements. Moreover, the magnitude scales only for sufficiently large $|\alpha_a - \alpha_b|$. From this observation, we identify the block size n as the number of points in the region where the off-diagonal elements do not scale. (In the present $N = 128$ case, we obtain $n = 20$. See below for more detail.)

Using the block size n determined in this way, we can obtain the time-evolution. In Fig. 4.7 (Right) we plot the expectation values $\langle \lambda_i(t) \rangle$ for $N = 128$. In contrast to the situation for $N < N_c$, we observe the spontaneous symmetry breaking from $\text{SO}(9)$ to $\text{SO}(3)$

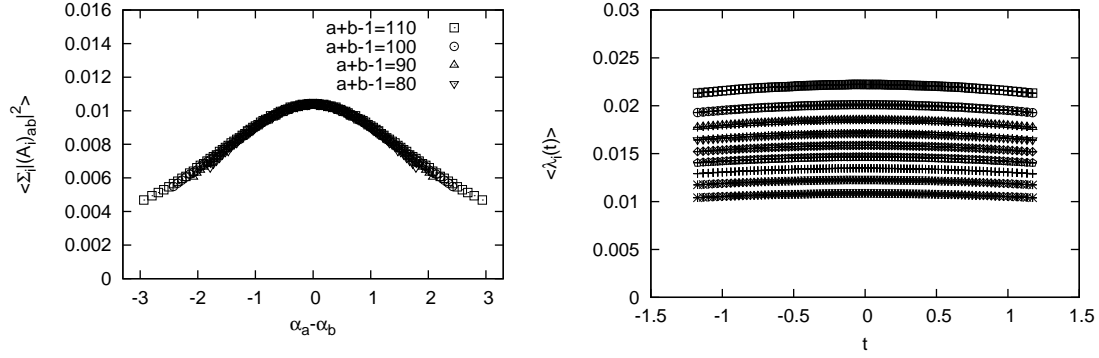


Figure 4.5: (Left) The magnitude $\sum_i |(A_i)_{ab}|^2$ of the off-diagonal elements of A_i is plotted against the time separation $\alpha_a - \alpha_b$ for $N = 110$. (Right) The expectation values $\langle \lambda_i(t) \rangle$ of the nine eigenvalues of $T_{ij}(t)$ are plotted against t for $N = 110$. The block size is chosen to be $n = 14$.

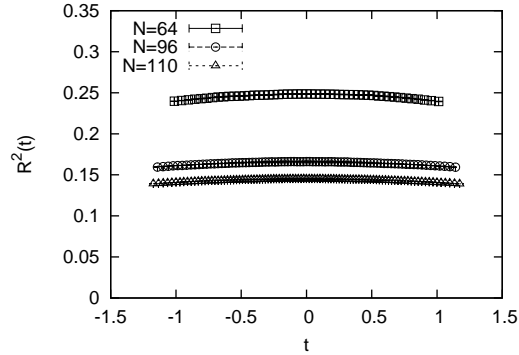


Figure 4.6: The extent of space $R^2(t)$ is plotted against t for $N = 64, 96$ and 110 . The block size is chosen to be $n = 14$ for all N .

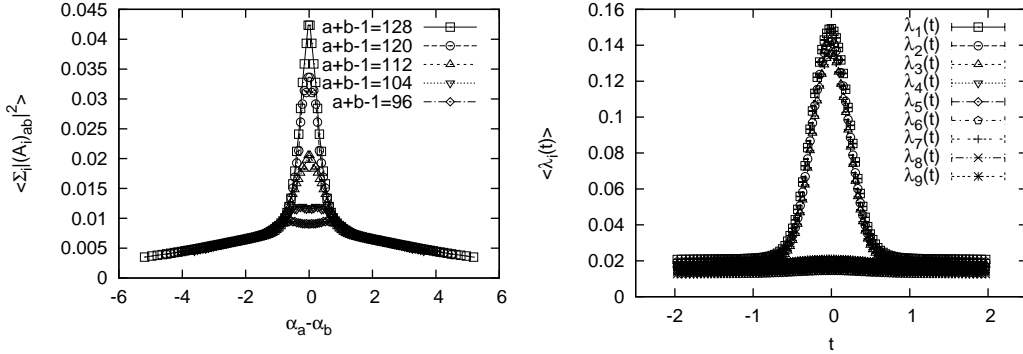


Figure 4.7: (Left) The magnitude $\sum_i |(A_i)_{ab}|^2$ of the off-diagonal elements of A_i is plotted against the time separation $\alpha_a - \alpha_b$ for $N = 128$. The scaling is observed only for sufficiently large $|\alpha_a - \alpha_b|$. (Right) The expectation values $\langle \lambda_i(t) \rangle$ of the nine eigenvalues of $T_{ij}(t)$ are plotted against t for $N = 128$ with the block size $n = 20$.

at a critical time t_c similarly to the original Lorentzian type IIB matrix model.⁵

In order to study the large- N scaling property, we perform simulation for $N = 256, 384, 512$ as well. In Fig. 4.8 (Top-Left) we zoom up the region near the origin in Fig. 4.7 (Left). From this figure, we determine the block size for $N = 128$ to be $n = 20$. Similarly, from the other figures in Fig. 4.8, we determine the block size for $N = 256, N = 384$ and 512 to be $n = 24, n = 28$ and 32 , respectively.

The definition of the critical time t_c is ambiguous at finite N . See Fig. 4.9 (Left), where we plot the expectation values $\langle \lambda_i(t) \rangle$ of the eigenvalues of $T_{ij}(t)$ against t for $N = 512$. For instance, the critical time t_c obtained in this way for $N = 512$ from Fig. 4.9 (Left) is $t_c = -0.76559(7)$. Similarly we obtain $t_c = -0.76930(7)$ for $N = 384$. Applying the same procedure to smaller N , we find that the large- N scaling behavior in Fig. 4.9 (Right) becomes less clear due to finite N effects. We absorb these finite N effects by adjusting the value of t_c slightly⁶ from the one determined from the above procedure. As is proposed in the original Lorentzian type IIB matrix model [35], we use the extent of space $R(t_c)$ at the critical time to fix the scale. Explicit values of $R(t_c)$ are given in table 1 together with the block size n and the critical time t_c for each N .

In Fig. 4.9 (Right) the extent of space $R^2(t)$ is plotted against t . The large- N scaling behavior is observed by shifting the time coordinate so that the critical time comes to the origin and by plotting dimensionful quantities in units of $R(t_c)$. The observed large- N scaling

⁵The fact that the spatial dimensionality after the spontaneous symmetry breaking turned out to be the same as in the original model is understandable from the view point of the mechanism suggested in ref. [35], which involves only the boson part of the action.

⁶For $N = 256$, we shift by two data points and use $t_c = -0.82166(6)$ instead of $t_c = -0.76987(6)$. Similarly, for $N = 128$, we shift by four data points and use $t_c = -0.89472(7)$ instead of $t_c = -0.75798(7)$.

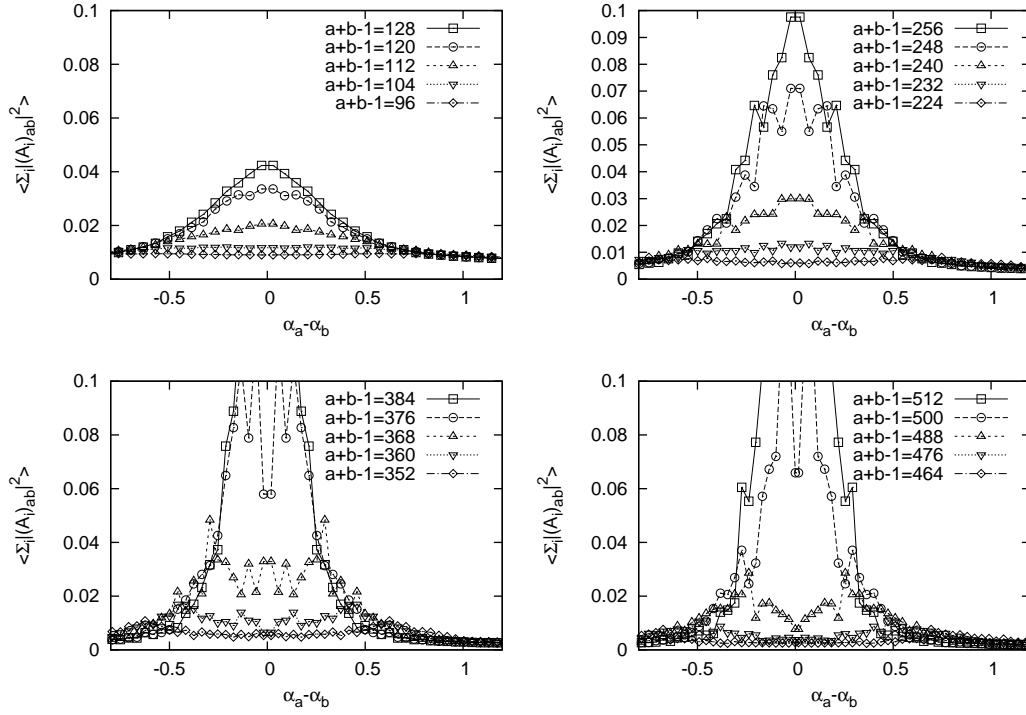


Figure 4.8: (Top-Left) The zoom up of the region near the origin in Fig. 4.7 (Left). We find 20 points in the region in which the scaling behavior is violated. Analogous plots for $N = 256$, $N = 384$, $N = 512$ are shown in the other panels, where we find 24, 28, 32 points in the non-scaling region, respectively.

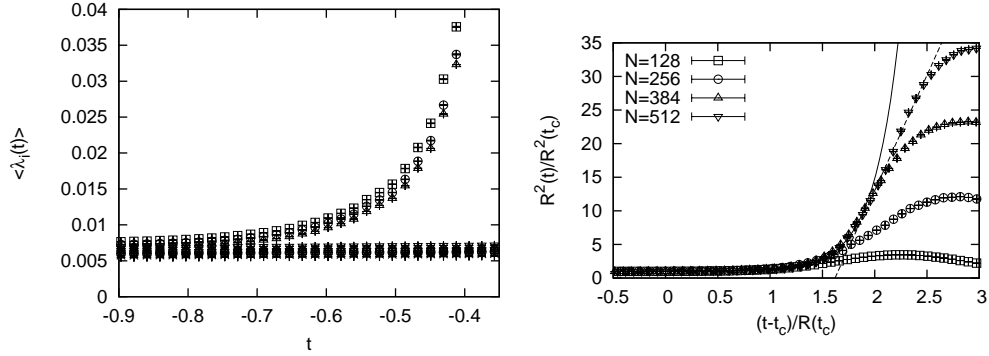


Figure 4.9: (Left) The expectation values $\langle \lambda_i(t) \rangle$ of the nine eigenvalues of $T_{ij}(t)$ are plotted against t for $N = 512$ with the block size $n = 32$. (Right) The extent of space $R^2(t)$ normalized by $R^2(t_c)$ is plotted against $x = (t - t_c)/R(t_c)$ for $N = 128, 256, 384$ and 512 . See table 1 for the values of the block size n , the critical time t_c and the extent of space $R(t_c)$ at the critical time, which are used to make this plot. The solid line is a fit of the $N = 512$ data to $R^2(t)/R^2(t_c) = a + (1 - a) \exp(bx)$ for $1.0 \leq x \leq 1.85$, which gives $a = 0.9957(5)$ and $b = 4.03(7)$. The dashed line is a fit of the $N = 512$ data to $R^2(t)/R^2(t_c) = cx + d$ for $1.85 \leq x \leq 2.5$, which gives $c = 34.3(6)$ and $d = -55(1)$.

shows that the theory one obtains in the large- N limit is characterized by one scale parameter $R(t_c)$ and it does not contain any dimensionless parameters.

It turns out that the behavior of $R^2(t)$ at $t > t_c$ can be fitted to an exponential function only for a finite range. At later times, it can be fitted well by a straight line, which corresponds to the power-law expansion

$$R(t) \propto t^{1/2}. \quad (4.7)$$

Note that this behavior is observed within the scaling region, which implies that the suggested power law persists in the large- N limit at least for some time region. In Appendix B we present the results for the (5+1)D version of the bosonic type IIB matrix model. While we observe qualitatively the same behaviors, there are also some interesting quantitative differences.

In order to understand the observed large- N scaling further, we investigate how the continuum limit and the infinite volume limit in the temporal direction are achieved in the large- N limit. Here we restrict ourselves to $N \geq 256$ since $N = 128$ is too close to the critical value $N_c = 112$. As the “lattice spacing” in the temporal direction, we consider the separation of data points in Fig. 4.9 (Right) in the horizontal direction. This quantity is actually t -dependent, and it can be defined more explicitly as $\frac{\delta t}{R(t_c)}$, where δt is the difference of (3.22) between adjacent blocks. In Fig. 4.10 (Left) we plot this t -dependent “lattice spacing”, choosing the horizontal axis to be the same as in Fig. 4.9 (Right). We find clear tendency that the “lattice spacing” at the same point on the horizontal axis decreases as N

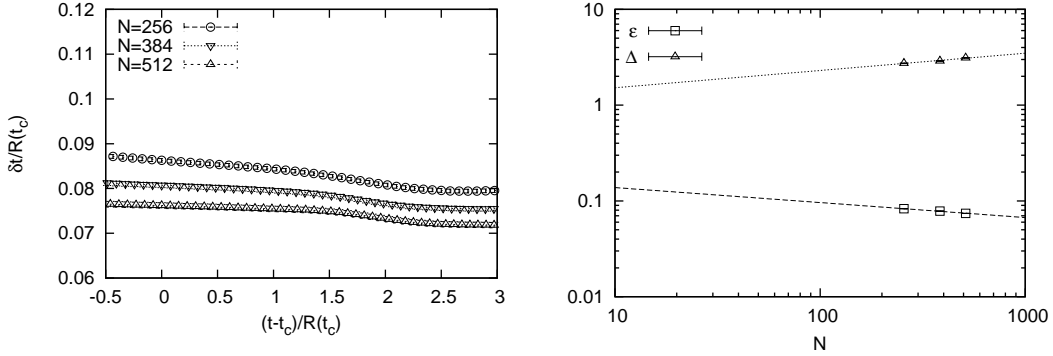


Figure 4.10: (Left) The “lattice spacing” $\frac{\delta t}{R(t_c)}$ is plotted against $(t - t_c) / R(t_c)$. (Right) The average “lattice spacing” ϵ and the “volume” in the temporal direction Δ_t is plotted against N in the log scale. The straight lines represent fits to the power-law behaviors $\epsilon = a N^{-p}$, where $a = 0.20(1)$, $p = 0.16(1)$ and $\Delta_t = b N^q$, where $b = 1.0(2)$, $q = 0.18(3)$.

increases. As the “volume” in the temporal direction, we define

$$\Delta_t \equiv \frac{t_{\text{peak}} - t_c}{R(t_c)}. \quad (4.8)$$

Using this quantity, we can also define an average “lattice spacing” $\epsilon = \Delta_t / \nu$, where ν is the number of data points within the region $[t_c, t_{\text{peak}}]$. The values of ϵ and Δ_t obtained for each N are given in table 1. We find that the average “lattice spacing” ϵ decreases and the “volume” increases as N becomes large. In Fig. 4.10 (Right) we plot ϵ and Δ_t against N in the log scale. The straight lines represent fits to the power-law behaviors, although the behaviors may be subject to a qualitative change at larger N . In particular, it is an interesting dynamical question whether $\Delta_t \rightarrow \infty$ or $\Delta_t \rightarrow \text{const.}$ in the large- N limit. In the former case, the expansion of space continues forever, since the time t_{peak} at the peak cannot be reached within a finite time. In the latter case, on the other hand, the space stops expanding in a finite time and starts to shrink. By addressing this issue in the original model, one can, in principle, predict the fate of our Universe.

5 The IR cutoff dependence of the expanding behavior

In section 4, we have shown that the emergent 3d space expands exponentially and the behavior changes into the power-law expansion in the simplified models. However, let us recall that we have to introduce IR cutoffs in the models since the partition function diverges due to the unbounded action. Indeed, it turned out that each term in the boson action (3.6) diverges without any IR cutoffs, which makes the path integral ill-defined. We can regularize

N	n	t_c	$R(t_c)$	ε	Δ_t
128	20	-0.89472(7)	0.39270(2)	—	—
256	24	-0.82166(6)	0.30045(3)	0.08297(2)	2.7380(7)
384	28	-0.76930(7)	0.26580(3)	0.07823(2)	2.8943(6)
512	32	-0.76559(7)	0.24578(3)	0.07417(2)	3.1150(7)

Table 1: The block size n , the critical time t_c and the extent of space $R(t_c)$ at the critical time, which are used to make the plot in Fig. 4.9 (Right). We also present the explicit values of the average “lattice spacing” ε and the “volume” Δ_t in the temporal direction, which are plotted in Fig. 4.10 (Right).

this divergence by restricting the extent of the eigenvalue distribution of A_μ . For instance, one can consider the regularization such as $\text{Tr} (A_\mu^2) \leq \Lambda^2$. However, since $\text{Tr} (A_\mu^2)$ involves positive and negative terms, it is reasonable to introduce IR cutoffs separately in $\text{Tr} (A_0^2)$ and $\text{Tr} (A_i^2)$ as in (3.7) and (3.8).

However, the results obtained in this way will involve some cutoff effects in a finite volume and depend on ways to regularize the model. Since we have not yet taken the infinite volume limit in obtaining the results shown in the previous section. it is considered that they are affected by the IR cutoffs. Thus, it is important to study the IR cutoff dependence in the infinite volume limit. Especially, because the extent of the eigenvalue distribution of matrices, which corresponds to the volume, is determined dynamically in the matrix model, it is not obvious that the cutoff effects disappear in the infinite volume limit. Hence, in this section, we study the IR cutoff dependence of the expending behavior. To see this, we first generalize the form of the IR cutoffs by introducing a parameter and then discuss the dependence on it in the infinite volume limit.

5.1 Generalization of the form of the IR cutoffs

In this thesis, we have considered the IR cutoffs (3.7) and (3.8). However, it is not obvious whether their effects disappear in the infinite volume limit. Note that the cutoffs (3.7) and (3.8) affect all the components of A_μ , that appear not only near the boundaries but also in the bulk of emergent space-time. Therefore, it is necessary for the effects in the bulk to disappear in the infinite volume limit.

In order to investigate the IR cutoff dependence of $R(t)$, we generalize the cutoffs (3.7) and (3.8) as

$$\frac{1}{N} \text{Tr} (A_0^2)^p \leq (\kappa L^2)^p, \quad (5.1)$$

$$\frac{1}{N} \text{Tr} (A_i^2)^p \leq L^{2p}, \quad (5.2)$$

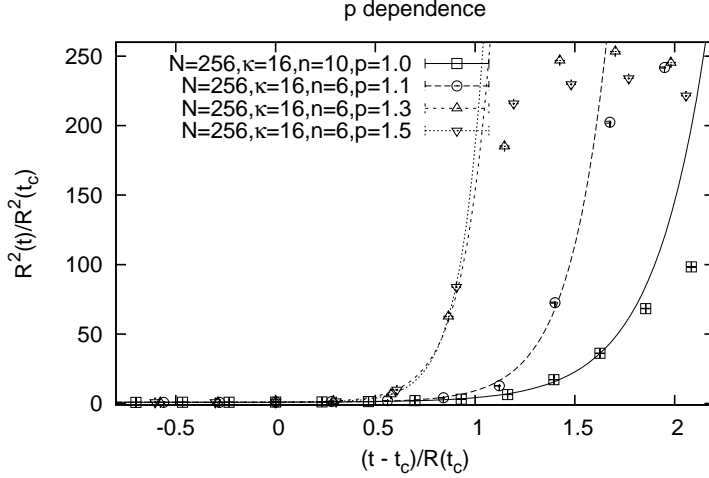


Figure 5.1: The extent of the space $R^2(t)$ normalized by $R^2(t_c)$ is plotted against $x = (t - t_c)/R(t_c)$ with $N = 256$ and $\kappa = 16$ for $p = 1.0, 1.1, 1.3$ and 1.5 . We have used the block size $n = 10$ for $p = 1.0$ and $n = 6$ for $p = 1.1, 1.3$ and 1.5 . The lines are fits to $R^2(t)/R^2(t_c) = a + (1 - a) \exp(bx)$. We present given values of a and b in table 2.

where the parameter p is real and $p = 1$ corresponds to the cutoff used so far. In particular, for sufficiently large p , the above cutoffs can be approximated by

$$\begin{aligned} \frac{1}{N} |\alpha_{\max}^p| &\leq (\kappa L^2)^p, \\ \frac{1}{N} |\lambda_{\max}^p| &\leq L^{2p}, \end{aligned}$$

where α_{\max} and λ_{\max} are the maximum eigenvalues of A_0^2 and $\sum_i A_i^2$. Therefore, the IR cutoff effects come to localize at the boundary of the emergent space-time as p is increased, and they will affect A_μ only at the boundary for sufficiently large p . We observe that the IR cutoff effects indeed exist in the bulk for $p = 1$ even in the infinite volume limit. As a result, it turns out that the expanding behavior depends on p . We will also show that this dependence disappears as one increases p .

5.2 The p dependence of $R(t)$

In the previous section, we have shown the result obtained for $p = 1$ in the simplified model for early times, and it is confirmed that the emergent 3d space continues to expand exponentially with much larger N . In this subsection, we study how $R(t)$ depends on p with sufficiently large volume.

N	κ	p	n	t_c	$R(t_c)$	a	b
256	16	1.0	10	-0.58208(7)	0.04669(07)	0.923(16)	3.77(15)
256	16	1.1	6	-0.39307(6)	0.03213(14)	0.956(20)	5.23(37)
256	16	1.3	6	-0.29213(8)	0.03055(11)	0.876(35)	7.10(37)
256	16	1.5	6	-0.23593(7)	0.02579(02)	0.952(07)	8.24(19)

Table 2: The block size n , the critical time t_c and the extent of space $R(t_c)$ at critical time, which is used to make the plot in figure 5.1. We also present the values of a and b , which are given by fitting $R^2(t)/R^2(t_c)$ to $f(x) = a + (1-a)\exp(bx)$ with $x = (t-t_c)/R(t_c)$ for each p .

In Fig. 5.1 we plot the extent of space $R^2(t)/R(t_c)$ against t for various values of p for the simplified model for early times with $N = 256$. We find that the result depends on p , although the qualitative behavior (exponential expansion) remains the same as $p = 1.0$., We also notice that the results for $p = 1.3$ and 1.5 are close to each other expect at large t . Therefore, it is suggested that the IR cutoff effects disappear for sufficiently large p in the infinite volume limit. This can be understood since the cutoffs come to affect $R(t)$ only at the boundary as p is increased. In fact, the behavior of $R(t)$ for $p = 1.3$ and 1.5 are different around the peak. From these considerations, we conclude that the values of p should be taken sufficiently large that the expanding behavior of $R(t)$ does not depend on p in the infinite volume limit.

5.3 The Schwinger-Dyson equations in the simplified model

In order to get a better understanding of the above result, we try to see the IR cutoff effects more directly by using the Schwinger-Dyson equations. Before we consider this, let us explain how to deal with the constraints introduced in the Lorentzian type IIB matrix model. As shown in section 3, the partition function of the model is given as

$$\begin{aligned}
Z = & \int \prod_{k=1}^N d\alpha_k \prod_{i=1}^9 dA_i \Delta^2(\alpha) \text{Pf} \mathcal{M}(A) \delta \left(\frac{1}{N} \text{Tr} (F_{\mu\nu} F^{\mu\nu}) \right) \\
& \times \delta \left(\frac{1}{N} \text{Tr} [(A_i^2)^p] - 1 \right) \theta \left(\kappa - \frac{1}{N} \text{Tr} [(A_0^2)^p] \right), \quad (5.3)
\end{aligned}$$

where the first delta function respects the effect of $\exp(iS_b)$ and the second one comes from the IR cutoff in the spatial direction. The step function represents the IR cutoff in the temporal direction.

When one deals with this model numerically, it is convenient to replace these delta functions and the step function by Gaussian potentials. We denote these potentials as $S_{\text{tr}F}$, $S_{\text{tr}A_i}$

and $S_{\text{tr}A_0}$, and they are given by

$$S_{\text{tr}F} = \frac{\gamma_C N^2}{2} \left(\frac{1}{N} \text{tr} F_{\mu\nu} F^{\mu\nu} \right)^2, \quad (5.4)$$

$$S_{\text{tr}A_i} = \frac{\gamma_L N^2}{2} \left(\frac{1}{N} \text{tr} [(A_i^2)^p] - 1 \right)^2, \quad (5.5)$$

$$S_{\text{tr}A_0} = \frac{\gamma_\kappa N^2}{2} \left(\frac{1}{N} \text{tr} [(A_0^2)^p] - \kappa^p \right)^2, \quad (5.6)$$

where coefficients γ_C , γ_L and γ_κ are taken to be large enough for the potentials to constrain the configuration well. Note that $S_{\text{tr}A_0}$ becomes

$$S_{\text{tr}A_0} = \frac{\gamma_\kappa N^2}{2} \left(\frac{1}{N} \sum_{a=1}^N \alpha_a^{2p} - \kappa^p \right)^2 \quad (5.7)$$

in the gauge (3.9). The Fadeev-Popov determinant and the Pfaffian in the partition function gives rise to a term

$$S_{\text{Pf+g.f.}} = -\ln [\Delta^2(\alpha) \text{Pf}\mathcal{M}(A)] \quad (5.8)$$

in the action. Using the terms⁷ (5.4), (5.5), (5.7) and (5.8), the partition function (5.3) becomes

$$Z = \int \prod_{a=1}^N d\alpha_a \prod_{i=1}^9 dA_i \exp[-S], \quad (5.9)$$

$$S = S_{\text{tr}F} + S_{\text{tr}A_i} + S_{\text{tr}A_0} + S_{\text{Pf+g.f.}}. \quad (5.10)$$

In particular, when we consider the simplified model for early times, from (4.2) the term (5.8) takes a simple form

$$S_{\text{Pf+g.f.}} = -18 \sum_{a>b} \ln(\alpha_a - \alpha_b). \quad (5.11)$$

In what follows, we consider the simplified model for early times, in which the term involving the Pfaffian (5.11) depends only on A_0 .

Then, let us study the IR cutoff effects in the model using the Schwinger-Dyson equations.

⁷In fact, we have also introduced another potential besides the above in order to stabilize a peak of $R(t)$ at the origin in simulations. Therefore, the Schwinger-Dyson equations in practice includes the term arising from this potential. However, since its effect is negligibly small compared to the other terms, we here dropped this term from the S-D eq. for simplicity.

For the given action (5.10), we consider the S-D equations

$$\frac{1}{Z} \int dA \frac{\delta}{\delta (A^\mu)_{kl}} \left(\mathcal{O}(A) e^{-S[A]} \right) = 0. \quad (5.12)$$

When one considers the case of $\mathcal{O}(A) = 1$, we obtain

$$\left\langle \frac{\delta S_{\text{tr}F}}{\delta (A^\mu)_{kl}} \right\rangle + \left\langle \frac{\delta S_{\text{tr}A_i}}{\delta (A^\mu)_{kl}} \right\rangle + \left\langle \frac{\delta S_{\text{tr}A_0}}{\delta (A^\mu)_{kl}} \right\rangle + \left\langle \frac{\delta S_{\text{Pf+g.f.}}}{\delta (A^\mu)_{kl}} \right\rangle = 0.$$

When the index μ takes a value corresponding to the spatial directions, however, each term in the l.h.s of the above equation is explicitly zero due to the SO(9) rotational symmetry of the model. Therefore, we consider $\mathcal{O}(A) = A_\mu$ as the simplest case giving nontrivial relations. By plugging in the action (5.10), we obtain the relations such as

$$\left\langle (A^I)_{KL} \frac{\delta S_{\text{tr}F}}{\delta (A^i)_{kl}} \right\rangle + \left\langle (A^I)_{KL} \frac{\delta S_{\text{tr}A_i}}{\delta (A^i)_{kl}} \right\rangle = \left\langle \frac{\partial (A^I)_{KL}}{\partial (A^i)_{kl}} \right\rangle, \quad (5.13)$$

$$\left\langle \alpha_K \frac{\delta S_{\text{tr}F}}{\delta \alpha_k} \right\rangle + \left\langle \alpha_K \frac{\delta S_{\text{Pf+g.f.}}}{\delta \alpha_k} \right\rangle + \left\langle \alpha_K \frac{\delta S_{\text{tr}A_0}}{\delta \alpha_k} \right\rangle = \left\langle \frac{\partial \alpha_K}{\partial \alpha_k} \right\rangle, \quad (5.14)$$

where $I = 1, \dots, 9$ is an index for SO(9) and $K, L = 1, \dots, N$ are indices for SU(N). The upper equation is given for $\mathcal{O}(A) = A_i$ and the lower one is given for $\mathcal{O}(A) = A_0$. In order for each term in eq. (5.13) to have a non-zero value, we need to contract the indices for SO(9) and SU(N), which gives

$$\sum_{i=1}^9 \sum_{l=L}^N \left(\left\langle (A^i)_{KL} \frac{\delta S_{\text{tr}F}}{\delta (A^i)_{kl}} \right\rangle + \left\langle (A^i)_{KL} \frac{\delta S_{\text{tr}A_i}}{\delta (A^i)_{kl}} \right\rangle \right) = 9N \left(1 - \frac{1}{N^2} \right) \delta_{kK}, \quad (5.15)$$

$$\left\langle \alpha_K \frac{\delta S_{\text{tr}F}}{\delta \alpha_k} \right\rangle + \left\langle \alpha_K \frac{\delta S_{\text{Pf+g.f.}}}{\delta \alpha_k} \right\rangle + \left\langle \alpha_K \frac{\delta S_{\text{tr}A_0}}{\delta \alpha_k} \right\rangle = \delta_{kK} - \frac{1}{N}. \quad (5.16)$$

To calculate the derivative with respect to $(A_i)_{kl}$, we used the generators t^a ($a = 1, \dots, N^2 - 1$) of SU(N) group with the normalization

$$\text{tr} \left(t^a t^b \right) = \delta^{ab}$$

and the relation

$$t_{ij}^a t_{kl}^a = \delta_{il} \delta_{jk} - \frac{1}{N} \delta_{ij} \delta_{kl}.$$

The bosonic matrices are decomposed using these generators as

$$(A_\mu)_{ij} = t_{ij}^a A_\mu^a.$$

Note that both sides of eq. (5.15) and (5.16) are $N \times N$ matrices; namely, every component in the matrices has to satisfy the relation. Therefore, one can confirm the consistency of the simulation by evaluating the equation for each component.

In the context of the Schwinger-Dyson analysis, the IR cutoff effects can be read off from the corresponding term. If the term arising from the cutoff is zero by itself, it does not affect the other terms in the S-D equation. This means that such a cutoff does not influence the physical quantities obtained from the simulation. However, the terms arising from the cutoffs will have some non-zero values for finite N because there should be some effects of regularizing the model. It is important that such effects disappear in an appropriate limit. In our case, it is expected that the IR cutoff effects appear significantly at the boundaries of the emergent space-time because its expansion is controlled by the cutoffs. Here, what we mean by is the peak of $R(t)$ and edges in the temporal direction. However, we have observed the quantitative behavior of $R(t)$ depends on p in the IR cutoffs. This observation indicates that their effects appear even in the bulk of the emergent space-time and influence its expanding behavior. On the other hand, for a certain values of p , $R(t)$ seems to be independent of the IR cutoffs, which indicates that their effects disappear in the bulk. In order to confirm these statements, we then investigate the IR cutoff effects in the emergent space using the S-D equations.

We explain how to read off the IR cutoff effects in the emergent space-time from the S-D eq. (5.15) and (5.16). Let us denote each term in these equations by

$$\begin{aligned} \frac{1}{9N} \sum_{i=1}^9 \sum_{m=1}^N \left\langle (A^i)_{jm} \frac{\delta S_{\text{tr}F}}{\delta (A^i)_{km}} \right\rangle &\equiv C_{jk}^{(\text{b})}, \\ \frac{1}{9N} \sum_{i=1}^9 \sum_{m=1}^N \left\langle (A^i)_{jm} \frac{\delta S_{\text{tr}A_i}}{\delta (A^i)_{km}} \right\rangle &\equiv C_{jk}^{(\text{cutoff})}, \end{aligned} \quad (5.17)$$

$$\left\langle \alpha_k \frac{\delta S_{\text{tr}F}}{\delta \alpha_k} \right\rangle = D_k^{(\text{b})}, \quad \left\langle \alpha_k \frac{\delta S_{\text{Pf+g.f.}}}{\delta \alpha_k} \right\rangle \equiv D_k^{(\text{f})}, \quad \left\langle \alpha_k \frac{\delta S_{\text{tr}A_0}}{\delta \alpha_k} \right\rangle \equiv D_k^{(\text{cutoff})}. \quad (5.18)$$

Note that we have gauge fixed the $SU(N)$ symmetry by requiring that A_0 is diagonal and its eigenvalues α_k are ordered in time. Therefore, $D_k^{(\text{cutoff})}$ represents the temporal cutoff effect at time α_k . Similarly, taking into account the fact that A_i is band-diagonal in this basis, we can think that the diagonal element of $C_{kk}^{(\text{cutoff})}$ represents the spatial cutoff effect at time α_k . For a given α_k , we then denote the corresponding C_{kk} and D_k given for the same k by $C(\alpha)$

and $D(\alpha)$, respectively. Thus, for the diagonal part of these matrices, the S-D eq. (5.15) and (5.16) become

$$C^{(b)}(\alpha) + C^{(\text{cutoff})}(\alpha) = 1 - \frac{1}{N^2}, \quad (5.19)$$

$$D^{(b)}(\alpha) + D^{(f)}(\alpha) + D^{(\text{cutoff})}(\alpha) = 1 - \frac{1}{N}. \quad (5.20)$$

By evaluating the cutoff terms $C^{(\text{cutoff})}(\alpha)$ and $D^{(\text{cutoff})}(\alpha)$, we can investigate the IR cutoff effects in the emergent space-time.

In Fig. 5.2, we plot $C^{(b)}(\alpha)$, $C^{(\text{cutoff})}(\alpha)$ and their sum against $\alpha_k \leq 0$ with the matrix size $N = 32$ and $\kappa = 6^p$ for $p = 0.5, 1.0$ and 1.5 . This figure shows that the sum of the two terms actually satisfies the spatial S-D equation (5.19) at every α_k . In this figure, the boundary in the temporal direction corresponds to the smallest α_k . On the other hand, the boundary in the spatial directions exists at $\alpha_k = 0$, where $R(t)$ has a peak. In other words, the region going away from the peak corresponds to the bulk. Therefore, $C^{(\text{cutoff})}(\alpha)$ becomes larger as one gets close to $\alpha_k = 0$. Also, it turns out that $C^{(\text{cutoff})}(\alpha)$ in the bulk becomes small as p is increased. This observation shows that the IR cutoff effect in the bulk is suppressed as p increases.

As for the temporal direction, we can calculate the explicit form of $D^{(\text{cutoff})}(\alpha)$ and obtain

$$D^{(\text{cutoff})}(\alpha) \sim c\alpha_k^{2p}, \quad (5.21)$$

where the coefficient is

$$c = 2p\gamma_\kappa N \left[\frac{1}{N} \sum_j \alpha_j^{2p} - \kappa^p \right].$$

In Fig. 5.3, we plot $D^{(b)}(\alpha)$, $D^{(f)}(\alpha)$, $D^{(\text{cutoff})}(\alpha)$ and their sum against α_k^{2p} for $\alpha_k \geq 0$ with the matrix size $N = 32$ and $\kappa = 6^p$ for $p = 0.5, 1.0$ and 1.5 . This figure also shows that the sum of the three terms actually satisfies the temporal S-D equation (5.20) at every α_k . In this figure, the boundary in the temporal direction corresponds to the largest α_k , at which the $D^{(\text{cutoff})}(\alpha)$ becomes largest for each p . Especially, we find that $D^{(\text{cutoff})}(\alpha)$ is in fact proportional to α_k^{2p} as we find in (5.21), which means that one can suppress the temporal IR cutoff effect in the bulk by increasing p as well as the spatial cutoff. For sufficiently large p , it is expected that the effect comes to exist only around the boundary $(\alpha_k)_{\text{max}}$.

The above observations are consistent with the results shown in Fig. 5.1, in which the expanding behaviors of $R(t)$ for $p = 1.0$ and 1.1 are different from the ones for $p \geq 1.3$. The results suggest that the IR cutoff effects remain in the bulk for $p \leq 1.1$, while the ones for

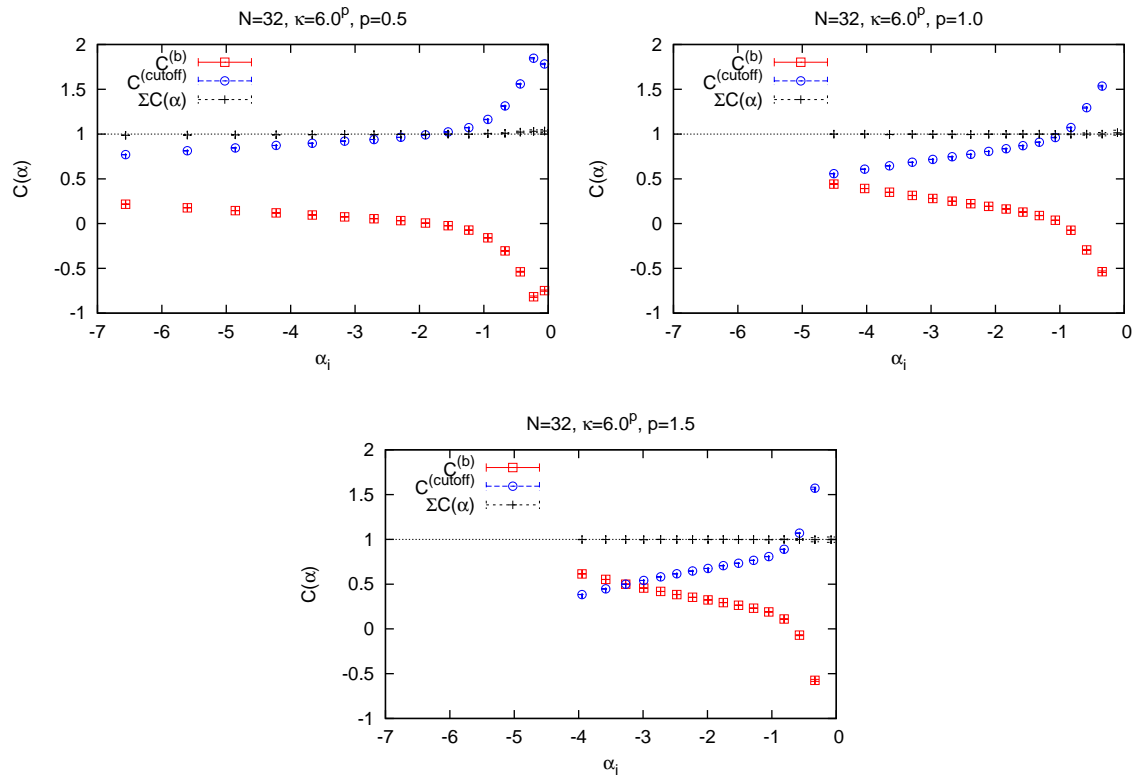


Figure 5.2: (Top-Left) $C^{(b)}(\alpha)$ and $C^{(\text{cutoff})}(\alpha)$ in the spatial S-D eq. (5.19) are plotted against $\alpha_k \leq 0$ for $p = 0.5$ with $N = 32$ and $\kappa = 6^p$, in which the boundary in the spatial direction exist at $\alpha_k = 0$ which $R(t)$ has a peak. We also plot the sum of $C^{(b)}(\alpha)$ and $C^{(\text{cutoff})}(\alpha)$ which becomes $1 - \frac{1}{N^2}$ for every α_k . Similarly, $C^{(b)}(\alpha)$ and $C^{(\text{cutoff})}(\alpha)$ and their sum for $p = 1.0$ and 1.5 are plotted in the other panels.

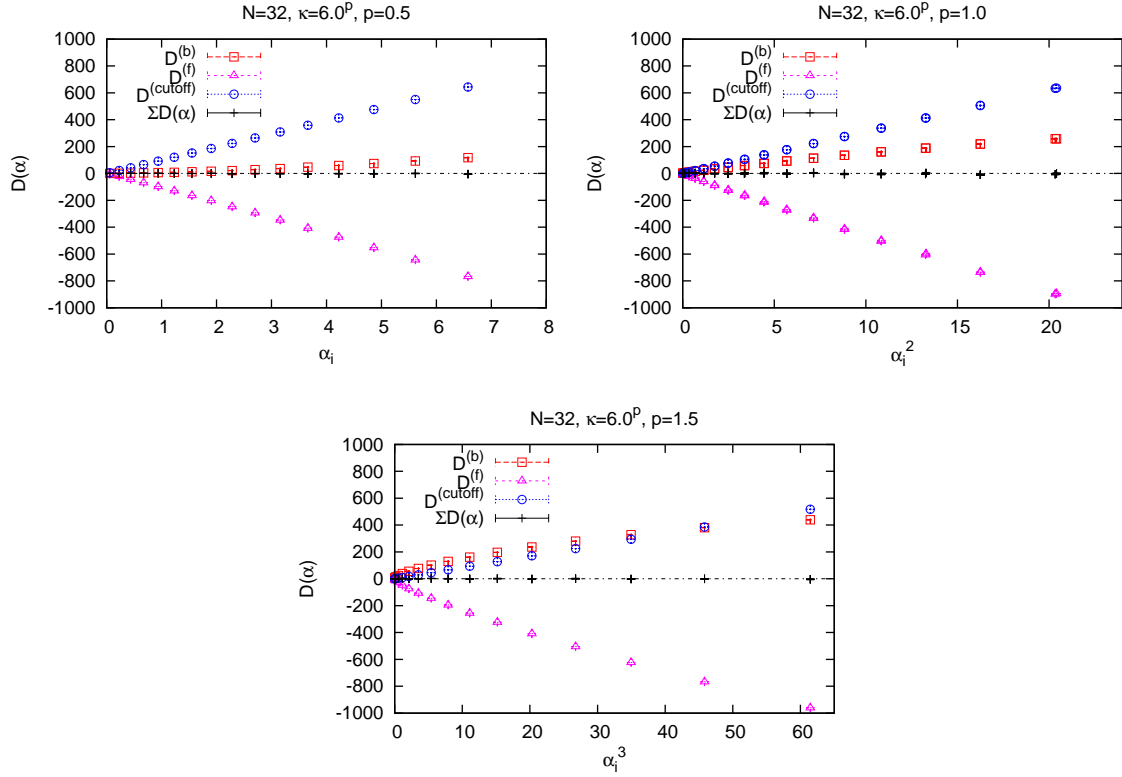


Figure 5.3: (Top-Left) $D^{(b)}(\alpha)$, $D^{(f)}(\alpha)$ and $D^{(\text{cutoff})}(\alpha)$ in the temporal S-D eq. (5.20) are plotted against $\alpha_k \geq 0$ for $p = 0.5$ with $N = 32$ and $\kappa = 6^p$, in which the right edge of α_k is the boundary in the temporal direction and $\alpha_k \sim 0$ corresponds to the bowels of the bulk. One can see that $D^{(\text{cutoff})}(\alpha)$ is proportional to α_k . The sum of $D^{(b)}(\alpha)$, $D^{(f)}(\alpha)$ and $D^{(\text{cutoff})}(\alpha)$ is also plotted, which becomes $1 - \frac{1}{N}$ for every α_k . Similarly, these terms for $p = 1.0$ and 1.5 are plotted against α_k^{2p} in the other panels, where $D^{(\text{cutoff})}(\alpha)$ are proportional to α_k^{2p} as well as $p = 0.5$.

N	κ	ε	Δ_t
64	4	0.28	4.19
96	8	0.27	4.96

Table 3: The explicit values of the lattice spacing ε and the volume Δ_t corresponding to N and κ for $p = 0.5$, which are used to make the plot in Fig. 5.5.

$p \geq 1.3$ has already disappeared for $N = 256$ and $\kappa = 16$. However, even for $p \leq 1.1$, it is still possible that the IR effects disappear in the infinite volume limit. We therefore investigate the behavior of the IR cutoff effects in this limit.

Before we show our results, we recall the definition of the lattice spacing and the volume in our model, which is explained for the bosonic model in the previous section. The lattice spacing $\delta t/R(t_c)$ is a time-dependent value, and it is defined for each time t as the interval between each adjacent points of $t/R(t_c)$. The volume Δ_t in the temporal direction is defined as the interval from t_c to the peak of $R(t)$ as in (4.8). Since the lattice spacing turns out to be almost constant, it is convenient to consider an averaged lattice spacing ε defined by

$$\varepsilon = \frac{\Delta_t}{\nu}, \quad (5.22)$$

where ν is the number of data points within Δ_t . The infinite volume limit corresponds to increasing the volume Δ_t with fixed ε , and the continuum limit corresponds to decreasing ε with fixed Δ_t . However, since these quantities are determined dynamically as a function of N and κ , it is difficult in practical to fix ε or Δ_t by adjusting N and κ . Therefore, we take the infinite volume limit in the following analysis by using the sets of N and κ having almost the same ε .

For $p \leq 1$ case

In Fig. 5.4, we first present the extent of space $R^2(t)/R^2(t_c)$ for $p = 0.5$ with $N = 64$ and 96, in which the lattice spacing ε have values close to each other. In order to see the behavior of the IR cutoff effects in the infinite volume limit, we focus on the effects after t_c and normalize α_k by $R(t_c)$. In Fig. 5.5 (left), we plot the cutoff term $D^{(\text{cutoff})}(\alpha)$ in the S-D eq. (5.20) against $\alpha'_k = (\alpha_k - t_c)/R(t_c)$ for $p = 0.5$ with N and κ chosen as in table 3. From this figure, we find that $D^{(\text{cutoff})}(\alpha)$ increases as the volume Δ_t becomes larger. Similarly, in Fig. 5.5 (right), we plot $C^{(\text{cutoff})}(\alpha)$ in the S-D eq. (5.19) against $\alpha'_k = (\alpha_k - t_c)/R(t_c)$ for $p = 0.5$ with the same N and κ , which shows that $C^{(\text{cutoff})}(\alpha)$ is independent of the volume. These results indicate that the IR cutoff effects for $p = 0.5$ does not disappear in the infinite volume limit.

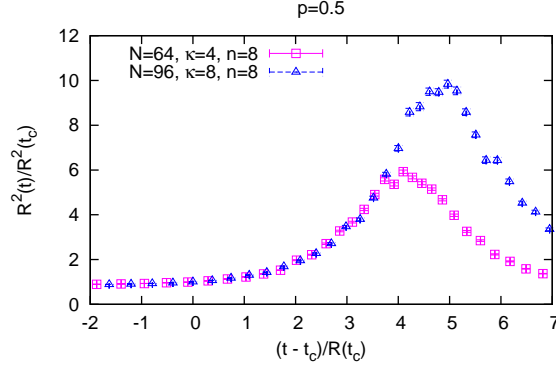


Figure 5.4: The extent of the space $R^2(t)$ normalized by $R^2(t_c)$ are plotted against $x = (t - t_c)/R(t_c)$ for $p = 0.5$, in which their lattice spacing have the close value whereas the volume increases, where the values of N , κ , ε and Δ_t are listed in table 3.

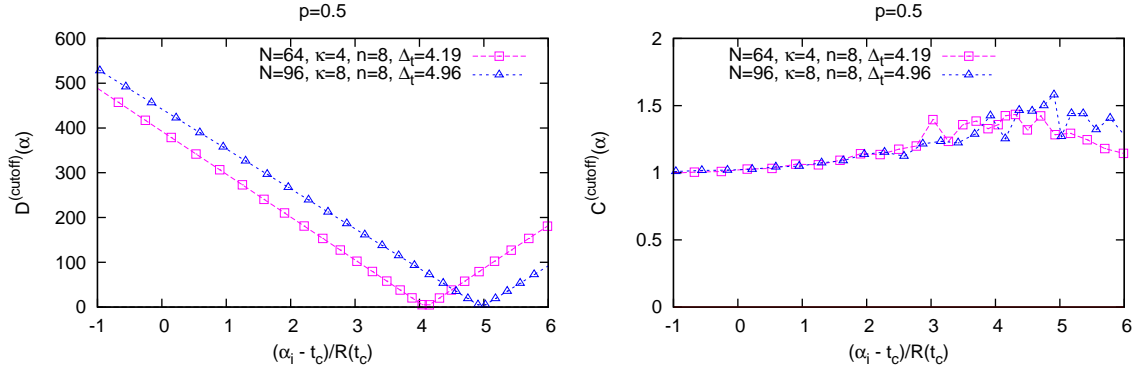


Figure 5.5: (Left) The cutoff term $D^{(\text{cutoff})}(\alpha)$ in the temporal S-D eq. (5.20) is plotted against $\alpha'_k = (\alpha_k - t_c)/R(t_c)$ for $p = 0.5$, in which the volume Δ_t takes various values while the lattice spacing is fixed to be $\varepsilon \sim 0.28$. These values and corresponding N , κ are listed in table 3. (Right) The cutoff term $C^{(\text{cutoff})}(\alpha)$ in the spatial S-D eq. (5.19) is plotted against $\alpha'_k = (\alpha_k - t_c)/R(t_c)$ for $p = 0.5$ with the same parameters for the left figure.

N	κ	ε	Δ_t	N	κ	ε	Δ_t
96	4	0.20	1.85	64	6	0.38	2.28
128	8	0.23	2.37	96	10	0.35	2.48
256	16	0.22	2.44				

Table 4: The values of matrix size N , the cutoff parameter κ , the lattice spacing ε and the volume Δ_t are listed for $p = 1.0$, which are used to make the plot in Fig. 5.6 and 5.7.

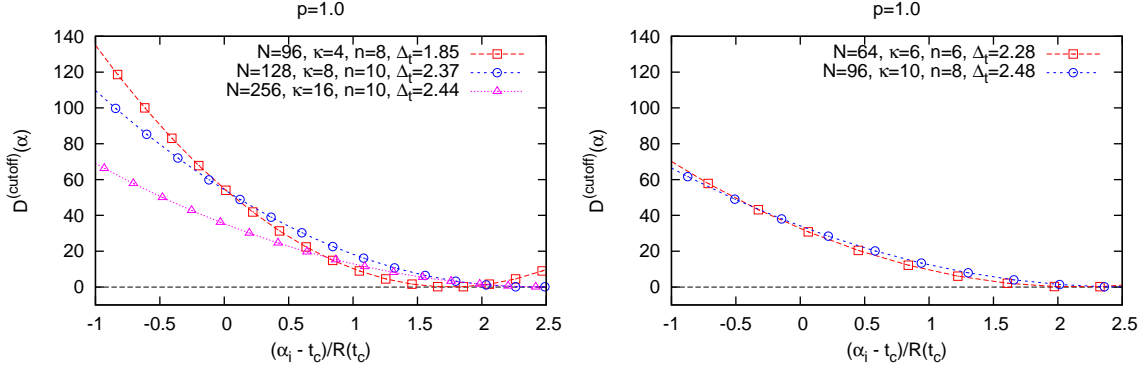


Figure 5.6: (Left) The cutoff term $D^{(\text{cutoff})}(\alpha)$ in the temporal S-D eq. (5.20) is plotted against $\alpha'_k = (\alpha_k - t_c)/R(t_c)$ for $p = 1.0$, in which the volume Δ_t takes various values while the lattice spacing is fixed to be $\varepsilon \sim 0.22$. These values and corresponding N , κ are listed in the left side of table 4. (Right) Similarly, $D^{(\text{cutoff})}(\alpha)$ is plotted for $p = 1.0$ with $\varepsilon \sim 0.35$. The parameters in detail are as in the right side of table 4.

Similarly, in Fig. 5.6 (left), we plot the cutoff term $D^{(\text{cutoff})}(\alpha)$ against $\alpha'_k = (\alpha_k - t_c)/R(t_c)$ for $p = 1.0$. We also plot the result for different lattice spacing in Fig. 5.6 (right). The values of N , κ , ε and Δ_t are listed in table 4. From these figures, we find that $D^{(\text{cutoff})}(\alpha)$ after t_c is independent of the volume. In Fig. 5.7, we plot the cutoff term $C^{(\text{cutoff})}(\alpha)$ against $\alpha'_k = (\alpha_k - t_c)/R(t_c)$ for $p = 1.0$ with the same parameters, and it turns out that $C^{(\text{cutoff})}(\alpha)$ decreases as one increases the volume. These results imply that the cutoff effect in the temporal direction remains in the infinite volume limit for $p = 1$ although the cutoff effect in the spatial directions disappears in this limit. Thus, we have found that the cutoff effects remain in the infinite volume limit for $p \leq 1$, which means that $R(t)$ and $T_{ij}(t)$ would depend on the IR cutoffs even for sufficiently large volume.

For $p > 1$ case

For $p = 1.5$, we plot $D^{(\text{cutoff})}(\alpha)$ against $\alpha'_k = (\alpha_k - t_c)/R(t_c)$ for $N = 64, 96$ and 128 in Fig 5.8 (left), in which the lattice spacing takes values close to each other and the volume

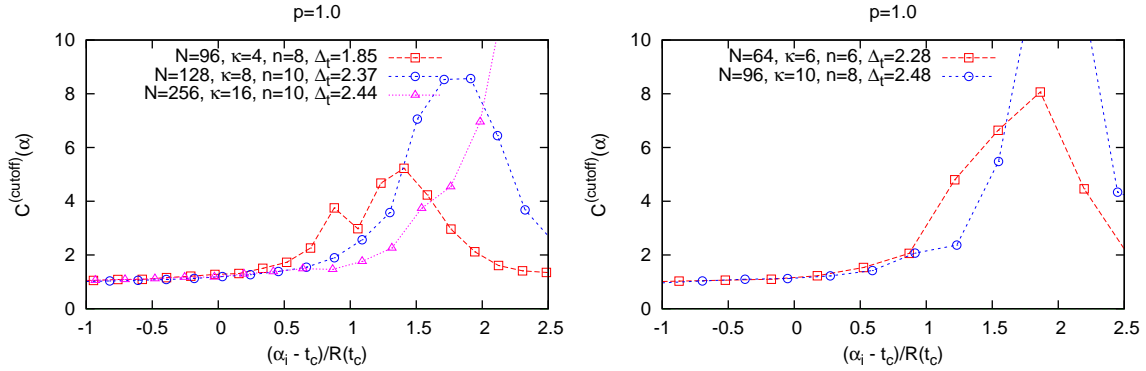


Figure 5.7: (Left) The cutoff term $C^{(\text{cutoff})}(\alpha)$ in the spatial S-D eq. (5.19) is plotted against $\alpha'_k = (\alpha_k - t_c)/R(t_c)$ for $p = 1.0$, in which the volume Δ_t takes various values while the lattice spacing is fixed to be $\varepsilon \sim 0.22$. These values and corresponding N, κ are listed in table 3. (Right) Similarly, $C^{(\text{cutoff})}(\alpha)$ is plotted for $p = 1.0$ with $\varepsilon \sim 0.35$. The parameters in detail are as in the right side of table 4.

N	κ	ε	Δ_t
64	4	0.312	1.12
96	6	0.294	1.18
128	8	0.298	1.49

Table 5: The values of matrix size N , the cutoff parameter κ , the lattice spacing ε and the volume Δ_t are listed for $p = 1.5$, which are used to make the plot in Fig. 5.8.

takes various values as in table 5. From this figure, $D^{(\text{cutoff})}(\alpha)$ turns out to be nearly zero after t_c . Moreover, it seems to decrease as one increases Δ_t . In Fig. 5.8 (Right), we also plot $C^{(\text{cutoff})}(\alpha)$ against $\alpha'_k = (\alpha_k - t_c)/R(t_c)$ for $p = 1.5$ with the same parameters. This figure shows that $C^{(\text{cutoff})}(\alpha)$ also decreases as the volume is increased. Therefore, we may conclude that the IR cutoff effects in both the temporal and spatial direction disappear in the infinite volume limit for $p = 1.5$.

Taking these results into account, we can interpret the IR cutoff dependence of $R(t)$ shown in Fig. 5.1. The observation that the behavior of $D^{(\text{cutoff})}(\alpha)$ changes at $p = 1$ indicates that the IR cutoff effects disappear in the infinite volume limit if one choose $p > 1$. This is also suggested from the observation that $R(t)$ almost coincides for $p = 1.3$ and 1.5 . Therefore, in order to obtain results which are independent of the IR cutoffs, we may use $1 < p \leq 1.5$ with sufficiently large volume.

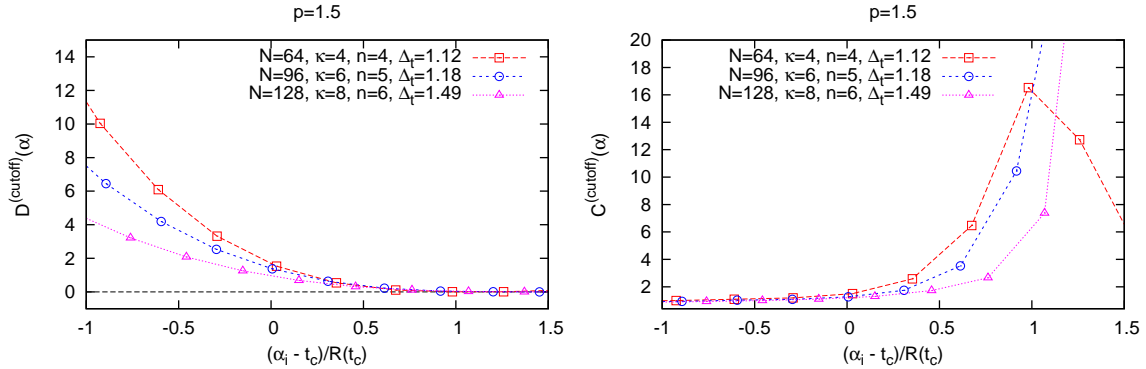


Figure 5.8: (Left) The cutoff term $D^{(\text{cutoff})}(\alpha)$ in the temporal S-D eq. (5.20) is plotted against $\alpha'_k = (\alpha_k - t_c)/R(t_c)$ for $p = 1.5$, in which the volume Δ_t takes various values while the lattice spacing is fixed to be $\varepsilon \sim 0.30$. These values and corresponding N , κ are listed in table 5. (Right) The cutoff term $C^{(\text{cutoff})}(\alpha)$ in the spatial S-D eq. (5.19) is plotted against $\alpha'_k = (\alpha_k - t_c)/R(t_c)$ for $p = 1.5$ with the same parameters for the left figure.

Short summary

We have studied the Lorentzian type IIB matrix model to investigate the time-evolution of the 10d space-time. In section 4, in order to investigate further time-evolution, we have considered the two simplified models which describe the expanding behavior at the early times and the late times qualitatively.

The simplified model for the early times is obtained by approximating the Pfaffian as $\text{Pf } \mathcal{M}(A) \sim \Delta^2(\alpha)$ where we omit the term proportional to A_i in the fermion action. In this model, it turned out that $R(t)$ expands exponentially as well as the original model. Moreover, we expect that this expansion continues for a long time. This result implies that the term proportional to A_0 is important for the emergent space to expand exponentially.

The simplified model for the late times is obtained by replacing the Pfaffian by $\text{Pf } \mathcal{M}(A) = 1$, which corresponds to quench all fermions. Due to the absence of fermions, there is an attractive force between the eigenvalues of A_0 . This fact makes the extent of their distribution finite without any temporal cutoffs. We have found that the behavior of the model drastically changes at the critical matrix size $N_c = 112$. For $N < N_c$, the extent in the temporal direction is independent of N , and one cannot extract a significant time-evolution. However, for $N \geq N_c$, the extent comes to grow linearly with N , and one can extract a significant time-evolution. It also turned out that the $\text{SO}(9)$ symmetry is spontaneously broken down to $\text{SO}(3)$ only for $N \geq N_c$. We observed that $R(t)$ deviates from the exponential expansion at the late times where $R(t)$ is proportional to $t^{1/2}$. The growth of $R(t) \propto t^{1/2}$ at the late times

is reminiscent of the behavior of the Friedmann-Robertson-Walker universe in the radiation dominated era.

We found that the expanding behavior of $R(t)$ in the long time-evolution is different between the simplified model for the early times and the late times although the difference between the action of these two models is only the power of the van der Monde determinant. We discuss the relation between these differences in Appendix C.

Although the Lorentzian type IIB matrix model exhibits interesting properties such as the spontaneous symmetry breaking of $SO(9)$, one needs to introduce the IR cutoffs in the model. In our models, it is not obvious whether the cutoff effects disappear in the infinite volume limit. In section 5, we therefore studied the IR cutoff dependence of the behavior of $R(t)$. In order to do this, we generalized the form of the IR cutoffs by introducing the parameter p and discuss the p dependence of $R(t)$, where $p = 1$ corresponds to the IR cutoffs used so far. For the simplified model for the early times, we have found that $R(t)$ depends on p although the qualitative behavior is the same as for $p = 1$. Interestingly, it has turned out that the $R(t)$ for $p = 1.3$ and 1.5 are close to each other except at large t , whereas the results for $p \leq 1.1$ are different from the ones for $p \geq 1.3$. These results suggest that the IR cutoff effects almost disappear for $p = 1.3$ and 1.5 for $N = 256$ and $\kappa = 16$.

In order to understand the above observations, we have also studied the IR cutoff effects more directly using the Schwinger-Dyson equations. From this analysis, we have found that the terms $C^{(\text{cutoff})}(\alpha)$ and $D^{(\text{cutoff})}(\alpha)$ arising from the IR cutoffs in the S-D eq. become small in the bulk of the emergent space-time as p is increased. This result is consistent with the result that $R(t)$ for $p \leq 1.1$ are different from the ones for $p \geq 1.3$ with $N = 256$ and $\kappa = 16$. However, it is possible that the IR cutoff effects for $p < 1.1$ disappear in the infinite volume limit. Therefore, by studying the behavior of the IR cutoff effects in the infinite volume limit, we have found that the temporal cutoff effect $D^{(\text{cutoff})}(\alpha)$ remains in this limit for $p \leq 1.0$. Similarly, it turned out that $C^{(\text{cutoff})}(\alpha)$ decreases in the infinite volume limit at least for $p > 1.0$.

These results indicate that $p = 1$ is a critical value for which the IR cutoff effects become independent of the volume. Therefore, we expect that the IR cutoff effects disappear in the infinite volume limit for $p > 1.0$, which implies that $R(t)$ for $p = 1.1$ come to be close to the ones for $p \geq 1.3$ with sufficiently large volume.

6 The matrix model with $SO(4)$ rotational symmetry

The numerical difficulty for studying the Euclidean type IIB matrix model comes from the sign problem arising from the complex fermion determinant. In general, when an action S

is complex, it is difficult to evaluate the path integral using usual Monte Carlo analysis and the importance sampling does not work since the factor $\exp(-S)$ in the partition function cannot be regarded as the Boltzmann weight factor.

In this thesis, we try to overcome the sign problem using the complex Langevin method (CLM), which is the complex extension of the stochastic quantization with the Langevin equation. According to this method, the path integral along the real axis is extended to the integration over the whole complex space by complexifying dynamical variables. In recent studies, the complex Langevin approach turned out to be successful in finite density QCD at least at high temperature or with heavy quarks as well as in the Random matrix theory at zero-temperature. Certain criteria to justify the method were suggested and the so-called “gauge cooling” procedure plays a very important role in improving the method in these studies.

The recent development on the complex Langevin method mentioned above motivates us to study the Euclidean type IIB matrix model by this method. In this model, the Pfaffian obtained by integrating out the fermions becomes complex. The Euclidean model has the $SO(10)$ symmetry and its spontaneous breaking has been studied by the factorization method and the Gaussian expansion method. According to these studies, it is suggested that the $SO(10)$ symmetry is broken down to $SO(3)$ rather than $SO(4)$. However, these results are obtained by assuming the pattern of the SSB. Therefore, it is important to confirm this result from another approach.

In this section, we consider a simplified model of the Euclidean type IIB matrix model in order to establish how to apply the complex Langevin method to the model. The simplified model consists of the Gaussian type of action for the bosonic part and the fermion determinant, which has the rotational $SO(4)$ symmetry. In this model, it is not broken when the fermions are absent. However, it is suggested that the symmetry is spontaneously broken down to $SO(2)$ in presence of the fermions [60, 61]. Therefore, the purpose in this section is to confirm that this SSB actually occurs using the complex Langevin method.

6.1 The definition of the toy model of the Euclidean type IIB matrix model

The partition function of the simplified model of the Euclidean type IIB matrix model is defined by

$$Z = \int dX d\bar{\psi} d\psi e^{-(S_b + S_f)}, \quad (6.1)$$

where the action is given by

$$S_b = \frac{1}{2}N \sum_{i=1}^4 \text{tr} (X_i^2), \quad (6.2)$$

$$S_f = -N \sum_{i=1}^4 \bar{\psi}_\alpha^f (\Gamma_i)_{\alpha\beta} X_i \psi_\beta^f. \quad (6.3)$$

X_i ($i = 1, \dots, 4$) are $N \times N$ Hermitian matrices and ψ_α^f and $\bar{\psi}_\beta^f$ ($\alpha, \beta = 1, 2$, $f = 1, \dots, N_f$) are Weyl fermions with N_f flavors. Γ^i are the 2×2 gamma matrices after the Weyl projection, which are defined by

$$\Gamma^i = \begin{cases} i\sigma_i & \text{for } i = 1 \sim 3, \\ \mathbf{1}_{2 \times 2} & \text{for } i = 4, \end{cases}$$

where σ_i are Pauli matrices. The model has the rotational $\text{SO}(4)$ symmetry under which A_μ transforms as a vector, and ψ_α^f and $\bar{\psi}_\alpha^f$ transform as Weyl spinors. By integrating out the fermions, the fermion action (6.3) becomes the determinant of the Dirac operator defined as

$$D = \sum_{i=1}^4 \Gamma^i \otimes X_i. \quad (6.4)$$

Therefore, the partition function becomes

$$Z = \int dX (\det D)^{N_f} e^{-S_b}. \quad (6.5)$$

It is suggested that the rotational $\text{SO}(4)$ symmetry of the model is spontaneously broken down to $\text{SO}(2)$ in the presence of the fermions. Note that the fermion effect for fixed N_f is suppressed in the large N limit because we now deal with fundamental fermions⁸. Therefore we also have to take N_f to infinity with N in order for the fermion effect to remain in the large N limit. Then, we define a ratio

$$r \equiv \frac{N_f}{N}$$

and take $N \rightarrow \infty$ with fixed r , which is known as the Veneziano limit.

Since we are interested in the spontaneous symmetry breaking of the $\text{SO}(4)$, we explain

⁸The degree of freedom for fundamental fermions with N_f flavors is $\sim NN_f$ while d.o.f. of the boson field is $\sim N^2$.

how to observe the SSB in this model. We define “the moment of inertia tensor”

$$T_{ij} = \frac{1}{N} \text{tr}(X_i X_j) \quad (6.6)$$

as an order parameter of the SSB of $\text{SO}(4)$. It is a 4×4 real symmetric tensor, and its four eigenvalues represent the extent in each direction of the four-dimensional space. We denote the eigenvalues as λ_i ($i = 1, \dots, 4$) with specified order

$$\lambda_1 \geq \lambda_2 \geq \lambda_3 \geq \lambda_4. \quad (6.7)$$

If the $\text{SO}(4)$ symmetry remains in the large N limit, the expectation values of these eigenvalues become the same quantity

$$\langle \lambda_1 \rangle = \langle \lambda_2 \rangle = \langle \lambda_3 \rangle = \langle \lambda_4 \rangle. \quad (6.8)$$

On the other hand, If the symmetry is spontaneously broken down to $\text{SO}(2)$, they will become as

$$\langle \lambda_1 \rangle = \langle \lambda_2 \rangle > \langle \lambda_3 \rangle \geq \langle \lambda_4 \rangle. \quad (6.9)$$

Thus, $\langle \lambda_i \rangle$ can be used as the order parameter of the $\text{SO}(4)$ symmetry breaking. In this simplified model, we can calculate analytically the sum of these expectation values as

$$\sum_{i=1}^4 \langle \lambda_i \rangle = \sum_{i=1}^4 \left\langle \frac{1}{N} \text{tr} X_i^2 \right\rangle = 4 + 2r. \quad (6.10)$$

In the case that there are no fermions, namely the $r = 0$ case, the model indeed has the $\text{SO}(4)$ symmetry at non-perturbative level, while the symmetry will be spontaneously broken for the $r > 0$ case.

In order to see the spontaneous symmetry breaking with a finite N , we introduce an external mass term in the action, which explicitly breaks the $\text{SO}(4)$ symmetry. Then, we first take the large N limit with the finite mass term, and then by extrapolating this term to zero, we can identify whether the SSB occurs in the infinite volume limit. We therefore introduce the mass term defined as

$$\frac{\epsilon N}{2} m_{ij} \text{tr}(X_i X_j) \quad (6.11)$$

in the boson action (6.2), where m_{ij} ($i, j = 1, \dots, 4$) is a mass parameter which is a real symmetric matrix, and ϵ is infinitesimal parameter which is taken to zero later. One can diagonalize the mass matrix m_{ij} using the $\text{SO}(4)$ transformation. Let us denote its diagonal

elements by m_i . Then, the boson action becomes

$$S_{b+\epsilon} = \frac{N}{2} (1 + \epsilon m_i) \text{tr} (X_i^2). \quad (6.12)$$

When all m_i have the same values, the action still has the SO(4) symmetry because the extra mass term can be absorbed by rescaling the X_i . Therefore, we should choose m_i to be different each other in order to break explicitly the SO(4) symmetry. For example, we have chosen the mass parameter in this thesis as

$$m_i = (1, 2, 4, 8). \quad (6.13)$$

Since we fixed the gauge of the SO(4) symmetry to diagonalize the mass matrix m_{ij} , it is not appropriate to use the eigenvalues of (6.6) as the order parameter of the SSB of the SO(4). Corresponding to the mass term introduced in (6.12), we instead adopt the order parameter such as

$$\begin{aligned} \langle \lambda_1 \rangle_\epsilon &= \frac{1}{N} \text{tr} X_1 X_1, & \langle \lambda_2 \rangle_\epsilon &= \frac{1}{N} \text{tr} X_2 X_2, \\ \langle \lambda_3 \rangle_\epsilon &= \frac{1}{N} \text{tr} X_3 X_3, & \langle \lambda_4 \rangle_\epsilon &= \frac{1}{N} \text{tr} X_4 X_4. \end{aligned}$$

For a finite ϵ , these expectation values will obviously differ from each other due to the extra mass term. For the mass parameter (6.13), their order is given as

$$\langle \lambda_1 \rangle_\epsilon > \langle \lambda_2 \rangle_\epsilon > \langle \lambda_3 \rangle_\epsilon > \langle \lambda_4 \rangle_\epsilon. \quad (6.14)$$

After extrapolating the mass term to zero, we can observe the pattern of symmetry breaking according to the discussion in this section.

However, the complex fermion determinant makes the evaluation of the partition function difficult. Since the factor e^{-S} can not be regarded as the Boltzmann weight and the importance sampling with Monte Carlo method will fail. As an proposal to overcome the sign problem, one can consider the factorization method for which one measures the expectation value of observables with the phase quenched action and then one re-weights them by the expectation value of the phase factor. This method works well at least in the case that the fluctuation of the phase factor is mild. However, when the phase oscillates acutely, the re-weighting with the phase factor becomes very sensitive and it is hard to estimate the correct expectation values. The study using the factorization method for this model has been performed in ref. [61]. On the other hand, one can consider the Gaussian expansion method which has been applied to this model in ref. [60]. Although this method uses a cer-

tain approximation, it turned out that the result obtained by the Gaussian expansion method agrees with the one obtained by the factorization method. According to these methods, the expectation values of λ_i for the $r = 1$ case become

$$\begin{aligned} \langle \lambda_1 \rangle &= \langle \lambda_2 \rangle \sim 2.1, \\ \langle \lambda_3 \rangle &\sim 1.0, \quad \langle \lambda_4 \rangle \sim 0.8. \end{aligned} \tag{6.15}$$

In this thesis, we study this matrix model using the complex Langevin method. This method is based on the stochastic quantization using the complex Langevin equation which is a complex extension of the Langevin equation. One can calculate the partition function without any approximations as long as one satisfies certain conditions to justify the method. In the next section, we review the complex Langevin method and its recent developments.

6.2 Brief review of the complex Langevin approach

In this subsection, we briefly introduce the stochastic quantization using the Langevin equation. In the next subsection we explain the complex extension of the Langevin method. The justification of the stochastic quantization is reviewed in Appendix D.

For a given action S , the Langevin equation is given as

$$\frac{d}{dt} x^{(\eta)}(t) = -\frac{\partial S}{\partial x} + \eta(t), \tag{6.16}$$

where $\eta(t)$ is the probabilistic variable generated with the Gaussian distribution

$$\exp \left[-\frac{1}{4} \int dt [\eta^2(t)] \right]$$

and t is a fictitious time introduced in the stochastic process. We denote the dynamical variable given in the stochastic process by $x^{(\eta)}(t)$. The probability distribution function so that $x^{(\eta)}(t) = x$ at time t for a provided initial configuration $x^{(\eta)}(t_0) = x_0$ is defined as

$$P(x; t) = \left\langle \delta \left(x - x^{(\eta)}(t) \right) \right\rangle_{\eta}, \tag{6.17}$$

where the expectation value $\langle \cdots \rangle_{\eta}$ is defined by

$$\langle \mathcal{O} \rangle_{\eta} \equiv \frac{\int D\eta \mathcal{O} e^{-\frac{1}{4} \int dt \eta^2(t)}}{\int D\eta e^{-\frac{1}{4} \int dt \eta^2(t)}}.$$

With this definition, the expectation value of the correlation function for the probabilistic

variable is given as

$$\langle \eta(t) \eta(t') \rangle_\eta = 2\delta(t - t').$$

The probability distribution function of $x^{(\eta)}(t)$ as the solution of the Langevin equation satisfies the Focker-Planck equation

$$\frac{\partial}{\partial t} P(x; t) = \frac{\partial}{\partial x} \left(\frac{\partial S}{\partial x} + \frac{\partial}{\partial x} \right) P(x; t).$$

One can show that $P(x; t)$ satisfying the FP eq. converges to a time-independent function for $t \rightarrow \infty$. More precisely, $P(x; t)$ behaves as

$$\lim_{t \rightarrow \infty} P(x; t) = P_{\text{eq}}(x) = e^{-S}$$

up to the normalization. Thus, the expectation values of observables can be calculated as

$$\begin{aligned} \lim_{t \rightarrow \infty} \langle O(x^{(\eta)}(t)) \rangle_\eta &= \lim_{t \rightarrow \infty} \int dx O(x) P(x; t) \\ &= \int dx O(x) P_{\text{eq}}(x) \\ &= \frac{\int dx O(x) e^{-S}}{\int dx e^{-S}} \\ &= \langle O(x) \rangle, \end{aligned}$$

which exactly coincides with that defined by the path integral formalism.

6.3 The application to the complex action case

When a given action is complex, the right-hand side of the Langevin equation (6.16) also becomes complex, which means that the dynamical variable x becomes complex even if one starts with a real configuration x . Therefore we need to complexify $x \mapsto z = x + iy$ and consider the complex extension of the Langevin equation

$$\frac{d}{dt} z^{(\eta)}(t) = -\partial_z S(z) + \eta(t),$$

where the action $S(z)$ is considered as a holomorphic function of a complex variable z by the analytic continuation. The probabilistic variable $\eta(t)$ may also be complex

$$\eta(t) = \eta_R(t) + i\eta_I(t)$$

which is generated with the probability distribution

$$\exp \left[-\frac{1}{4} \int dt \left[\frac{1}{N_R} \eta_R^2(t) + \frac{1}{N_I} \eta_I^2(t) \right] \right].$$

The probability distribution function of $z(t)$ following the complex Langevin equation (6.16) is defined as

$$P(x, y; t) = \left\langle \delta \left(x - x^{(\eta)}(t) \right) \delta \left(y - y^{(\eta)}(t) \right) \right\rangle_{\eta}, \quad (6.18)$$

where the expectation value $\langle \dots \rangle_{\eta}$ is defined by

$$\langle \mathcal{O} \rangle_{\eta} \equiv \frac{\int D\eta \mathcal{O} e^{-\frac{1}{4} \int dt \left[\frac{1}{N_R} \eta_R^2(t) + \frac{1}{N_I} \eta_I^2(t) \right]}}{\int D\eta e^{-\frac{1}{4} \int dt \left[\frac{1}{N_R} \eta_R^2(t) + \frac{1}{N_I} \eta_I^2(t) \right]}}.$$

We can also calculate the auto-correlation of $\eta(t)$ as

$$\begin{aligned} \langle \eta_R(t) \eta_R(t') \rangle_{\eta} &= 2N_R \delta(t - t'), \\ \langle \eta_I(t) \eta_I(t') \rangle_{\eta} &= 2N_I \delta(t - t'), \\ \langle \eta_R(t) \eta_I(t') \rangle_{\eta} &= 0. \end{aligned}$$

As we will see later, it is convenient to assume that

$$N_R - N_I = 1. \quad (6.19)$$

One can show that the probability distribution defined in (6.18) satisfies the Focker-Planck like equation

$$\partial_t P(x, y; t) = \partial_x (N_R \partial_x + \text{Re}[\partial_z S]) P(x, y; t) + \partial_y (N_I \partial_y + \text{Im}[\partial_z S]) P(x, y; t). \quad (6.20)$$

For a holomorphic observable $O(x + iy)$ defined as an analytic continuation of $O(x)$, one can show under certain conditions that there exists a complex valued probability distribution $\rho(x; t)$ that satisfies the relation

$$\int dx \rho(x; t) O(x) = \int dx dy P(x, y; t) O(x + iy) \quad (6.21)$$

and the equation

$$\frac{\partial \rho}{\partial t} = \frac{\partial}{\partial x} \left(\frac{\partial S}{\partial x} + \frac{\partial}{\partial x} \right) \rho. \quad (6.22)$$

The second relation is the Focker-Planck equation. Therefore, if the probability distribution $P(x, y; t)$ as the solution of the FP equation (6.20) converges to a finite function uniquely, the relation (6.21) implies that one can calculate the expectation value of observables $O(x)$ using the real probability distribution $P(x, y; t)$ and the holomorphic observable $O(x + iy)$ given by the CLM as

$$\begin{aligned}
\langle O \rangle &= \int dx O(x) \rho_{\text{equilibrium}}(x) \\
&= \lim_{t \rightarrow \infty} \int dx O(x) \rho(x; t) \\
&= \lim_{t \rightarrow \infty} \int dx dy O(x + iy) P(x, y; t) \\
&= \lim_{t \rightarrow \infty} \langle O(x + iy) \rangle_{\eta}.
\end{aligned}$$

In the rest of this subsection, we review the derivation of the relation (6.21).

In order to verify the relation (6.21), we first assume at $t = 0$ that

$$P(x, y; 0) = \rho(x; 0) \delta(y), \quad (6.23)$$

which satisfies the relation (6.21) trivially. In order to prove this relation for arbitrary $t > 0$, we show that each side of the relation can be rewritten as

$$\int dx dy O(x + iy) P(x, y; t) = \int dx dy O(x + iy; t) P(x, y; 0), \quad (6.24)$$

$$\int dx O(x) \rho(x; t) = \int dx O(x; t) \rho(x; 0). \quad (6.25)$$

We can immediately prove the relation (6.21) using (6.23), (6.24) and (6.25).

In the equation (6.24), we have introduced the time-dependent observables $O(z; t)$ defined as the solution of the differential equation

$$\frac{\partial}{\partial t} O(z; t) = \tilde{L} O(z; t), \quad (6.26)$$

where the operator \tilde{L} is defined by

$$\tilde{L} = \left(\frac{\partial}{\partial z} - \frac{\partial S}{\partial z} \right) \frac{\partial}{\partial z}. \quad (6.27)$$

In order to show (6.24), we consider the function

$$F(t, \tau) = \int dx dy O(x + iy; \tau) P(x, y; t - \tau)$$

interpolating each side of the equation (6.24) with $0 \leq \tau \leq t$. If this function is independent of τ , we obtain the equation (6.24). Therefore, let us consider the derivative of $F(t, \tau)$ with respect to τ , which gives

$$\begin{aligned} \frac{\partial}{\partial \tau} F(t, \tau) &= \int dx dy \frac{\partial}{\partial \tau} O(x + iy; \tau) P(x, y; t - \tau) + \int dx dy O(x + iy; \tau) \frac{\partial}{\partial \tau} P(x, y; t - \tau) \\ &= \int dx dy \tilde{L} O(x + iy; \tau) P(x, y; t - \tau) - \int dx dy O(x + iy; \tau) L^\top P(x, y; t - \tau), \end{aligned}$$

where we used (6.26). L^\top represents the operator acting on P , which is defined in the right hand side of the Focker-Planck like equation (6.20). As the result of partial integrations, we get

$$\frac{\partial}{\partial \tau} F(t, \tau) = \int dx dy \tilde{L} O(x + iy; \tau) P(x, y; t - \tau) - \int dx dy L O(x + iy; \tau) P(x, y; t - \tau), \quad (6.28)$$

where the operator L is given as

$$L = (N_R \partial_x - \text{Re}[\partial_z S]) \partial_x + (N_I \partial_y - \text{Im}[\partial_z S]) \partial_y \quad (6.29)$$

and we have assumed that the boundary terms vanish, which is actually correct when the integrand is a holomorphic function in the domain of integration and damps rapidly at the boundary.

It turns out that the terms on right hand side of (6.28) cancel to each other. In order to see this, let us act the operator L on a holomorphic function

$$f(z) = u(x, y) + iv(x, y).$$

Then, we get

$$\begin{aligned} Lf(z) &= (N_R \partial_x - \text{Re}[\partial_z S]) \partial_x f + (N_I \partial_y - \text{Im}[\partial_z S]) \partial_y f \\ &= (N_R \partial_z - \text{Re}[\partial_z S]) \partial_z f + (iN_I \partial_z - \text{Im}[\partial_z S]) (i\partial_z f) \\ &= [-\partial_z S + (N_R - N_I) \partial_z] \partial_z f \\ &= \tilde{L} f(z), \end{aligned} \quad (6.30)$$

where we have used the Cauchy-Riemann relation

$$\begin{aligned}\frac{\partial u}{\partial x} &= \frac{\partial v}{\partial y}, \\ \frac{\partial u}{\partial y} &= -\frac{\partial v}{\partial x}\end{aligned}$$

and $\partial_z = \frac{1}{2}(\partial_x - i\partial_y)$. In the last step, we have used (6.19). Therefore it is necessary for the observable to be holomorphic to satisfy the eq. (6.30). From (6.30), it turns out that the right hand side of (6.28) vanishes, which implies that $F(t, \tau)$ is independent of τ , and the relation (6.24) is satisfied for any t .

We can perform a similar argument to verify the eq. (6.25). Thus, we can show that the relation (6.21).

6.4 Application of the complex Langevin method to the matrix model

The complex Langevin equation for the model (6.1) is given by

$$\frac{dX_i}{dt} = -\frac{\partial S}{\partial X_i} + \eta(t),$$

where $\eta(t)$ is a white noise which is an $N \times N$ Hermitian matrix. The action S is given as

$$S = S_{b+\epsilon} - N_f \ln(\det D) \quad (6.31)$$

using the mass deformed bosonic action (6.12). The drift term in the complex Langevin equation is given as

$$\frac{\partial S}{\partial X_i} = N(1 + \epsilon m_i) X_i - N_f \text{tr}_\alpha (D^{-1} \Gamma^i), \quad (6.32)$$

where the symbol tr_α represents a trace over spinor indices. To derive (6.32) we used the equation

$$\frac{\delta \det D}{\delta X^i} = \frac{\delta \det D}{\delta D_{ab}} \frac{\delta D_{ab}}{\delta X^i} = \det D D_{ab, \alpha\beta}^{-1} \frac{\delta D_{ba, \beta\alpha}}{\delta X^i}.$$

Since the action and the drift term in (6.32) are complex, X_i are no longer Hermitian. Therefore, we need to complexify the X_i to complex matrices in $SL(N, \mathbb{C})$. By considering a norm such as

$$N_H = \frac{1}{dN} \sum_{i=1}^4 \text{tr} \left[\left(X_i - X_i^\dagger \right) \left(X_i - X_i^\dagger \right)^\dagger \right], \quad (6.33)$$

one can measure the degree of deviation from the Hermitian configuration space. It vanishes when all X_i are Hermitian, while for non-Hermitian matrices, it will not vanish. In order to

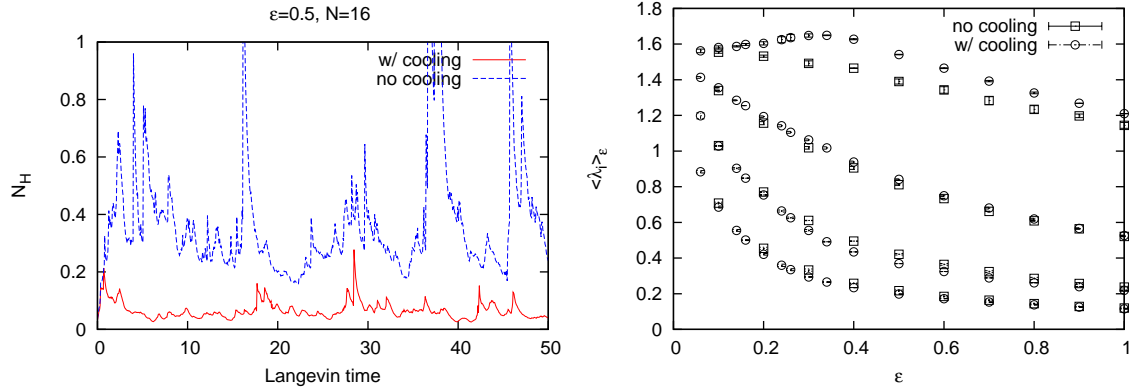


Figure 6.1: (Left) The hermiticity norm (6.33) for the $r = 1$ case are plotted against Langevin time for $\epsilon = 0.5$ and $m_i = (1, 2, 4, 8)$ with $N = 16$. The solid line is the norm obtained from the simulation with the gauge cooling and the broken line is the one obtained from the simulation without the gauge cooling. (Right) The expectation values of the order parameter $\langle \lambda_i \rangle_\epsilon$ are plotted against ϵ , in which the circle represents the result obtained from the simulation with the gauge cooling, and the square represents the result obtained from the simulation without the gauge cooling.

satisfy the criteria to justify the complex Langevin method, it is necessary to keep the norm (6.33) small as possible, which can be improved by the so-called “gauge cooling”. In our case, we consider the gauge transformation for the bosonic matrices X_i such as

$$X_i \rightarrow \Omega^{-1} X_i \Omega, \quad \Omega = e^{i\delta_a \omega_a} \in SL(N, \mathbb{C}),$$

where ω_a ($a = 1, \dots, N^2 - 1$) are the generators of the $SL(N, \mathbb{C})$ and δ_a are parameters of the gauge cooling. One should choose δ_a so that the norm (6.33) decreases by the transformation. We carry out this gauge transformation for each Langevin step to decrease the norm (6.33). The result of the gauge cooling is illustrated in Fig. 6.1 (Left), in which we plot the norm (6.33) against the Langevin time in the cases that the gauge cooling is applied or not. This figure shows that the gauge cooling successfully keeps the hermiticity norm small. In Fig. 6.1 (Right), we plot the expectation values $\langle \lambda_i \rangle_\epsilon$ against ϵ in the cases that the gauge cooling is applied or not. From this figure, we find that $\langle \lambda_i \rangle_\epsilon$ depends on the hermiticity norm and the gauge cooling actually improve the method.

While we found that the hermiticity can be improved by the gauge cooling, there is another issue to be taken into account in the CLM when the drift term in the complex Langevin equation has poles. In this case, one cannot justify the method if the poles are involved in the probability distribution of dynamical variables. In our case, the drift term (6.32) has a pole at the values of X_i for which the Dirac operator has zero-eigenvalues. Therefore, when

X_i given as the solution to the complex Langevin equation takes such values, the method will not work. In Fig. 6.2 (Left) and (Right), we plot the the eigenvalue distribution of the Dirac operator obtained by solving the complex Langevin equation for $r = 1$ with $N = 48$ and $\epsilon = 0.2, 0.6$, in which the Dirac operator comes to have zero-eigenvalues frequently for small ϵ . Therefore, we expect that the CLM does not work for such values of ϵ .

In this thesis, we propose a procedure to overcome this singular drift problem. In order that the probability distribution function of X_i avoids this pole, we modify the model by introducing a mass term to the fermions. As we will explain as follows, this modification corresponds to shift the pole of the Dirac operator. For instance, let us consider the 4-component vector fields x_i instead of the bosonic matrices X_i . Then the Dirac operator is given by

$$D = \Gamma^i \otimes x_i = \begin{pmatrix} x_4 + ix_3 & x_2 + ix_1 \\ -x_2 + ix_1 & x_4 - ix_3 \end{pmatrix},$$

from which the determinant of D becomes

$$\det D = \sum_i x_i^2.$$

Therefore, D^{-1} in the drift term has a pole at $|x_i| = 0$. Note that $\langle x_i \rangle = 0$ if the SO(4) symmetry remains. Hence, the CLM does not work for small ϵ . In order to make x_i to avoid the pole, we add extra fermion mass terms $-N \sum_{i=1}^4 \bar{\psi}_\alpha^f (\Gamma^i)_{\alpha\beta} \alpha_i \psi_\beta^f$ to the action. Then the mass deformed Dirac operator is given as

$$D_{(\alpha)} = \sum_{i=1}^4 \Gamma^i \otimes (x_i + \alpha_i),$$

where α_i ($i = 1, \dots, 4$) are real. Then, the drift term becomes

$$\frac{\partial S}{\partial x_i} = (1 + \epsilon m_i) x_i - N_f \text{tr}_\alpha \left(D_{(\alpha)}^{-1} \Gamma^i \right),$$

in which the pole of $D_{(\alpha)}^{-1}$ shifts to $x_i = -\alpha_i$. Therefore we expect that x_i obtained as the solution to the complex Langevin eq. avoids the pole of $D_{(\alpha)}^{-1}$ even for small ϵ as far as one uses sufficiently large $|\alpha_i|$. Note that these extra fermion masses can be absorbed by translating the bosonic fields in our model. In fact, if one translates $x_i \rightarrow x_i - \alpha_i$, the deformed Dirac operator $D_{(\alpha)}$ returns to D while the Gaussian potential $\frac{1}{2} x_i^2$ in the boson action becomes $\frac{1}{2} (x_i - \alpha_i)^2$. In this case, the probability distribution function $P(x_i)$ also avoid the pole of the drift term.

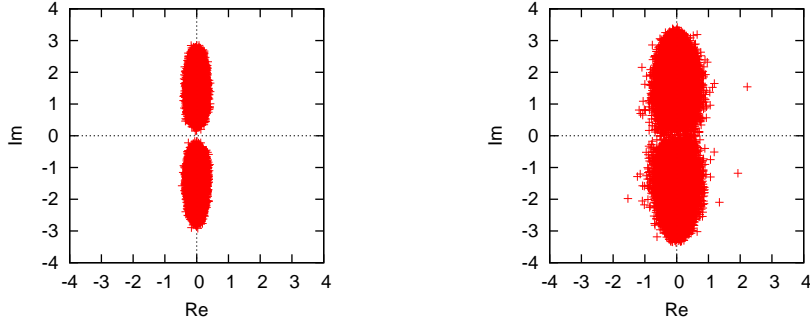


Figure 6.2: (Left) The scattered plot of the eigenvalues of the Dirac operator (6.4) with $\epsilon = 0.6$ and $N = 48$ in the $r = 1$ case. The origin is the pole of the drift term (6.32). (Right) The scattered plot of the eigenvalues of the Dirac operator with $\epsilon = 0.2$ and $N = 48$ in the $r = 1$ case.

Similarly, for boson matrices X_i , we can also shift the pole of the drift term by introducing the mass terms to fermions. The Dirac operator (6.4) is deformed as

$$D \rightarrow D_{(\alpha)} = \sum_{i=1}^4 \Gamma^i \otimes (X_i + \alpha_i \mathbf{1}_{N \times N}) \quad (6.34)$$

Note that the extra fermion mass terms explicitly break the $\text{SO}(4)$ symmetry at $\epsilon = 0$. Therefore, in order to remain the symmetry as possible, we introduce the fermion mass term to only one out of four directions. Taking into account the order of λ_i for finite ϵ (6.14), we should use the values of α_i as

$$\alpha_i = (0, 0, 0, m_f), \quad (6.35)$$

for which the $\text{SO}(3)$ symmetry remains in the model at $\epsilon = 0$. Therefore, we still can investigate the pattern of the spontaneous symmetry breaking of $\text{SO}(3)$. For the fermion mass parameter (6.35), since the deformed Dirac operator becomes

$$D_{(\alpha)} = \sum_{i=1}^3 \Gamma^i \otimes X_i + \mathbf{1}_{2 \times 2} \otimes (X_4 + m_f),$$

it is expected that the pole of the drift term shifts along the real direction. In Fig. 6.3, we plot the eigenvalue distribution of the mass deformed Dirac operator (6.34) with $m_f = 0.6$ for $\epsilon = 0.6$ and 0.2 , in which the pole of the drift term exists at the origin. This figure shows that the whole eigenvalue distribution actually shifts along the real direction. Moreover, it turns out that the distribution avoids the pole at the origin even for $\epsilon = 0.2$ in contrast to the $m_f = 0$ case. Therefore, we can extrapolate ϵ to zero using smaller values of ϵ for a finite

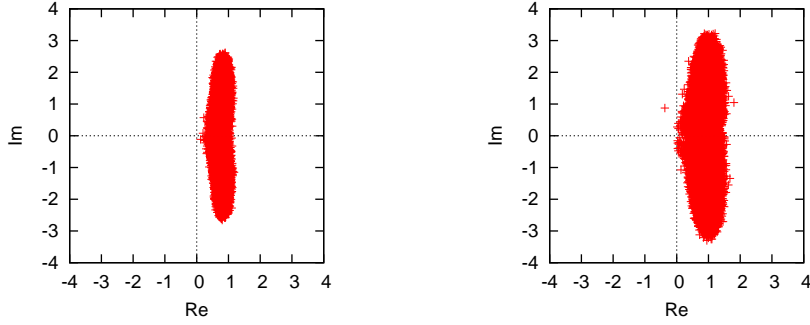


Figure 6.3: (Left) The scattered plot of the eigenvalues of the mass deformed Dirac operator (6.34) with $m_f = 0.6$ and $\epsilon = 0.6$ in the $r = 1$ case. The pole of the drift term is at the origin. (Right) The scattered plot of the eigenvalues of the mass deformed Dirac operator (6.34) with $m_f = 0.6$ and $\epsilon = 0.2$ in the $r = 1$ case.

m_f .

In order to evaluate how far the eigenvalues deviate from the pole, it is convenient to define the radial distribution function $\varphi(R)$ as

$$\varphi(R) = \frac{1}{2\pi R} \sum_i \int dX P(\chi^{(i)}, t = \infty) \delta(|\chi^{(i)}| - R), \quad (6.36)$$

where $\chi^{(i)}$ ($i = 1, \dots, 2N$) are eigenvalues of the mass deformed Dirac operator $D_{(\alpha)}$. The $\varphi(R)$ represents the eigenvalue distribution of $\chi^{(i)}$, which is a function of the radius R that is the distance from the pole. We plot $\varphi(R)$ against R for $m_f = 0$ in Fig. 6.4 (Left), in which we find that the eigenvalues indeed distribute around the pole for small ϵ . We also plot $\varphi(R)$ against R for the mass parameter (6.35) with $m_f = 0.6$ in Fig. 6.4 (Right). This figure shows that eigenvalues distribution damps rapidly around the pole even for small ϵ .

Thus, the fermion mass term moves the eigenvalues of the Dirac operator to the real direction, which improves the singular drift problem. On the other hand, we have also taken care of the hermiticity norm (6.33) by performing the gauge cooling. We expect that the complex Langevin method works in this model as far as both the singular drift and hermiticity are controllable by the above procedures.

We recall that the action also has the boson mass term which explicitly breaks the $SO(4)$ symmetry. Therefore we first take the large- N limit with fixed ϵ , and then we extrapolate ϵ to zero. We plot the expectation values of λ_i against $1/N$ for $\epsilon = 0.2$ and $m_f = 0.6$ in Fig. 6.5, in which we take the large N limit. Similarly, we can take the large- N limit of λ_i

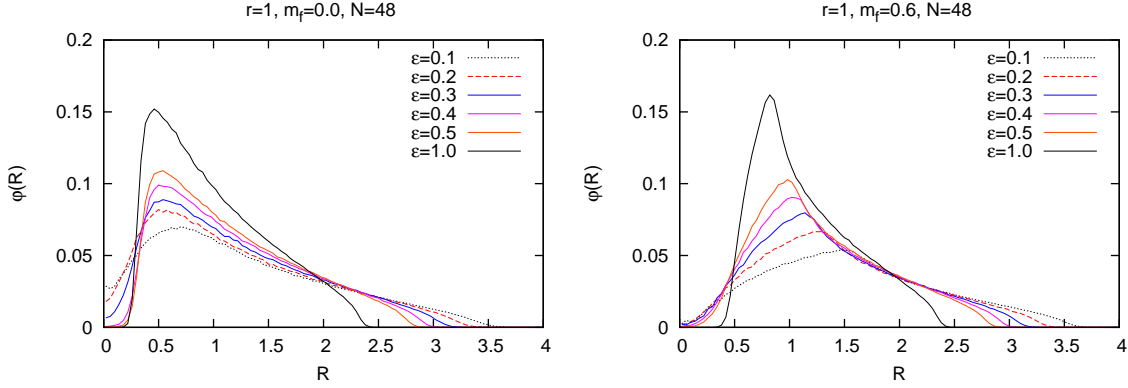


Figure 6.4: (Left) The radial eigenvalue distribution function $\varphi(R)$ for the Dirac operator is plotted against R for $m_f = 0$ in the $r = 1$ case. (Right) The eigenvalue distribution function $\varphi(R)$ for the mass deformed Dirac operator $D_{(\alpha)}$ is plotted against R for the mass parameter (6.35) for $m_f = 0.6$ in the $r = 1$ case.

for every ϵ . Let us consider the ratio defined as

$$\rho_{\epsilon, m_f}^{(i)} = \frac{\langle \lambda_i \rangle_{\epsilon, m_f}}{\sum_{i=1}^4 \langle \lambda_i \rangle_{\epsilon, m_f}}, \quad (6.37)$$

where $\langle \lambda_i \rangle_{\epsilon, m_f}$ is the expectation values after taking large- N limit for fixed ϵ and m_f . Then, we plot the expectation values (6.37) against ϵ for $m_f = 0.6$ in Fig. 6.6, in which we extrapolated ϵ to zero using only reliable data points of ϵ in terms of the radial distribution function. Let us denote the expectation value of λ_i obtained by extrapolating ϵ to zero with fixed m_f as

$$\begin{aligned} \langle \lambda_i \rangle_{m_f} &= \lim_{\epsilon \rightarrow 0} \langle \lambda_i \rangle_{\epsilon, m_f}, \\ \rho_{m_f}^{(i)} &= \lim_{\epsilon \rightarrow 0} \rho_{\epsilon, m_f}^{(i)}. \end{aligned}$$

As a result, we find that $\langle \lambda_1 \rangle_{m_f}$ and $\langle \lambda_2 \rangle_{m_f}$ are close to each other while the other $\langle \lambda_i \rangle_{m_f}$ are different from them. Since the action with the fermion mass (6.35) has $SO(3)$ symmetry at $\epsilon = 0$, this observation can be interpreted as the SSB from $SO(3)$ to $SO(2)$. Note that the exact values of $\langle \lambda_i \rangle_{m_f}$ depend on m_f , and those values are different from the ones for $m_f = 0$ as in (6.15). Therefore, in order to obtain the exact expectation values of λ_i for $m_f = 0$, we also have to extrapolate m_f to zero. We plot the expectation values $\rho_{\epsilon, m_f}^{(1)}$ against ϵ for various m_f in Fig. 6.7 (Top-Left). From this, we obtain $\rho_{m_f}^{(1)}$ for each m_f . Similarly, we can obtain $\rho_{m_f}^{(2)}$, $\rho_{m_f}^{(3)}$ and $\rho_{m_f}^{(4)}$ for each m_f from the other panels in Fig. 6.7.

We plot $\rho_{m_f}^{(i)}$ against m_f in Fig. 6.8, in which it turns out that the SSB from $SO(3)$ to

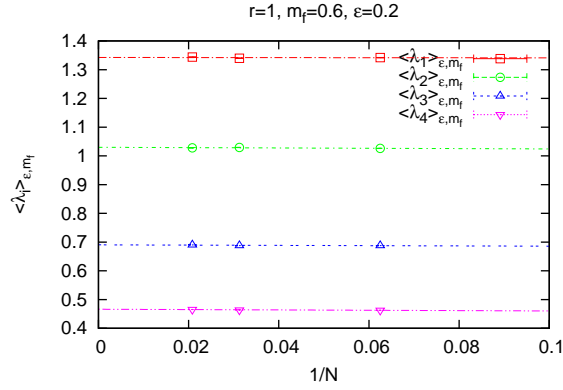


Figure 6.5: The expectation values of λ_i are plotted against $1/N$ for $\epsilon = 0.2$ and $m_f = 0.6$. The lines are fit of λ_i to a function $f(x) = ax + b$.

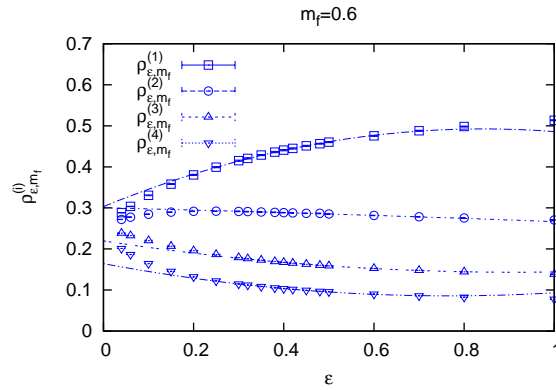


Figure 6.6: The expectation values $\rho_{\epsilon, m_f}^{(i)}$ are plotted against ϵ for $m_f = 0.6$. The broken lines are fits of the data for each λ_i to $f(\epsilon) = a\epsilon^2 + b\epsilon + c$. We obtained $\rho_{m_f}^{(1)} = 3.03(1) \times 10^{-1}$, $\rho_{m_f}^{(2)} = 3.00(1) \times 10^{-1}$, $\rho_{m_f}^{(3)} = 2.19(2) \times 10^{-1}$ and $\rho_{m_f}^{(4)} = 1.64(1) \times 10^{-1}$ by extrapolating ϵ to zero.

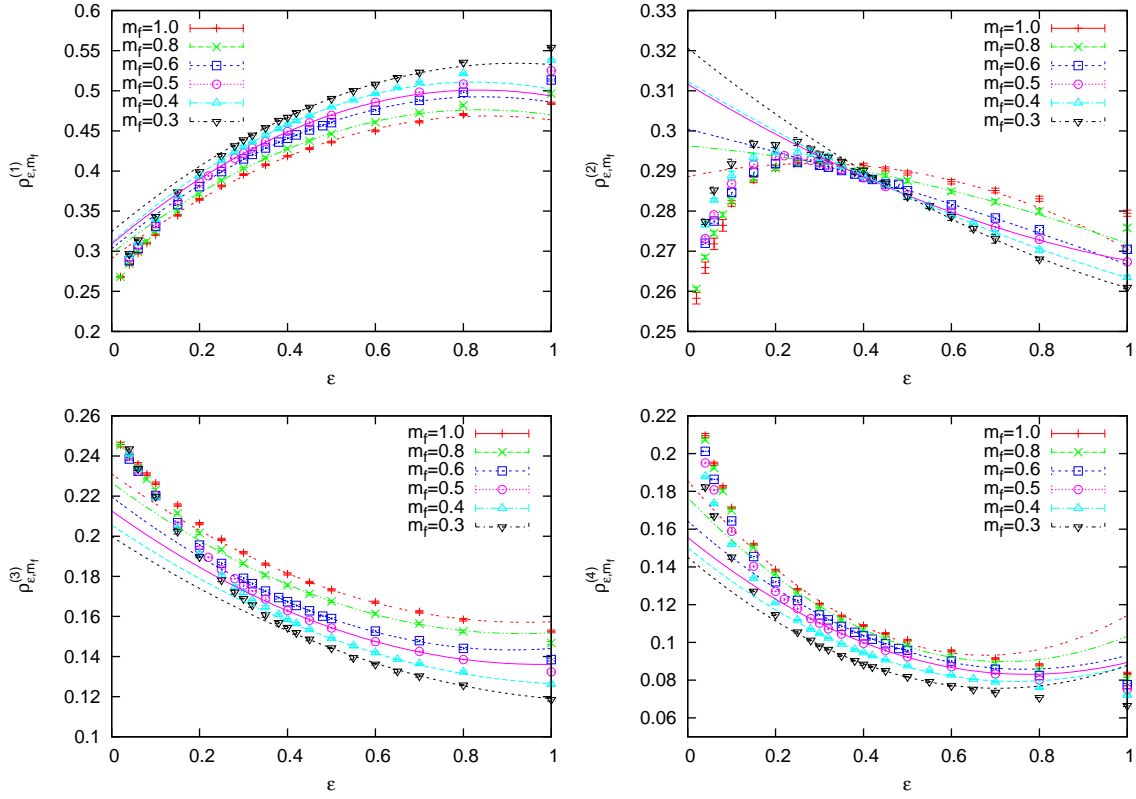


Figure 6.7: (Top-left) The expectation values of the order parameter $\langle \lambda_1 \rangle_\epsilon$ are plotted against ϵ for various values of m_f . The lines are fits of the data for each m_f to a function $f(\epsilon) = a\epsilon^2 + b\epsilon + c$. The results for the other $\langle \lambda_i \rangle_\epsilon$ are also plotted in the other panels.

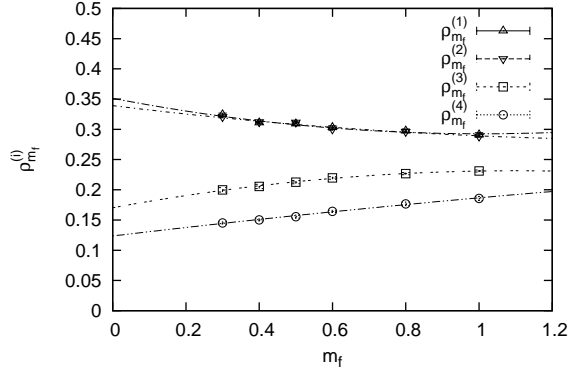


Figure 6.8: The expectation values $\rho_{m_f}^{(i)}$ obtained by extrapolating ϵ to zero are plotted against m_f . The lines are fits of the data to a function $f(m_f) = am_f^2 + bm_f + c$ for $0.4 \leq m_f \leq 1.0$. We obtained $\rho^{(1)} = 3.25(6) \times 10^{-1}$, $\rho^{(2)} = 3.3(1) \times 10^{-1}$, $\rho^{(3)} = 1.66(4) \times 10^{-1}$ and $\rho^{(4)} = 1.14(6) \times 10^{-1}$ by extrapolating m_f to zero.

SO(2) can be observed for every m_f . From this figure, we can extrapolate the fermion mass m_f to zero, which gives $\rho^{(1)} = 3.25(6) \times 10^{-1}$, $\rho^{(2)} = 3.3(1) \times 10^{-1}$, $\rho^{(3)} = 1.66(4) \times 10^{-1}$ and $\rho^{(4)} = 1.14(6) \times 10^{-1}$, where $\rho^{(i)}$ is defined by

$$\begin{aligned}
 \rho^{(i)} &= \lim_{m_f \rightarrow 0} \rho_{m_f}^{(i)} \\
 &= \lim_{m_f \rightarrow 0} \frac{\langle \lambda_i \rangle_{m_f}}{\sum_{i=1}^4 \langle \lambda_i \rangle_{m_f}} \\
 &= \frac{\langle \lambda_i \rangle}{4 + 2r}.
 \end{aligned} \tag{6.38}$$

Note that the rotational SO(4) symmetry of the model restores in the $m_f \rightarrow 0$ limit. Therefore, this indicates that the SO(4) symmetry is spontaneously broken down to SO(2). Moreover, we obtain $\langle \lambda_1 \rangle = 1.95(4)$, $\langle \lambda_2 \rangle = 1.99(8)$, $\langle \lambda_3 \rangle = 0.99(2)$ and $\langle \lambda_4 \rangle = 0.68(4)$ from the relation (6.38) and find that these values are agree with the ones obtained for the previous results (6.15). We should emphasize that we did not assume the pattern of the SSB of SO(4) in this analysis in contrast to the previous approaches.

In this section, we have considered only the boson mass term as in (6.13) and the fermion mass as in (6.35). We have also performed the same analysis with the fermion mass parameter $\alpha_i = (0, 0, m_f, 0)$, from which we find that the SSB from SO(4) to SO(2) is also observed. See appendix E in detail.

Short summary

In section 6, we have studied the matrix model as a toy model of the type IIB matrix model. The toy model is suffered from the sign problem due to the fermion determinant while it will induce the spontaneous breaking of the rotational symmetry of the model. In this thesis, in order to overcome the sign problem, we have used the complex Langevin method in which one complexifies dynamical variables and considers a holomorphic extension of an given action.

The toy model has the rotational $SO(4)$ symmetry which will be spontaneously broken down to $SO(2)$ in the presence of the fermions. In order to observe it for finite N , we have introduced the boson mass in the model. By extrapolating the extra mass to zero, we can investigate the pattern of the SSB. It is important to reduce the mass term close to zero as possible. Since the drift term in the complex Langevin equation involves the inversion of the Dirac operator, the drift term becomes singular when the Dirac operator has zero-eigenvalues. We have shown that the eigenvalues keep away from the pole for $\epsilon \geq 0.5$, nevertheless the Dirac operator comes to have eigenvalues around the pole frequently for $\epsilon \leq 0.3$. Therefore, we cannot make ϵ sufficiently small because the CLM does not work for such ϵ .

In order to overcome this singular drift problem, we have introduced the fermion mass term in the model. This mass term shifts the pole of the drift term, which enable the eigenvalues of the deformed Dirac operator to avoid the pole even for small ϵ . Although the mass deformation of the fermion action explicitly breaks the $SO(4)$ symmetry of the model to $SO(3)$ in the $\epsilon \rightarrow 0$ limit, we are still able to investigate the pattern of the spontaneous breaking of the $SO(3)$ symmetry. We found that the $SO(3)$ symmetry is spontaneously broken down to $SO(2)$ for several values of the fermion mass m_f .

Also, by evaluating the order parameter after extrapolating the fermion mass m_f , we are able to investigate the pattern of the spontaneous breaking of the full $SO(4)$ symmetry. As a result, we found that the $SO(4)$ symmetry breaks down to $SO(2)$ in the $m_f \rightarrow 0$ limit. Moreover, the exact values of the order parameters $\langle \lambda_i \rangle$ are consistent with the ones obtained for the previous studies [60, 61]. In particular, we have confirmed the SSB from $SO(4)$ to $SO(2)$ without any ansatz such that one assumes the pattern of the SSB as in the previous studies.

7 Summary and discussion

In this thesis we have studied the dynamics of the space-time using matrix models by numerical approach. In the first part, I have investigated the time evolution of the 10d space-time predicted by the superstring theory using the Lorentzian type IIB matrix model. we have also studied this subject using the toy model of the Euclidean version of type IIB matrix

model.

In the Lorentzian type IIB matrix model, it turned out that emergent 3d space expands exponentially for $N \leq 24$. Furthermore, in order to investigate the expanding behavior of the 3d space qualitatively, we defined the simplified model for early times and late times by approximating the fermion determinant. These two models are expected to capture the qualitative properties of the original model. The simplified model for early times indicates that the exponential expansion observed for the original model continues for a long time. On the other hand, the simplified model for late times has finite time extent without any temporal cutoffs since the supersymmetry does not exist. For $N < N_c$, the dominant matrix configurations do not allow extraction of a well-defined time-evolution. For $N \geq N_c$, on the other hand, we can extract a meaningful time-evolution, which shows that the $SO(9)$ rotational symmetry is broken spontaneously down to $SO(3)$ symmetry at some point in time similarly to the original model. With the matrix size $N \leq 512$, we observed that the exponential expanding behavior of 3d space continues for a while and it changes into a power-law expansion at late times. Interestingly, it turned out that the power-law expanding behavior observed in the simplified model is consistent with that of the Friedmann-Robertson-Walker universe in the radiation dominated era.

Furthermore, using the simplified model of the Lorentzian type IIB matrix model, we have confirmed that the effects of IR cutoff disappear in the infinite volume limit by modifying the form of the cutoffs. The expanding behavior becomes universal in some range of p . In the simplified model, we have concluded that $p = 1$ is the critical value below which the IR cutoff effects remain even in the infinite volume limit by evaluating them directly using the Schwinger-Dyson equation. Therefore, we need to choose $p > 1$ to obtain results which are independent of the IR cutoffs.

On the other hand, as a toy model of the Euclidean type IIB matrix model, we studied numerically the matrix model with spontaneous breaking of rotational $SO(4)$ symmetry, whose fermion determinant causes the sign problem. In order to overcome this problem, we used the complex Langevin approach in this thesis. In order to observe the SSB, we first introduced boson masses which break the $SO(4)$ symmetry and then extrapolates them to zero later. Moreover, in order to extend the region in which the method is applicable, we also introduced an extra mass term to the fermion action, which improves the singular-drift problem. As a result we were able to extrapolate the boson masses to smaller values. Thus, we found that the $SO(4)$ symmetry is actually spontaneously broken down to $SO(2)$. The expectation values obtained by the extrapolation is consistent with the one obtained by the Gaussian expansion method [60] and the factorization method [61]. We would like to emphasize here that we do not have to assume a concrete pattern of the SSB in advance in

contrast to the other method.

Future direction

Considering that the argument on the disappearance of the cutoff effects does not depend on the details of the model, we may naturally expect that the cutoff effects also disappear with sufficiently large p in the original model. However, the critical value of p beyond which the cutoff effects disappear in the infinite volume limit may depend on the model. It is therefore important to determine the critical p by simulating the original model.

Let us recall that in the simplified model for early times, the growth of $R(t)$ was observed to be exponential [49]. In that model, only the first term in (3.12) was used to represent the effect of fermionic matrices. We consider that the exponential expansion occurs also in the original model at early times as is suggested by direct Monte Carlo studies up to $N \leq 24$ [48]. At late times, however, the sub-leading term in (3.12) becomes important due to the expansion of space, and that would affect the expanding behavior. Note that the repulsive potential for the eigenvalues of A_0 is obtained from integrating out the fermionic matrices without the sub-leading term. Therefore one of the effects of the sub-leading term would be to make the repulsive potential less effective. Considering that the bosonic model mimics such a situation, we speculate that the exponential expansion in the original model changes into a power-law expansion at some point in time, where the sub-leading term in (3.12) becomes important. According to this scenario, the number of e-foldings is determined dynamically in the Lorentzian type IIB matrix model. It would be interesting to confirm the transition directly by simulating the original model. An attempt in doing this with a systematic approximation is in progress.

On the other hand, the success of the complex Langevin approach in the toy model with SSB of $SO(4)$ encourages us to extend the analysis to the type IIB matrix model which has the $SO(10)$ symmetry. We expect that the $SO(10)$ symmetry is spontaneously broken down to $SO(4)$, which means that the 4d space emerges from the 10d space predicted by superstring theory. By the Gaussian expansion method, it is indicated that the $SO(10)$ seems to be broken down to $SO(3)$ rather than $SO(4)$. However, as mentioned above, this analysis is based on an ansatz and an approximation. Therefore, it is important to confirm this observation from first principle calculation using the complex Langevin method.

The improvement using extra source terms in the action might be also helpful for other systems such as the finite density QCD or the random matrix theory. In particular, it is known that the complex Langevin method does not work in high density and low temperature region due to the singular drift problem. We hope that the new technique we developed in this thesis will be useful also in this case.

Acknowledgments

I would like to thank Asato Tsuchiya, Takehiro Azuma and Sang-Woo Kim for their collaboration on the studies in this thesis. In particular, I thank my supervisor Jun Nishimura for continuous encouragement and advice. I also would like to thank all the staffs and students at the theory center in KEK. And I would like to the JSPS fellows for financial support.

Finally, this research used computational resources of the K computer of the HPCI system provided by the AICS through the HPCI System Research Project (Project ID : hp130063). The supercomputer FX10 at University of Tokyo has been used in developing our code for parallel computing. Computation for the (5+1)D matrix model discussed in the Appendix B was carried out mostly on PC clusters at KEK.

A Details of Monte Carlo simulation

In this section we give the details on how we perform Monte Carlo simulation of the bosonic model (4.6).

First the delta functions in (4.6) are replaced by Gaussian potentials as

$$V_{\text{pot}} = \frac{1}{2}\gamma_C \left(\frac{1}{N} \text{Tr} (F_{\mu\nu} F^{\mu\nu}) \right)^2 + \frac{1}{2}\gamma_L \left(\frac{1}{N} \text{Tr} (A_i)^2 - 1 \right)^2, \quad (\text{A.1})$$

where the coefficients γ_C and γ_L are taken large enough to fix each observable to the specified value. The values used in actual simulation are given in table 6.

Another important issue we have to take care of is the spontaneous breaking of the shift symmetry $A_0 \mapsto A_0 + \alpha \mathbf{1}$. For instance, let us consider calculating the expectation value $R^2(t)$ defined in (3.23). The peak of this quantity measured for each configuration fluctuates considerably. This reflects the ambiguity in choosing the origin of the time coordinate, and we should fix it before taking the ensemble average. Here we fix it by introducing a potential

$$V_{\text{sym}} = \frac{1}{2}\gamma_{\text{sym}} \left(\frac{1}{N} \left[\text{Tr} (A_i)^2 \right]_{\text{left}} - \frac{1}{N} \left[\text{Tr} (A_i)^2 \right]_{\text{right}} \right)^2, \quad (\text{A.2})$$

$$\left[\text{Tr} (A_i)^2 \right]_{\text{left}} = \sum_{i=1}^d \sum_{a+b < N+1} |(A_i)_{ab}|^2, \quad (\text{A.3})$$

$$\left[\text{Tr} (A_i)^2 \right]_{\text{right}} = \sum_{i=1}^d \sum_{a+b > N+1} |(A_i)_{ab}|^2, \quad (\text{A.4})$$

where the values of the coefficient γ_{sym} used in our simulation are given in table 6.

To summarize, the model we simulate is given by

$$\begin{aligned} Z &= \int \prod_{a=1}^N d\alpha_a \prod_{i=1}^d dA_i e^{-S_{\text{eff}}} , \\ S_{\text{eff}} &= -2 \log \Delta(\alpha) + V_{\text{pot}} + V_{\text{sym}} . \end{aligned} \quad (\text{A.5})$$

The simulation of the model (A.5) can be performed by using the Hybrid Monte Carlo (HMC) method. First we rewrite the model by introducing auxiliary variables p_a and $(X_i)_{ab}$ ($a, b = 1, \dots, N$) with the action

$$S_{\text{HMC}} = \frac{1}{2} \sum_a (p_a)^2 + \frac{1}{2} \text{Tr} (X_i)^2 + S_{\text{eff}}[\alpha, A] . \quad (\text{A.6})$$

Here p_a are real variables, whereas X_i are traceless Hermitian matrices. We update all the variables in the model (A.6) in the following way. First we regard p_a as the conjugate momenta of α_a and X_i as the conjugate momenta of A_i . Then we regard S_{HMC} in (A.6) as the Hamiltonian H and solve the classical equations of motion obtained as the Hamilton equations

$$\begin{aligned} \frac{d\alpha_a}{d\tau} &= \frac{\partial H}{\partial p_a} = p_a, & \frac{dp_a}{d\tau} &= -\frac{\partial H}{\partial \alpha_a} = -\frac{\partial S_{\text{eff}}}{\partial \alpha_a} , \\ \frac{dA_i}{d\tau} &= \frac{\partial H}{\partial X_i} = X_i^*, & \frac{dX_i}{d\tau} &= -\frac{\partial H}{\partial A_i} = -\frac{\partial S_{\text{eff}}}{\partial A_i} , \end{aligned} \quad (\text{A.7})$$

for some fictitious time τ . This part of the algorithm is called the Molecular Dynamics. In order to solve the Hamilton equations (A.7) numerically, we discretize them using the so-called leap-frog discretization, which maintains reversibility with respect to τ . Starting from the previous configuration at $\tau = 0$, we obtain a new configuration at $\tau = \tau_f$ by solving (A.7) with the step size $\Delta\tau$ so that $\tau_f = N_\tau \cdot \Delta\tau$, where N_τ is the number of steps. We accept the new configuration with the probability $\min(1, \exp(-\Delta S_{\text{HMC}}))$, where $\Delta S_{\text{HMC}} \equiv S_{\text{HMC}}(\tau_f) - S_{\text{HMC}}(0)$, following the idea of the Metropolis algorithm to satisfy the detailed balance. The important point here is that S_{HMC} is nothing but the Hamiltonian H , which is preserved in the classical dynamics if the equations (A.7) are solved exactly. In fact, ΔS_{HMC} becomes non-zero due to the discretization, but it is guaranteed to be a small quantity of the order of $(\Delta\tau)^2$. By choosing sufficiently small $\Delta\tau$, the acceptance rate can be kept reasonably high, which enables the system to move around efficiently in the configuration space. Note also that the auxiliary variables p_a and $(X_i)_{ab}$ appear only as the Gaussian terms in (A.6). Therefore, we can update them independently by using normalized Gaussian random numbers. This procedure of refreshing the conjugate momenta should be done each

N	γ_C/N^2	γ_L/N^2	γ_{sym}	N_τ	$\Delta\tau$	trajectories
128	1	100	200	20	0.0015	2,000,000
256	1	100	200	10	0.0008	1,600,000
384	1	100	2,000	10	0.0004	1,000,000
512	1	100	6,000	10	0.00025	2,250,000

Table 6: The values of the parameters γ_C , γ_L and γ_{sym} in (A.5) used in our simulation. We also give the values of the parameters in the HMC algorithm: the number of steps N_τ in the Molecular Dynamics and its step size $\Delta\tau$. In the last column, we give the number of “trajectories”, which represents how many times we solve the Molecular Dynamics after thermalization to achieve the statistics of our data.

time we start a Molecular Dynamics procedure.

To summarize, the HMC algorithm as applied to our system can be described as follows.

1. Generate initial configurations of $p_a(0)$ and $X_i(0)$ with Gaussian distribution $\propto e^{-\frac{1}{2}\sum_a(p_a)^2}$ and $e^{-\frac{1}{2}\text{Tr}(X_i)^2}$, respectively.
2. Evolve the fields $p_a(\tau)$, $X_i(\tau)$, $\alpha_a(\tau)$ and $A_i(\tau)$ for fictitious time τ_f according to the discretized Molecular Dynamics.
3. Accept the configuration of $\alpha_a(\tau_f)$ and $A_i(\tau_f)$ obtained at the end of Molecular Dynamics with the probability $\min(1, e^{-\Delta H})$, where $\Delta H = H(\tau_f) - H(0)$.

In the HMC algorithm, there are two parameters⁹ $\Delta\tau$ and τ_f . In the present work we choose them as in table 6.

B Results for the (5+1)D version of the bosonic model

In this section we present our results¹⁰ for a bosonic model that can be obtained by omitting fermionic matrices in the (5+1)D version of the type IIB matrix model. The latter model is obtained formally by dimensional reducing the 6D $\mathcal{N} = 1$ super Yang-Mills theory to a point, and it consists of six bosonic matrices A_μ ($\mu = 1, \dots, 6$) and four fermionic matrices Ψ_α ($\alpha = 1, \dots, 4$) representing four components of a 6D Weyl spinor. The form of the bosonic part of the action is the same as that of the original type IIB matrix model, which is given in (3.2).

⁹These parameters can be optimized as follows. For fixed τ_f , it is optimal to choose $\Delta\tau$ so that $\Delta\tau \times$ (acceptance rate) is maximized. Then τ_f can be optimized to minimize the auto-correlation time in units of one step in the Molecular Dynamics.

¹⁰Preliminary results shown in Fig. B.2 (Right) are published in the proceedings [48].

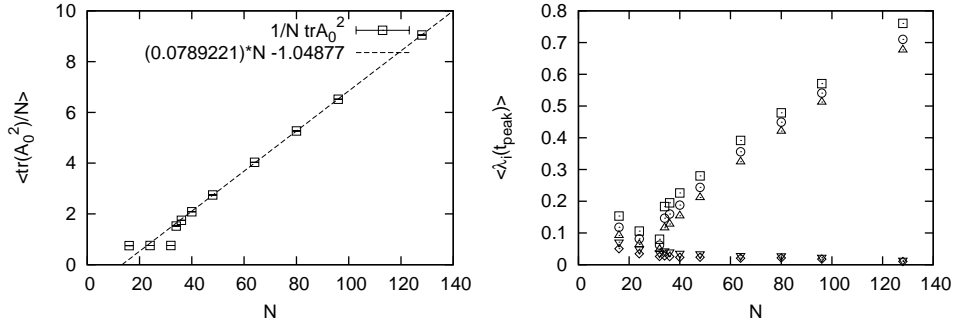


Figure B.1: (Left) The extent $\langle \frac{1}{N} \text{Tr}(A_0)^2 \rangle$ of the eigenvalue distribution of A_0 is plotted against N for the (5+1)D model. It starts to increase at $N = N_c = 34$. (Right) The expectation values $\langle \lambda_i(t) \rangle$ of the five eigenvalues of $T_{ij}(t)$ at $t = t_{\text{peak}}$ are plotted against N for the (5+1)D model.

N	γ_C/N^2	γ_L/N^2	γ_{sym}	N_τ	$\Delta\tau$	trajectories
64	1	100	1,000	10	0.0015	200,000
96	1	100	1,000	10	0.001	400,000
128	1	100	2,000	10	0.001	2,400,000

Table 7: The values of the parameters γ_C , γ_L and γ_{sym} in (A.1) used in our simulation of the (5+1)D model. We also give the values of parameters in the HMC algorithm, (See caption of table 6 for explanation.)

In Fig. B.1 (Left), we plot the extent $\langle \frac{1}{N} \text{Tr}(A_0)^2 \rangle$ of the eigenvalue distribution of A_0 against N . In Fig. B.1 (Right), we plot the expectation values $\lambda_i(t)$ of the five eigenvalues of $T_{ij}(t)$ at $t = t_{\text{peak}}$ against N . While the qualitative behaviors are the same as in the (9+1)D case shown in Fig. 4.4, we find that the critical N_c is smaller and the slope of the linearly increasing behavior of $\langle \frac{1}{N} \text{Tr}(A_0)^2 \rangle$ for $N \geq N_c$ is larger. We can understand this difference by considering the attractive potential between the eigenvalues of A_0 discussed below eq. (3.11). For general spatial dimensionality d , one obtains a factor $\Delta^{-2d}(\alpha)$ from integrating out the spatial matrices A_i at one loop. This factor acts as an attractive potential between the eigenvalues of A_0 , and it is stronger for larger d .

Below we discuss the properties of the (5+1)D model for $N \geq N_c$. (The parameters used in the simulation are listed in table 7.) We have determined the block size to be $n = 8, 10, 12$ for $N = 64, 96, 128$, respectively, from the fall-off of the off-diagonal elements of A_i as is done for the (9+1)D case in section 4.2.2. In Fig. B.2 (Left) we plot the expectation values $\langle \lambda_i(t) \rangle$ of the five eigenvalues of $T_{ij}(t)$ for $N = 128$, which shows that the $\text{SO}(5)$ symmetry is broken spontaneously down to $\text{SO}(3)$ after a critical time. From this kind of figures, we

N	n	t_c	$R(t_c)$	ε	Δ_t
64	8	-0.7248(5)	0.1575(4)	0.2281(6)	1.825(5)
96	10	-0.7692(3)	0.1276(3)	0.2157(4)	2.157(4)
128	12	-0.8037(1)	0.1070(1)	0.2048(2)	2.457(2)

Table 8: The block size n , the critical time t_c , the extent of space $R(t_c)$ at the critical time, which are used in the (5+1)D model to make the plot in Fig. B.2 (Right). We also present the explicit values of the average “lattice spacing” ε and the “volume” Δ_t in the temporal direction, which are plotted in Fig. B.3 (Right).

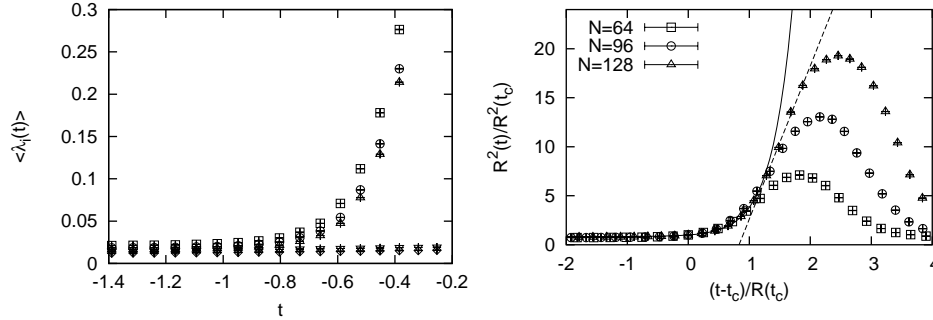


Figure B.2: (Left) The expectation values $\langle \lambda_i(t) \rangle$ of the five eigenvalues of $T_{ij}(t)$ are plotted against t for the (5+1)D model with $N = 128$. The critical time is determined as $t_c = -0.8037(1)$. (Right) The extent of space $R^2(t)$ is plotted against $x = (t - t_c)/R(t_c)$ for $N = 64, 96$ and 128 in the (5+1)D model. The solid line represents a fit of the $N = 128$ data to $R^2(t)/R^2(t_c) = a + (1 - a) \exp(bx)$ for $0.4 \leq x \leq 1.2$, which gives $a = 0.839(9)$ and $b = 2.91(6)$. The dashed line represents a fit of the $N = 128$ data to $R^2(t)/R^2(t_c) = cx + d$ for $1.2 \leq x \leq 2.0$, which gives $c = 15.6(5)$ and $d = -13.0(8)$.

can determine the critical time t_c for each N as described¹¹ in section 4.2.2.

In Fig. B.2 (Right) we show the large- N scaling behavior of the extent of space $R^2(t)$. Explicit values of $R(t_c)$, together with the block size n and the critical time t_c , which are used to make this plot, are given in table 8. The power-law expansion (4.7) is observed at late times similarly to the (9+1)D model.

In Fig. B.3 (Left) we plot the t -dependent “lattice spacing”, which shows how the continuum limit is achieved as N increases. The average “lattice spacing” ε and the “volume” Δ_t in the temporal direction are given in table 8. In Fig. B.3 (Right) we plot them in the log scale. The straight lines represent fits to the power-law behaviors.

¹¹Unlike in the (9+1)D case, there was no need to adjust the value of t_c to obtain the large- N scaling behavior in Fig. B.2 (Right).

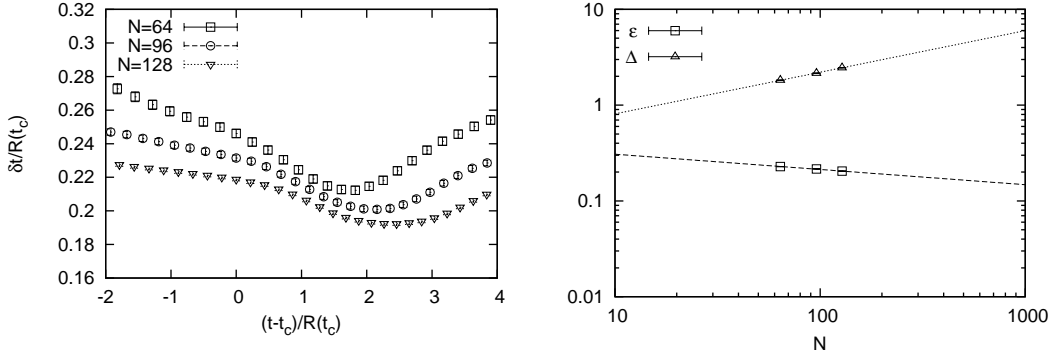


Figure B.3: (Left) The “lattice spacing” $\frac{\delta t}{R(t_c)}$ is plotted against $(t-t_c)/R(t_c)$ for the (5+1)D model. (Right) The average “lattice spacing” ε and the “volume” in the temporal direction Δ_t is plotted against N in the log scale for the (5+1)D model. The straight lines represent fits to the power-law behaviors $\varepsilon = a N^{-p}$, where $a = 0.44(2)$, $p = 0.16(1)$ and $\Delta_t = b N^q$, where $b = 0.30(2)$, $q = 0.43(1)$ using all the data.

C The differences between two simplified models

We have seen that the simplified model for the early times and for the late times exhibit different expanding behaviors as space-time. In this section we discuss what causes this difference.

In this Appendix, we refer to the simplified models for early times as the VDM model and for the late times as the bosonic model, respectively. The partition functions are defined in (4.3) for the VDM model and (4.6) for the bosonic model, where we find two differences. The first one is the power of the van der Monde determinant, and the second one is the presence or absence of the IR cutoffs in the temporal direction..

Let us recall that the van der Monde determinant $\Delta^{18}(\alpha)$ in the VDM model comes from two parts, the Faddeev-Popov determinant by the gauge fixing (3.9) and the Pfaffian for A_0 (4.2). They act on the eigenvalues of A_0 as a repulsive force between them, which cancels the attractive force coming from the bosonic one-loop effective potential for A_0 . Because of this, the eigenvalues of A_0 can extend freely in the VDM model. However, this is not the case in the bosonic model because there exists an attractive force between them due to the absence of fermions. Therefore, one can expect that this difference affects the eigenvalue distribution of A_0 . In Fig. C.1, we plot the expectation values of the eigenvalues α_k ($k = 1, \dots, N$) of A_0 against k with $N = 256$, $\kappa = 16$ for the VDM model and with $N = 256$ for the bosonic model. This figure shows that difference between two adjacent α_k for the bosonic model is slightly narrower than that for the VDM model for $|\alpha_k| \lesssim 2$, while the difference becomes wider than that for the VDM model for $|\alpha_k| \gtrsim 2$. Since the difference of α_k appears in the

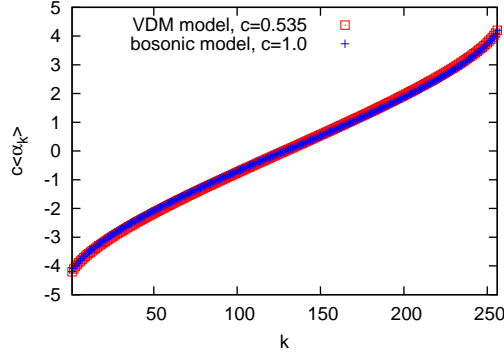


Figure C.1: The expectation values of eigenvalue α_k are plotted against k with $N = 256$ and $\kappa = 16$ for the VDM model and $N = 256$ for the bosonic model. The result of the VDM model is rescaled by a parameter c so that the maximum value of α_k coincides with the one for the bosonic model.

bosonic action S_b as

$$S_b = \frac{1}{4g^2} \left\{ -2 \sum_{a,b}^N (\alpha_a - \alpha_b)^2 |(A_i)_{ab}|^2 + \text{Tr} \left([A_i, A_j]^2 \right) \right\},$$

the matrix components $(A_i)_{ab}$ close to the diagonal elements of A_i are strongly influenced by the difference $(\alpha_a - \alpha_b)$ for small $|a - b|$. How this influence appears in the behaviors of $R(t)$ is not obvious, though.

Let us also point out that the behavior of fluctuations of α_k is different in the two models. We define the fluctuation of α_k by

$$\delta\alpha_k = \sqrt{\langle \alpha_k^2 \rangle - \langle \alpha_k \rangle^2}, \quad (\text{C.1})$$

and plot it against k for the VDM model with $N = 256$, $\kappa = 16$ and for the bosonic model with $N = 256$ in Fig. C.2. It turns out that the α_k in the VDM model are almost frozen. On the other hand, it turns out that the fluctuation of α_k is larger in the bosonic model. This can be understood because the eigenvalue distribution of α_k in the bosonic model is easy to contract due to the attractive force between α_k . It is not clear whether this fluctuation causes the difference of the expanding behavior of $R(t)$.

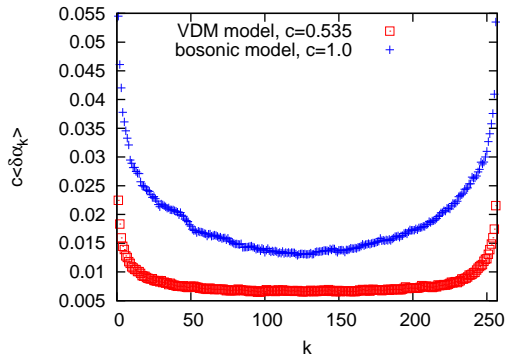


Figure C.2: The fluctuation of α_k are plotted against k with $N = 256$ and $\kappa = 16$ for the VDM model and $N = 256$ for the bosonic model. The result of the VDM model is rescaled by the parameter c which is the same value as the one used in Fig. C.1.

D Review of stochastic quantization and the Langevin equation

In this Appendix, we review the stochastic quantization using the Langevin equation. This review is based on the paper provided by P. H. Damgaard and H. Huffel [52].

Here, we consider the Brown motion as an example for the stochastic process. The Langevin equation for the Brownian motion is given by

$$m \frac{d}{dt} \mathbf{v}(t) = -\alpha \mathbf{v}(t) + \boldsymbol{\eta}(t), \quad (\text{D.1})$$

where m is a mass of a particle and $\mathbf{v}(t)$ is the velocity of the particle. α is the friction coefficient of the fluid in which the particle moves. $\boldsymbol{\eta}(t)$ is a white noise generated with the Gaussian distribution, which represents the force vector acting on the particle due to the collision to molecules in the fluid. It follows from the Gaussian distribution that

$$\begin{aligned} \langle \boldsymbol{\eta}(t) \rangle_{\boldsymbol{\eta}} &= 0, \\ \langle \boldsymbol{\eta}(t) \boldsymbol{\eta}(t') \rangle_{\boldsymbol{\eta}} &= 2\delta(t - t'), \end{aligned}$$

where the $\langle \dots \rangle_{\boldsymbol{\eta}}$ is defined as

$$\langle \mathcal{O} \rangle_{\boldsymbol{\eta}} \equiv \frac{\int D\boldsymbol{\eta} \mathcal{O} e^{-\frac{1}{4} \int dt \boldsymbol{\eta}^2(t)}}{\int D\boldsymbol{\eta} e^{-\frac{1}{4} \int dt \boldsymbol{\eta}^2(t)}}.$$

In the statistical mechanics, it is known that the conditional probability distribution $P(v, t | v_0, t_0) \equiv$

$P(v, t)$ satisfies the Focker-Planck (FP) equation. Here, $P(v, t|v_0, t_0)$ represents the probability such that the particle's velocity \mathbf{v}_0 at t_0 becomes \mathbf{v} at t . The probability distribution given as the solution to the Langevin equation (D.1) also satisfies the FP equation in the form of

$$\frac{\partial}{\partial t} P(v, t) = \frac{\partial}{\partial v} \left(v + \frac{\partial}{\partial v} \right) P(v, t), \quad (\text{D.2})$$

where we set $m = \alpha = 1$. In what follows, we prove that the $P(v, t)$ given from the Langevin eq. satisfies the FP eq..

Firstly, let us consider the expectation value of an arbitrary function of $v(t)$ defined as

$$\langle f(v(t)) \rangle = \int dv f(v) P(v, t), \quad (\text{D.3})$$

where $P(v, t)$ is the probability distribution function of $v(t)$ given as the solution to the eq. (D.1). Taking the time derivative for the left hand side of the above equation,

$$\frac{d}{dt} \langle f(v(t)) \rangle = \left\langle \frac{\delta f}{\delta v} \frac{dv}{dt} \right\rangle = \left\langle \frac{\delta f}{\delta v} (-v + \eta) \right\rangle, \quad (\text{D.4})$$

where we used the Langevin eq. in the last step. Then, using the relation

$$\langle g(v(t)) \eta(t) \rangle = \left\langle \frac{\delta g}{\delta v(t)} \right\rangle, \quad (\text{D.5})$$

we obtain

$$\begin{aligned} \frac{d}{dt} \langle f(v(t)) \rangle &= \left\langle \frac{\delta f}{\delta v} (-v + \eta) \right\rangle \\ &= \left\langle -\frac{\delta f}{\delta v} v + \frac{\delta}{\delta v} \frac{\delta f}{\delta v} \right\rangle. \end{aligned}$$

Rewriting it with the integration form,

$$\begin{aligned} \left\langle -\frac{\delta f}{\delta v} v + \frac{\delta}{\delta v} \frac{\delta f}{\delta v} \right\rangle &= \int dv \left(-\frac{\partial f}{\partial v} v + \frac{\partial^2 f}{\partial v^2} \right) P(v, t) \\ &= \int dv f(v) \frac{\partial}{\partial v} \left(v + \frac{\partial}{\partial v} \right) P(v, t) + \text{total derivative} \end{aligned}$$

Then, one can get the relation

$$\int dv f(v) \frac{\partial}{\partial v} \left(v + \frac{\partial}{\partial v} \right) P(v, t) = \int dv f(v) \frac{d}{dt} P(v, t) \quad (\text{D.6})$$

which indicates the Focker-Planck equation.

We note that the relation (D.5) can be shown as follows.

$$\begin{aligned}
\langle g(v(t)) \eta(t) \rangle &= \int D\eta g \eta e^{-\frac{1}{4} \int \eta^2(\tau) d\tau} \\
&= -2 \int D\eta g \frac{\delta}{\delta \eta} e^{-\frac{1}{4} \int \eta^2(\tau) d\tau} \\
&= 2 \int D\eta \frac{\delta g}{\delta \eta} e^{-\frac{1}{4} \int \eta^2(\tau) d\tau} \\
&= 2 \left\langle \frac{\delta g}{\delta \eta} \right\rangle \\
&= 2 \left\langle \frac{\delta g}{\delta v} \frac{\delta v}{\delta \eta} \right\rangle.
\end{aligned}$$

And we use the

$$v(t) = \int_0^\infty d\tau \theta(t - \tau) e^{-(t-\tau)} \eta(\tau),$$

from which we find

$$\frac{\delta v(t)}{\delta \eta(t)} = \theta(t - \tau) e^{-(t-\tau)} \Big|_{\tau=t} = \theta(0) = \frac{1}{2}.$$

Thus, we obtain the relation (D.5).

The proof of the equivalence to the path integral quantization

In fact, the expectation value obtained for the stochastic quantization in the large fictitious time limit is equivalent to the one defined in the path integral quantization.

The Focker-Planck equation for the system described by an action S is given as

$$\frac{d}{dt} P(x, t) = \frac{\partial}{\partial x} \left(\frac{\partial}{\partial x} + \frac{\partial S}{\partial x} \right) P(x, t). \quad (\text{D.7})$$

Assuming that $P(x, t) = \psi(x, t) e^{-S/2}$, we can rewrite the (D.7) into the Schrodinger type equation

$$\frac{d}{dt} \psi(x, t) = -2H\psi(x, t), \quad (\text{D.8})$$

where

$$H = \frac{1}{2} \left(-\frac{\partial}{\partial x} + \frac{1}{2} \frac{\partial S}{\partial x} \right) \left(\frac{\partial}{\partial x} + \frac{1}{2} \frac{\partial S}{\partial x} \right)$$

is a self-adjoint operator with semi-positive definite. When one denotes the eigenstate of H

by ψ_n , the r.h.s. of the (D.8) can be written as

$$H\psi_n(x) = E_n\psi_n(x),$$

where E_n is n -th eigenvalue corresponding to the ψ_n . Therefore, one can represent $\psi(x, t)$ as

$$\psi(x, t) = \sum_{n=0}^{\infty} a_n \psi_n(x) e^{-E_n t}.$$

The eigenfunction with zero energy is

$$\psi_0(x) = e^{-\frac{1}{2}S} \quad (\text{D.9})$$

up to the normalization. So, in the large time limit, the probability distribution function follows as

$$\lim_{t \rightarrow \infty} P(x, t) = a_0 e^{-S}.$$

By fixing the normalization to be

$$\lim_{t \rightarrow \infty} \int dx P(x, t) = 1,$$

one obtains the probability distribution function in the $t \rightarrow \infty$ limit as

$$P_{\text{eq}}(x) = \lim_{t \rightarrow \infty} P(x, t) = \frac{e^{-S}}{\int dx e^{-S}}.$$

Then, one can show that the expectation value defined with P_{eq} is equivalent to the one defined in the path integral formalism as follows.

$$\begin{aligned} \lim_{t \rightarrow \infty} \langle O(x^{(\eta)}(t)) \rangle_{\eta} &= \lim_{t \rightarrow \infty} \frac{\int D\eta O(x^{(\eta)}(t)) e^{-\frac{1}{4} \int dt \eta^2(t)}}{\int D\eta e^{-\frac{1}{4} \int dt \eta^2(t)}} \\ &= \lim_{t \rightarrow \infty} \frac{\int D\eta \int dx O(x) \delta(x - x^{(\eta)}(t)) e^{-\frac{1}{4} \int dt \eta^2(t)}}{\int D\eta e^{-\frac{1}{4} \int dt \eta^2(t)}} \\ &= \lim_{t \rightarrow \infty} \int dx O(x) \langle \delta(x - x^{(\eta)}(t)) \rangle_{\eta} \\ &= \lim_{t \rightarrow \infty} \int dx O(x) P(x) \\ &= \frac{\int dx O(x) e^{-S}}{\int dx e^{-S}} \\ &= \langle O(x) \rangle \end{aligned}$$

The discretized Langevin equation

In order to solve the Langevin equation numerically, we introduce the discretized version of the Langevin equation. The expectation values in the original quantum theory are given from the classical evolution in the fictitious time as we have shown above. In what follows, we derive the discretized Langevin equation from the discretized Hamilton equation by regarding the conjugate momentum as a noise term.

For a given classical action $S[\varphi]$, the Hamiltonian is given as

$$H = \int d^d x \frac{1}{2} \pi^2(x; t) + S[\varphi],$$

where $\varphi(x; t)$ is a field depending on the space-time variable x_μ and fictitious time t and $\pi(x; t)$ is the conjugate momentum of the field φ .

The expectation values of observables $O(\varphi)$ are defined by

$$\langle O(\varphi) \rangle = Z^{-1} \int D\pi D\varphi O(\varphi) e^{-H[\pi, \varphi]}$$

with the normalization

$$Z = \int D\pi D\varphi e^{-H[\pi, \varphi]}.$$

Integrating out the conjugate momenta π reduces the path integral as

$$Z = \int D\varphi e^{-S[\varphi]},$$

from which one can see that these are equivalent quantization. The classical dynamics of the field φ and conjugate momenta π in the fictitious time t is described by the Hamilton equation

$$\frac{\partial \varphi(x; t)}{\partial t} = \frac{\delta H}{\delta \pi(x; t)} = \pi(x; t), \quad (\text{D.10})$$

$$\frac{\partial \pi(x; t)}{\partial t} = \frac{\delta H}{\delta \varphi(x; t)} = -\frac{\delta S}{\delta \varphi(x; t)}. \quad (\text{D.11})$$

Let us discretize the Hamilton equation (D.10) and (D.11) in the fictitious time direction by introducing discretized time $\Delta t = t_{n+1} - t_n$. Then, the discretized version of eq. (D.10) up

to second order of Δt is given as

$$\begin{aligned}\varphi(x; t_n + \Delta t) &= \varphi(x; t_n) + \frac{\partial \varphi(x; t_n)}{\partial t} \Delta t + \frac{1}{2} \frac{\partial^2 \varphi(x; t_n)}{\partial t^2} \Delta t^2 \\ \varphi(x; t_{n+1}) &= \varphi(x; t_n) + \pi(x; t_n) \Delta t - \frac{1}{2} \frac{\delta S[\varphi]}{\delta \varphi(x; t_n)} \Delta t^2\end{aligned}\quad (\text{D.12})$$

Note that the conjugate momenta $\pi(x)$ have the Gaussian distribution and these are independent of the values of the field $\varphi(x)$. Therefore, instead of solving the classical Hamilton equation with initial given momenta, by refreshing the momenta randomly after every step, we obtain the classical Langevin dynamics in fictitious time. Therefore, by rewriting the conjugate momenta and the discretized time as

$$\sqrt{2}\pi(x; t_n) \rightarrow \eta(t), \quad \frac{1}{2}\Delta t^2 \rightarrow \epsilon,$$

we obtain the discretized version of the Langevin equation

$$\varphi(x; t_{n+1}) = \varphi(x; t_n) - \epsilon \frac{\partial S[\varphi]}{\partial \varphi(x)} + \sqrt{\epsilon} \eta(t), \quad (\text{D.13})$$

where the $\eta(x)$ obeys the probability distribution $e^{-\frac{1}{4}\sum_t \eta(t)}$ and hence, we obtain

$$\langle \eta(t) \eta(t') \rangle_\eta = 2\delta_{t,t'}.$$

With this discretized Langevin equation, we can also derive the Focker-Planck equation. To do this, let us consider the expectation value of a function $f(x)$ as

$$\langle f(\varphi(x; t_n)) \rangle_\eta = \int dx f(\varphi(x)) P(x; t_n). \quad (\text{D.14})$$

The time differential of this expectation value is given by

$$\begin{aligned}\langle f(\varphi(x; t_{n+1})) \rangle_\eta - \langle f(\varphi(x; t_n)) \rangle_\eta &= \left\langle f\left(\varphi(x; t_n) - \epsilon \frac{\partial S[\varphi]}{\partial \varphi(x)} + \sqrt{\epsilon} \eta(t)\right) \right\rangle_\eta - \langle f(\varphi(x; t_n)) \rangle_\eta \\ &= \left\langle \frac{\partial f}{\partial \varphi} \left(-\epsilon \frac{\partial S}{\partial \varphi}\right) + \frac{1}{2} \frac{\partial^2 f}{\partial \varphi^2} (\sqrt{\epsilon})^2 \eta(t) \eta(t) \right\rangle_\eta + O(\epsilon^2),\end{aligned}\quad (\text{D.15})$$

where the terms proportional to $\sqrt{\epsilon}$ vanish because those terms always have odd number of

$\eta(t)$ whose expectation value should be zero. Therefore,

$$\begin{aligned} \text{l.h.s. of eq. (D.15)} &= \epsilon \int dx \left(-\frac{\partial f}{\partial \varphi} \frac{\partial S}{\partial \varphi} + \frac{\partial^2 f}{\partial \varphi^2} \right) P(x; t_n) + O(\epsilon^2) \\ &= \epsilon \int dx f(\varphi(x)) \frac{\partial}{\partial \varphi} \left(\frac{\partial S}{\partial \varphi} + \frac{\partial}{\partial \varphi} \right) P(x; t_n) + O(\epsilon^2). \end{aligned} \quad (\text{D.16})$$

On the other hand, the left hand side of (D.15) can be given as

$$\langle f(\varphi(x; t_{n+1})) \rangle_\eta - \langle f(\varphi(x; t_n)) \rangle_\eta = \int dx f(x) (P(x; t_{n+1}) - P(x; t_n)). \quad (\text{D.17})$$

Therefore, one obtains the relation

$$P(x; t_{n+1}) - P(x; t_n) = \epsilon \frac{\partial}{\partial \varphi} \left(\frac{\partial S}{\partial \varphi} + \frac{\partial}{\partial \varphi} \right) P(x; t_n) + O(\epsilon^2), \quad (\text{D.18})$$

from which the continuum version of the FP eq. is again derived by taking the $\epsilon \rightarrow 0$ limit.

E The result for the another fermion mass term

In this Appendix, we show the result obtained by introducing the fermion mass only in the 3rd direction as

$$\alpha_i = (0, 0, m_f, 0). \quad (\text{E.1})$$

We again use the boson mass as in (6.13). Note that we have also taken care of the hermiticity of X_i by using the gauge cooling with respect to the norm (6.33) for every step. We plot the eigenvalue distribution of the mass deformed Dirac operator (6.34) for $\epsilon = 0.1$ and $m_f = 0.5$ in Fig. E.1, in which it turns out that the eigenvalues shift to not the real direction but the imaginary direction. This can be understood since the fermion mass term α_3 contracts with $i\sigma_3$. In Fig. E.2, we plot the radial eigenvalue distribution function (6.36) of the Dirac operator against the distance R from the pole of the drift term for $m_f = 0.2$ and 0.5 . This figure shows that the eigenvalue distributions damp rapidly around $R = 0$ even for small ϵ . As a result, it turns out that we can take ϵ closer to zero than the case of the fermion mass (6.35).

In Fig. E.3, we plot the expectation values of the order parameters $\rho_{\epsilon, m_f}^{(i)}$ defined in (6.37) against ϵ for $m_f = 0.3$. By extrapolating ϵ to zero, we find that the values of $\rho_{m_f}^{(1)}$ and $\rho_{m_f}^{(2)}$ are close to each other as well as in the case of the fermion mass (6.35). This result shows that SO(2) symmetry remains for the fermion mass (E). However, we note that this fermion mass explicitly breaks SO(4) symmetry down to SO(2) even in the $\epsilon \rightarrow 0$ limit since the order of

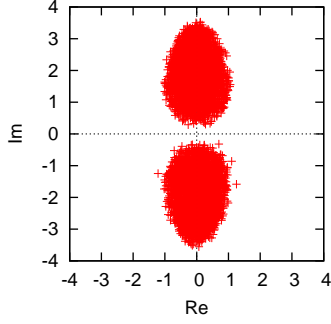


Figure E.1: The scattered plot of the eigenvalues of the mass deformed Dirac operator for $\epsilon = 0.1$ with $m_f = 0.5$ in the $r = 1$ case, where m_f is now introduced in the only third direction.

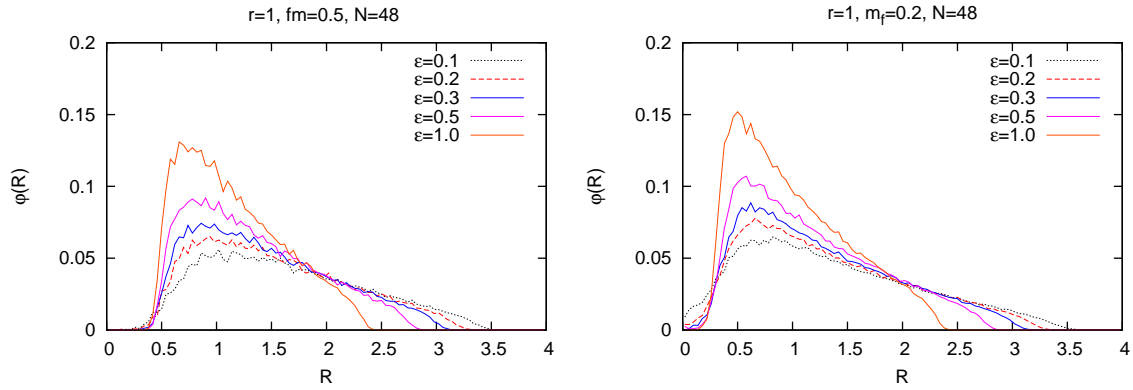


Figure E.2: (Left) The radial distribution function $\varphi(R)$ for the eigenvalues of the Dirac operator is plotted against the distance R from the pole for the fermion mass (E.1) with $m_f = 0.5$. (Right) We also plot $\varphi(R)$ against R with $m_f = 0.2$.

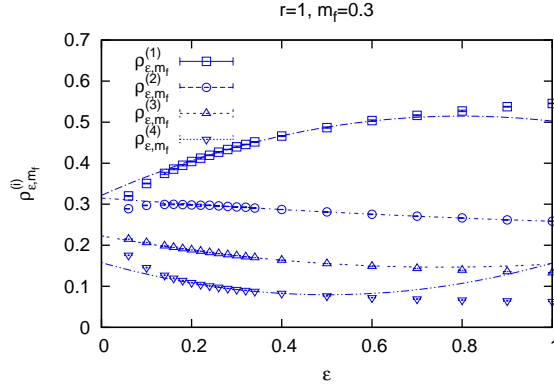


Figure E.3: The expectation values of the order parameters $\rho_{\epsilon, m_f}^{(i)}$ are plotted against ϵ for $m_f = 0.3$. The broken lines are fits of the data for each $\rho_{\epsilon, m_f}^{(i)}$ to a function $f(\epsilon) = a\epsilon^2 + b\epsilon + c$ for $\epsilon \geq 0.22$, which gives $\rho_{m_f}^{(1)} = 3.21(2) \times 10^{-1}$, $\rho_{m_f}^{(2)} = 3.150(6) \times 10^{-1}$, $\rho_{m_f}^{(3)} = 2.230(8) \times 10^{-1}$ and $\rho_{m_f}^{(4)} = 1.57(2) \times 10^{-1}$.

λ_i is now constrained as in (6.14). Therefore, we can not identify the spontaneous breaking of SO(4) or SO(3) for $\alpha_i = (0, 0, m_f, 0)$.

Thus, in order to make sure that the SO(4) symmetry is spontaneously broken down to SO(2), we have to extrapolate m_f to zero. In Fig. E.4 (Top-Left), we plot the expectation values of order parameter $\rho_{\epsilon, m_f}^{(1)}$ against ϵ for various values of m_f , in which the lines are fits of data points for each m_f to a function $f(\epsilon) = a\epsilon^2 + b\epsilon + c$. We also plot the other $\rho_{\epsilon, m_f}^{(i)}$ in the other panels in Fig. E.4.

Then, we plot $\rho_{m_f}^{(i)}$ obtained in this way against m_f in Fig. E.5. By extrapolating m_f to zero, we obtain $\rho^{(1)} = 3.5(2) \times 10^{-1}$, $\rho^{(2)} = 3.54(9) \times 10^{-1}$, $\rho^{(3)} = 1.74(5) \times 10^{-1}$ and $\rho^{(4)} = 1.07(8) \times 10^{-1}$. From these, we obtain $\langle \lambda_1 \rangle = 2.1(1)$, $\langle \lambda_2 \rangle = 2.12(5)$, $\langle \lambda_3 \rangle = 1.04(3)$ and $\langle \lambda_4 \rangle = 0.64(5)$, and we again find that the values of $\langle \lambda_1 \rangle$ and $\langle \lambda_2 \rangle$ are close to each other, which implies that the SSB from SO(4) to SO(2) occurs for the fermion mass (E.1). Moreover, these quantities are agree with the ones obtained by the Gaussian expansion method and the factorization method. Thus, we can confirm that the result is independent of the way to introduce mass terms to the fermions.

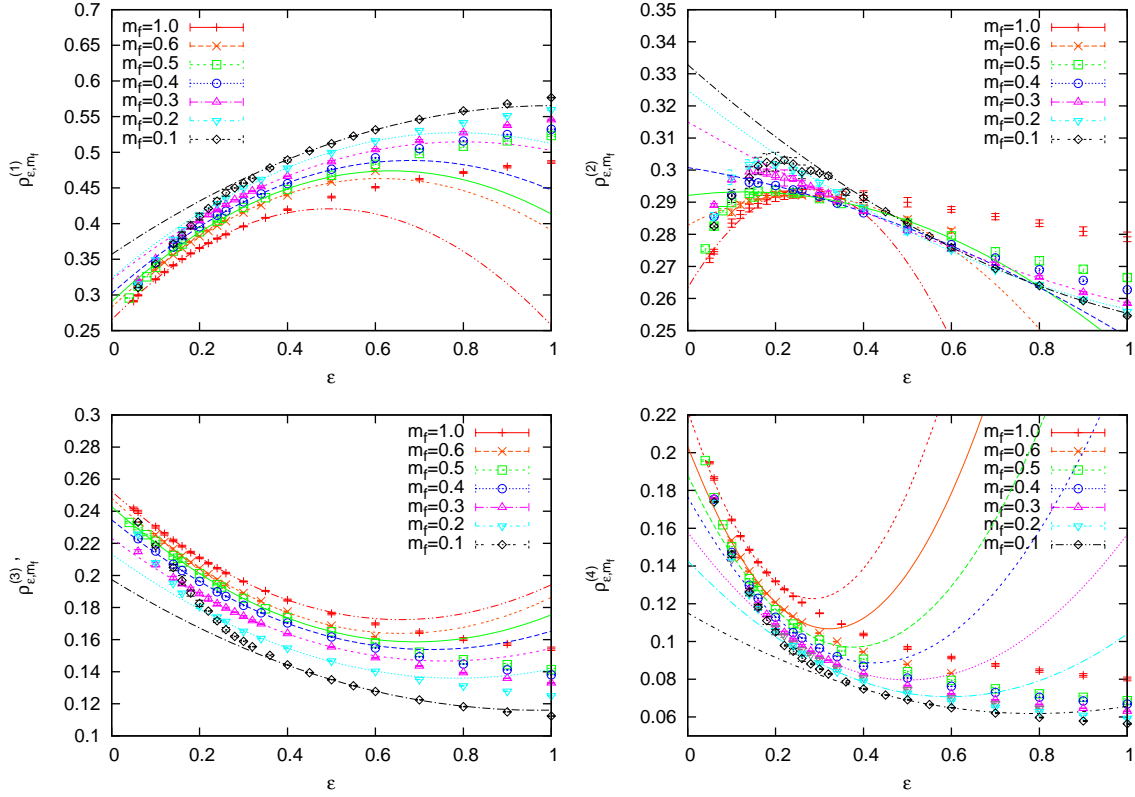


Figure E.4: (Top-left) The expectation values of the order parameter $\langle \lambda_1 \rangle_\epsilon$ are plotted against ϵ for various values of m_f . The lines are fits of the data for each m_f to a function $f(\epsilon) = a\epsilon^2 + b\epsilon + c$. The results for the other $\langle \lambda_i \rangle_\epsilon$ are also plotted in the other panels.

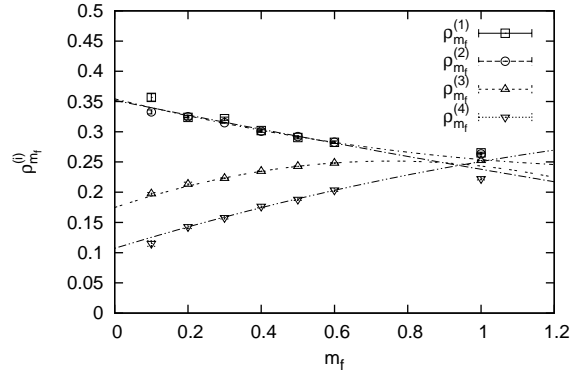


Figure E.5: The expectation values $\langle \lambda_i \rangle_{m_f}$ obtained by extrapolating ϵ to zero are plotted against m_f . The lines are fits of the data for each λ_i to a function $f(m_f) = am_f^2 + bm_f + c$ for $0.2 \leq m_f \leq 0.6$. We obtained $\langle \lambda_1 \rangle = 2.15(6)$, $\langle \lambda_2 \rangle = 2.15(7)$, $\langle \lambda_3 \rangle = 0.99(4)$ and $\langle \lambda_4 \rangle = 0.65(1)$ by extrapolating the fermion mass to zero.

References

- [1] N. Ishibashi, H. Kawai, Y. Kitazawa and A. Tsuchiya, *A large- N reduced model as superstring*, Nucl. Phys. B, **498** (1997) 467 [[arXiv:hep-th/9612115](#)].
- [2] T. Banks, W. Fischler, S. H. Shenker and L. Susskind, *M theory as a matrix model: a conjecture*, Phys. Rev. D **55** (1997) 5112 [[hep-th/9610043](#)].
- [3] R. Dijkgraaf, E. P. Verlinde and H. L. Verlinde, *Matrix string theory*, Nucl. Phys. B **500** (1997) 43 [[hep-th/9703030](#)].
- [4] R. J. Szabo, *Symmetry, gravity and noncommutativity*, Class. Quant. Grav. **23** (2006) R199 [[hep-th/0606233](#)].
- [5] H. Steinacker, *Emergent gravity from noncommutative gauge theory*, JHEP **0712** (2007) 049 [[arXiv:0708.2426](#) [[hep-th](#)]].
- [6] H. Steinacker, *Emergent gravity and noncommutative branes from Yang-Mills matrix models*, Nucl. Phys. B **810** (2009) 1 [[arXiv:0806.2032](#) [[hep-th](#)]].
- [7] D. Klammer and H. Steinacker, *Cosmological solutions of emergent noncommutative gravity*, Phys. Rev. Lett. **102** (2009) 221301 [[arXiv:0903.0986](#) [[gr-qc](#)]].
- [8] H. Steinacker, *Emergent geometry and gravity from matrix models: an introduction* Class. Quant. Grav. **27** (2010) 133001 [[arXiv:1003.4134](#) [[hep-th](#)]].
- [9] H. S. Yang, *Emergent gravity from noncommutative spacetime* Int. J. Mod. Phys. A **24** (2009) 4473 [[hep-th/0611174](#)].
- [10] H. S. Yang, *Emergent spacetime and the origin of gravity* JHEP **0905** (2009) 012 [[arXiv:0809.4728](#) [[hep-th](#)]].
- [11] H. S. Yang, *Emergent spacetime and cosmic inflation*, [arXiv:1503.00712](#) [[hep-th](#)].
- [12] H. Aoki, N. Ishibashi, S. Iso, H. Kawai, Y. Kitazawa and T. Tada, *Noncommutative Yang-Mills in IIB matrix model*, Nucl. Phys. B **565** (2000) 176 [[hep-th/9908141](#)].
- [13] J. Ambjorn, Y. M. Makeenko, J. Nishimura and R. J. Szabo, *Finite N matrix models of noncommutative gauge theory*, JHEP **9911** (1999) 029 [[hep-th/9911041](#)].
- [14] J. Ambjorn, Y. M. Makeenko, J. Nishimura and R. J. Szabo, *Nonperturbative dynamics of noncommutative gauge theory*, Phys. Lett. B **480** (2000) 399 [[hep-th/0002158](#)].

- [15] J. Ambjorn, Y. M. Makeenko, J. Nishimura and R. J. Szabo, *Lattice gauge fields and discrete noncommutative Yang-Mills theory*, JHEP **0005** (2000) 023 [[hep-th/0004147](#)].
- [16] H. Aoki, S. Iso, H. Kawai, Y. Kitazawa and T. Tada, *Space-time structures from IIB matrix model*, Prog. Theor. Phys. **99** (1998) 713 [[hep-th/9802085](#)].
- [17] T. Hotta, J. Nishimura and A. Tsuchiya, *Dynamical aspects of large N reduced models*, Nucl. Phys. B **545** (1999) 543 [[hep-th/9811220](#)].
- [18] J. Ambjorn, K. N. Anagnostopoulos, W. Bietenholz, T. Hotta and J. Nishimura, *Large N dynamics of dimensionally reduced 4D $SU(N)$ superYang-Mills theory*, JHEP **0007** (2000) 013 [[hep-th/0003208](#)].
- [19] J. Ambjorn, K. N. Anagnostopoulos, W. Bietenholz, T. Hotta and J. Nishimura, *Monte Carlo studies of the IIB matrix model at large N* , JHEP **0007** (2000) 011 [[hep-th/0005147](#)].
- [20] K. N. Anagnostopoulos and J. Nishimura, *New approach to the complex action problem and its application to a nonperturbative study of superstring theory*, Phys. Rev. D **66** (2002) 106008 [[hep-th/0108041](#)].
- [21] J. Nishimura and G. Vernizzi, *Spontaneous breakdown of Lorentz invariance in IIB matrix model*, JHEP **0004** (2000) 015 [[hep-th/0003223](#)].
- [22] J. Nishimura and G. Vernizzi, *Brane world from IIB matrices*, Phys. Rev. Lett. **85** (2000) 4664 [[hep-th/0007022](#)].
- [23] J. Nishimura and F. Sugino, *Dynamical generation of four-dimensional space-time in the IIB matrix model*, JHEP **0205** (2002) 001 [[hep-th/0111102](#)].
- [24] H. Kawai, S. Kawamoto, T. Kuroki, T. Matsuo and S. Shinohara, *Mean field approximation of IIB matrix model and emergence of four-dimensional space-time*, Nucl. Phys. B **647** (2002) 153 [[hep-th/0204240](#)].
- [25] T. Aoyama and H. Kawai, *Higher order terms of improved mean field approximation for IIB matrix model and emergence of four-dimensional space-time*, Prog. Theor. Phys. **116** (2006) 405 [[hep-th/0603146](#)].
- [26] T. Imai, Y. Kitazawa, Y. Takayama and D. Tomino, *Quantum corrections on fuzzy sphere*, Nucl. Phys. B **665** (2003) 520 [[hep-th/0303120](#)].

- [27] T. Imai, Y. Kitazawa, Y. Takayama and D. Tomino, *Effective actions of matrix models on homogeneous spaces*, Nucl. Phys. B **679** (2004) 143 [[hep-th/0307007](#)].
- [28] T. Imai and Y. Takayama, *Stability of fuzzy $S^2 \times S^2$ geometry in IIB matrix model*, Nucl. Phys. B **686** (2004) 248 [[hep-th/0312241](#)].
- [29] K. N. Anagnostopoulos, T. Azuma and J. Nishimura, *Monte Carlo studies of the spontaneous rotational symmetry breaking in dimensionally reduced super Yang-Mills models*, JHEP **1311** (2013) 009 [[arXiv:1306.6135](#) [[hep-th](#)]].
- [30] W. Krauth, H. Nicolai and M. Staudacher, *Monte Carlo approach to M theory*, Phys. Lett. B **431**(1998) 31 [[hep-th/9803117](#)].
- [31] P. Austing and J. F. Wheeler, *Convergent Yang-Mills matrix theories*, JHEP **0104** (2001) 019 [[hep-th/0103159](#)].
- [32] J. Ambjorn, J. Jurkiewicz and R. Loll, *Reconstructing the universe*, Phys. Rev. D **72** (2005) 064014 [[hep-th/0505154](#)].
- [33] H. Kawai and T. Okada, *Asymptotically vanishing cosmological constant in the multi-universe*, Int. J. Mod. Phys. A **26** (2011) 3107 [[arXiv:1104.1764](#) [[hep-th](#)]].
- [34] J. Nishimura, T. Okubo and F. Sugino, *Systematic study of the $SO(10)$ symmetry breaking vacua in the matrix model for type IIB superstrings*, JHEP **1110** (2011) 135 [[arXiv:1108.1293](#) [[hep-th](#)]].
- [35] S. W. Kim, J. Nishimura and A. Tsuchiya, *Expanding $(3+1)$ -dimensional universe from a Lorentzian matrix model for superstring theory in $(9+1)$ -dimensions*, Phys. Rev. Lett. **108** (2012) 011601 [[arXiv:1108.1540](#) [[hep-th](#)]].
- [36] S. W. Kim, J. Nishimura and A. Tsuchiya, *Expanding universe as a classical solution in the Lorentzian matrix model for nonperturbative superstring theory*, Phys. Rev. D **86** (2012) 027901 [[arXiv:1110.4803](#) [[hep-th](#)]].
- [37] S. W. Kim, J. Nishimura and A. Tsuchiya, *Late time behaviors of the expanding universe in the IIB matrix model* JHEP **1210** (2012) 147 [[arXiv:1208.0711](#) [[hep-th](#)]].
- [38] A. Stern, *Matrix model cosmology in two space-time dimensions*, Phys. Rev. D **90** (2014) 12, 124056 [[arXiv:1409.7833](#) [[hep-th](#)]].
- [39] A. Chatzistavrakidis, *Dynamical phase space from a $SO(d, d)$ matrix model*, Phys. Rev. D **90** (2014) 12, 121502 [[arXiv:1407.7054](#) [[hep-th](#)]].

- [40] A. Chaney, Lei Lu, A. Stern, *Lorentzian fuzzy spheres*, arXiv:1506.03505 [hep-th].
- [41] J. Nishimura and A. Tsuchiya, *Local field theory from the expanding universe at late times in the IIB matrix model*, PTEP **2013** (2013) 043B03. [arXiv:1208.4910 [hep-th]].
- [42] A. Chatzistavrakidis, H. Steinacker and G. Zoupanos, *Intersecting branes and a standard model realization in matrix models*, JHEP **1109** (2011) 115 [arXiv:1107.0265 [hep-th]].
- [43] H. Aoki, *Chiral fermions and the standard model from the matrix model compactified on a torus*, Prog. Theor. Phys. **125** (2011) 521 [arXiv:1011.1015 [hep-th]].
- [44] J. Nishimura and A. Tsuchiya, *Realizing chiral fermions in the type IIB matrix model at finite N* , JHEP **1312** (2013) 002 [arXiv:1305.5547 [hep-th]].
- [45] H. C. Steinacker and J. Zahn, *An extended standard model and its Higgs geometry from the matrix model*, PTEP **2014** (2014) 8, 083B03 [arXiv:1401.2020 [hep-th]].
- [46] H. Aoki, J. Nishimura and A. Tsuchiya, *Realizing three generations of the Standard Model fermions in the type IIB matrix model*, JHEP **1405** (2014) 131 [arXiv:1401.7848 [hep-th]].
- [47] H. C. Steinacker, *Spinning squashed extra dimensions and chiral gauge theory from $N=4$ SYM*, Nucl. Phys. B **896** (2015) 212 [arXiv:1411.3139 [hep-th]].
- [48] Y. Ito, S. W. Kim, J. Nishimura and A. Tsuchiya, *Monte Carlo studies on the expanding behavior of the early universe in the Lorentzian type IIB matrix model*, PoS LATTICE **2013** (2014) 341 [arXiv:1311.5579 [hep-lat]].
- [49] Y. Ito, S. W. Kim, Y. Koizuka, J. Nishimura and A. Tsuchiya, *A renormalization group method for studying the early universe in the Lorentzian IIB matrix model*, PTEP **2014** (2014) 8, 083B01 [arXiv:1312.5415 [hep-th]].
- [50] Y. Ito, J. Nishimura and A. Tsuchiya, *Power-law expansion of the Universe from the bosonic Lorentzian type IIB matrix model*, arXiv:1506.04795 [hep-th] (to appear in JHEP).
- [51] G. Parisi, *On Complex Probabilities*, Phys. Lett. B **131** (1983) 393. doi:10.1016/0370-2693(83)90525-7
- [52] P. H. Damgaard and H. Huffel, *Stochastic Quantization*, Phys. Rept. **152** (1987) 227. doi:10.1016/0370-1573(87)90144-X

- [53] G. Aarts, F. A. James, E. Seiler and I. O. Stamatescu, *Complex Langevin: Etiology and Diagnostics of its Main Problem*, Eur. Phys. J. C **71** (2011) 1756 doi:10.1140/epjc/s10052-011-1756-5 [arXiv:1101.3270 [hep-lat]].
- [54] G. Aarts, F. Attanasio, B. Jäger, E. Seiler, D. Sexty and I. O. Stamatescu, *Exploring the phase diagram of QCD with complex Langevin simulations*, PoS LATTICE **2014** (2014) 200 [arXiv:1411.2632 [hep-lat]].
- [55] J. Nishimura and S. Shimasaki, *New Insights into the Problem with a Singular Drift Term in the Complex Langevin Method*, Phys. Rev. D **92** (2015) 1, 011501 doi:10.1103/PhysRevD.92.011501 [arXiv:1504.08359 [hep-lat]].
- [56] K. Nagata, J. Nishimura and S. Shimasaki, “Testing a generalized cooling procedure in the complex Langevin simulation of chiral Random Matrix Theory,” arXiv:1511.08580 [hep-lat].
- [57] K. Nagata, J. Nishimura and S. Shimasaki, *Justification of the complex Langevin method with the gauge cooling procedure*, arXiv:1508.02377 [hep-lat].
- [58] G. Aarts, L. Bongiovanni, E. Seiler and D. Sexty, *Some remarks on Lefschetz thimbles and complex Langevin dynamics*, JHEP **1410** (2014) 159 doi:10.1007/JHEP10(2014)159 [arXiv:1407.2090 [hep-lat]].
- [59] T. Hayata, Y. Hidaka and Y. Tanizaki, *Complex saddle points and the sign problem in complex Langevin simulation*, arXiv:1511.02437 [hep-lat].
- [60] J. Nishimura, T. Okubo and F. Sugino, “Gaussian expansion analysis of a matrix model with the spontaneous breakdown of rotational symmetry,” Prog. Theor. Phys. **114** (2005) 487.
- [61] K. N. Anagnostopoulos, T. Azuma and J. Nishimura, “A General approach to the sign problem: The Factorization method with multiple observables,” Phys. Rev. D **83** (2011) 054504.